A COMPREHENSIVE STUDY OF SOLAR PANELS TILTED UP ON FLAT ROOFS

UNDER WIND ACTION

Hatem Alrawashdeh

A Thesis

in

The Department

of

Building, Civil and Environmental Engineering

Presented in Partial Fulfillment of the Requirements

for the Degree of

Doctor of Philosophy (Building Engineering)

at Concordia University

Montreal, Quebec, Canada

November 2022

CONCORDIA UNIVERSITY

SCHOOL OF GRADUATE STUDIES

This is to certify that the thesis prepared

By: Hatem Alrawashdeh

Entitled: A Comprehensive Study of Solar Panels Tilted Up on Flat Roofs Under Wind Action

and submitted in partial fulfillment of the requirements for the degree of

Doctor of Philosophy (Building Engineering)

compiles with the regulations of the University and meets the accepted standards with respect to originality and quality.

Signed by the final examining committee:

_____	Chair
Dr. Rolf Wuthrich	
_____	External Examiner
Dr. Yukio Tamura	
_____	Examiner
Dr. Lucia Tirca	
_____	Examiner
Dr. Hua Ge	
_____	Examiner
Dr. Lyes Kadem	
_____	Thesis Supervisor
Dr. Theodore Stathopoulos	

Approved by

_____

Dr. Mazdak Nik-Bakht, GPD
Department of Building, Civil and Environmental Engineering

_____

Date   Dr. Mourad Debbabi, Dean
Gina Cody School of Engineering and Computer Science

November 23, 2022

ABSTRACT

A COMPREHENSIVE STUDY OF SOLAR PANELS TILTED UP ON FLAT ROOFS UNDER WIND ACTION

Hatem Alrawashdeh, Ph.D.

Concordia University, 2022

The present thesis provides a wind tunnel study dedicated to comprehensively addressing several vital issues in modeling solar panels in atmospheric boundary layer wind tunnels. Atmospheric boundary-layer-wind-tunnel testing has been recognized as a credible tool for generating wind-induced pressures on structures. The simulation process involves duplicating the characteristics of the approaching atmospheric flow and structure modeling. Nevertheless, this process is not straightforward, and various experimental dilemmas always persist. Testing solar panels in simulated atmospheric boundary flow constitutes a case in point where the size of the prototype of the solar panels remains the most significant constraint to the fulfillment of proper modeling.

Recently, there has been considerable growth in the knowledge of wind effects on rooftop solar panel structures, which stemmed chiefly from experimental modeling in the atmospheric wind tunnels, in response to the demands of solar roofing professionals. A portion of the literature work has contributed to the development of the current design provisions of some wind standards and codes of practice. The current practices for wind tunnel modeling of rooftop solar panels are shown to yield significant discrepancies in the results and arise questions concerning the provisions based on such results. Most previous studies have particularly turned a blind eye toward the geometric test scaling requirement to achieve physically testable models in wind tunnels. Other common practices identified in the previous studies, such as incorrectly handling the air clearance

underneath the solar array and the pressure taps distribution on the solar panel surfaces, have not received adequate attention during the experimental setup.

The present thesis aims to further expand the knowledge in the area of wind loads on rooftop solar panels with a focus on the aerodynamic and design aspects. The objectives of this research are to thoroughly quantify the distortions of the experimental results due to the experimental practices of modeling solar panels tilted on flat roofs in atmospheric wind tunnels, considering that (1) enlarging the geometric scale of the test models; (2) modeling the air clearance between the solar array and the building roof; and (3) arranging the pressure taps coverage on the test models pose modeling challenges shown to be crucial for producing credible wind-induced surface and net pressures on solar panels. The intended objectives of this thesis have been accomplished through a series of wind tunnel experiments carried out in the boundary layer wind tunnel of Concordia University. Three wind tunnel models were designed at geometric scales of 1:200, 1:100, and 1:50 for a prototype of a solar array of eight typical panels mounted on a building with full-scale plane dimensions of 14.0 m and 27.0 m and a height of 7.5 m. The designed models were tested in standard open-country exposure commonly used for codification studies. The solar array of the larger model was placed at three clearance heights above the roof, including gaps of 0, 20 cm, and 40 cm (in full-scale equivalent). Furthermore, six different configurations of pressure-tap coverage were investigated.

The assessment of the results demonstrates that these experimental considerations are critical for modeling rooftop solar panels in the atmospheric wind tunnel. It was found that the surface and net pressures of the solar panels are very dependent on these considerations with high spatial heterogeneity within the array. The thesis has stressed that caution needs to be exercised when testing solar panels in atmospheric wind tunnels and that improper implementation of these

requirements could dramatically risk the credibility of the experimental outcomes and conclusions, notably those treated as design loadings. Finally, a procedure for modeling rooftop solar panels utilizing enlarged models in open-terrain exposure is formulated to assist the generation and codification of design wind pressure coefficients. Furthermore, recommendations are made to remedy the potential distortions owing to the shortfalls in the current design provisions. All proposals are crafted in the interests of practicing wind engineers and architects, code officials, and codification committees.

Keywords

ACKNOWLEDGMENTS

This thesis is not limited to being mere documentation for my work; it goes away beyond that. It is a major milestone in my life after the most rewarding years of work at Concordia University and specifically within the Building Aerodynamics Laboratory, where I have been provided with a rich and stimulating environment that served to build and shape my academic character. In one way or another, this thesis would not have been possible without the support of remarkable individuals whom I wish at the very least to acknowledge.

First and foremost, I would like to express my sincerest respect and gratitude to my supervisor, Prof. Theodore Stathopoulos, for having provided me with useful knowledge, continuous efforts, and guidance. Prof. Stathopoulos has been more than my supervisor; indeed, he was my mentor.

I like to take this opportunity to thank all of you, esteemed friends, colleagues, and lab technicians at Concordia University, especially Murad Aldoum, Jianhan Yu, Anastasia Athanasiou, and Theodore Potsis for their friendship.

I would also like to thank Concordia University and the Natural Sciences and Engineering Research Council of Canada (NSERC) for funding my research.

I am furthermore indebted to my life companion, my wife Esra'a, for her continued and sustainable love, support, and comprehensibility. To my beating heart, my daughters Kenda and Linda, your cheerful characters were the perseverance, discipline, and motivation during the pursuit of my Ph.D. degree. Also, I am grateful to my brothers and sister for their never-ending support and encouragement.

Last but first to my heart, I extend my loftiest expressions of thanks and appreciation to my parents, Mrs. Aida and Mr. Salem Alrawashdeh, who guided me in the right direction, supported my dreams, and encouraged my pursuits.

TABLE OF CONTENTS

LIST OF FIGURES

xiii

LIST OF TABLES

LIST OF SYMBOLS

Symbol	Definition (unit)
A	Effective wind area (m^2)
A_n	Normalized wind area (-)
C_a	Wind factor (-)
C_F	Mean force coefficient (-)
C_P	Mean surface pressure coefficient (-)
E_r	Exposure factor at roof height (-)
G	Clearance height above the roof (m)
GC_F	Peak force coefficient (-)
GC_P	Peak surface pressure coefficient (-)
$(GC_{rn})_{nom}$	Nominal net pressure coefficients (-)
G_f	Gust effect factor (-)
H	Building height (m)
h_{pt}	Parapet height (m)
I_u	Streamwise turbulence intensity (-)
I_v	Lateral turbulence intensity (-)
K_d	Wind directionality factor (-)
K_e	Ground elevation factor (-)
K_h	Exposure factor at roof height (-)
K_t	Topographic factor at roof height (-)
L	Longest side of the roof (m)
L_b	Normalized building length (-)
L_P	Panel chord-length (m)
L_S	Panel span-length (m)
$L_{u,x}$	Streamwise component of the longitudinal integral length scale (m)

n	Cyclic frequency (Hz)
P	Surface wind pressure (Pa)
P_o	Freestream static pressure (Pa)
R_{C_P}	Correlation coefficient of the fluctuating force coefficients (-)
R_e	Reynolds number (-)
Re_r	Flow roughness Reynolds number (-)
R_{C_P}	Correlation coefficient of the fluctuating pressure coefficients (-)
S	Setback distance (m)
S_u	Streamwise power spectral density ($m^2/s^2/Hz$)
u_*	Friction velocity (m/s)
$\overline{U}$	Streamwise mean wind speed (m/s)
$\overline{U}_g$	Streamwise gradient wind speed (m/s)
W	Shortest side of the roof (m)
Z	Height above the ground (m)
Z_g	Gradient height (m)
z_0	Surface Roughness length (m)
α	Power-law exponent constant (-)
γ_C	Panel chord-length factor (-)
γ_E	Array edge factor (-)
γ_P	Parapet factor (-)
θ	Wind direction (°)
v	Kinematic viscosity of the air (m^2/s)
ρ	Density of the air (kg/m^3)
ω	Array tilt angle (°)

CHAPTER 1 INTRODUCTION

Renewable energy projects have become very popular worldwide in recent decades in response to the calls to a sustainable future. Solar technology and energy have significant contributions towards achieving sustainable energy development of safe, clean, and constantly replenished resources. Application of photovoltaic modules to low-rise residential and industrial buildings along with utility-scale solar PV projects are rapidly growing. Efforts to promote such installations encompass the safety and operation of their structures against several environmental impacts, primarily wind-induced pressures.

1.1 Background

The application of PV modules to low-rise buildings increases rapidly. Certainly, this is driven by the advantages of generating energy on-site, for example, decreasing energy dependence for the utility power grid, and addressing climate change, net-zero energy buildings, and sustainable energy development. The applications of solar PV modules according to their mounting system into the buildings are mainly recognized under two broad categories, namely Building Attached Photovoltaics (BAPVs) and Building Integrated Photovoltaics (BIPVs).

In BIPVs systems, PV modules are integrated into the building envelope or components instead of using conventional building materials, primarily in two major placement areas: roofs (e.g., shingles, tiles, and skylights) and façades (e.g., cladding, curtain walls, windows). In addition, PV modules can be integrated into building attachments (e.g., balcony railings and canopies). In BIPV installation, PV modules are considered integral component of the structural envelope system of the building.

In BAPVs installations, PV modules are fixed onto the building walls or roofs at different configurations, namely tilted-up on flat roofs, flushed in parallel to inclined roofs, or mounted on walls. Figure 1.1 illustrates various possible attachments of PV modules into the building. In this kind of installation, PV modules are not considered part of the structural envelope system of the building, but they are deemed to be mountings or attachments to the structural building system.

(a)

(b)
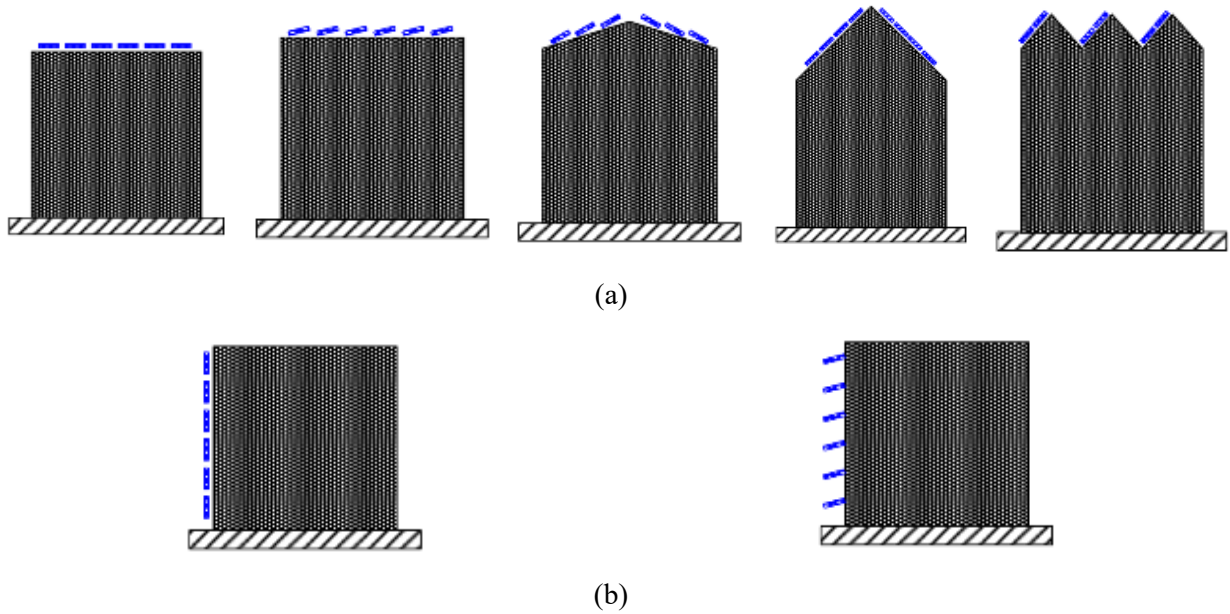
Figure 1.1 Possible installations of solar panels into building's: (a) Roof, and (b) Walls

Rooftop PV solar panels are supported by racking systems that commonly exist in two fundamental forms exemplified by mechanically fastened (penetrating) and ballast restrained systems. In fact, the load-carrying capacity of the roof structural elements has a greater role in selecting the racking system of the solar panels.

The mechanically fastened system can be implemented through posts secured in the roof beams. Roof mechanically fastened solar array weighs on average 0.10 kPa to 0.24 kPa including

the panels and the racking. Although special leak protection is needed at each penetration in the roof façade, the solar array of such a system is more stable in windy regions by very tight junctions of the racking system and the roof. The roof ballasted solar arrays, on the other hand, are the most popular for low-rise commercial and industrial installations (i.e., flat or nearly flat large roofs). This system seems to be preferable mainly by considerations of easy implementation, cost, and most importantly no penetration through the roof façade is needed for construction because the racking system is ballasted using weights or concrete blocks. This system weighs on average 0.17 kPa to 0.34 kPa (Rabinovitch, 2019).

The rooftop PV modules need to satisfy performance and safety criteria and conform to both PV and building design standards, where established. The PV installations shall be designed for fire resistance and potential environmental and hazardous conditions, primarily the weight of snow built-up and wind pressures induced on the surface. Solar panel systems are lightweight structures, and wind pressures on their surfaces unless properly considered may lead to damaging or extremely deforming the array.

Figure 1.2 provides notable examples of cases related to some types of structural failure mechanisms at different levels (i.e., module, panel, or entire array). As shown in Figure 1.2 (a), some modules' cover plate (PV film) was locally damaged either due to local surface wind pressure or wind-prone debris, the PV films of some modules were detached from the supporting frame, and some modules were peeled out off the supporting system but they did not blow away. The failure due to the net wind pressure over the PV module area is clearly illustrated in Figure 1.2 (b), where the clamp has been plucked from its location. Also, the net wind pressure produced over the panel area may damage the entire panel or the array, as shown in Figure 2 (c), where three panels were completely dislocated from the supporting system (rails).

(a)
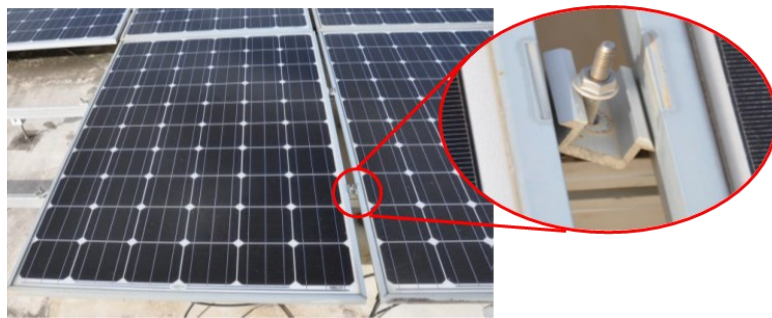
(b)

(c)

Figure 1.2 Examples of real cases for some types of structural failure mechanisms (PV

Magazine, 2018)

According to the solar panels failure mechanisms discussed above, the design requirement for

solar panels on buildings against wind pressures should satisfy the immunity of the PV modules

cover plate from cracking due to surface wind loads, the solar modules from loose or peeling out

from their supports due to the net wind loads received by the area of the module or less, and the array supporting system from damaging or collapsing due to the wind loads received by the panel or array area.

1.2 Thesis Motivation

In structural wind engineering, as it is well-known, the atmospheric boundary layer wind tunnel testing is the most dependable approach for evaluating wind-induced pressure, where such facilities have been extensively utilized for the generation of wind loads on buildings and structures and for the development of the current national wind codes and standards. The simulation process involves duplicating the characteristics of the approaching atmospheric flow and structure modeling. Nevertheless, this process is not straightforward, and various experimental dilemmas always persist. Testing solar panels in simulated atmospheric boundary flow for design- and codification-oriented studies constitutes a case in point where the size of the prototype of the solar panels remains the most significant constraint to the fulfillment of proper modeling. Certainly, this has sparked a renewed interest in examining the scaling techniques in wind tunnels.

Since the turn of the current century, more studies on wind loads on rooftop solar panels have been carried out in response to the demands by solar professionals, including engineers, consultants, and installers, for design guidelines for such installations. Investigation of previous studies on solar panels tilted up on flat roofs, as will be tackled at greater length in the next chapter, shows controversies in the peak force coefficients and also in the impact of the geometric and configuration parameters on the induced wind loads of rooftop solar panels (e.g., building size, array inclination, inter-panel spacing, and array clearance height off the building roof). There is a strong perception that the requirements for modeling solar panels structures in atmospheric wind

tunnels, which have been disregarded in the practice of the experimental work of the literature studies, were the underlying reason for these controversies. The establishment of the perception and the need to illustrate the differences among the previous studies were the main impetus for the initial development of the present thesis, bearing in mind that the extent to which such experimental practices influenced the results has not been quantified in previous studies.

Naturally, the lack of standardization in the testing of rooftop solar panels experimentally in the atmospheric wind tunnels gave an additional impetus for the current thesis. The current study has been undertaken to ascertain the impact of modeling requirements on wind-induced loads on the rooftop solar panels, and ultimately to establish procedural guidelines for testing rooftop solar panel models in the atmospheric boundary layer wind tunnels for design and codification purposes correctly duplicating the natural wind effects.

1.3 Thesis Scope and Objectives

This research aims to effectively further the knowledge in the area of aerodynamic wind loads on rooftop solar panels to strengthen the existing efforts made to achieve the long-term benefits in academia and industry. The present study's threefold focus, namely (1) distortion of the geometric scale between the simulated boundary flow and the test model; (2) modeling the air clearance between the solar array and the building roof; and (3) pressure taps coverage, are modeling challenges that remain in fulfilling the wind tunnel modeling requirements for testing solar panels. The specific objectives pursued in this thesis are to:

I.   Holistically examining and quantifying the impact of the above-mentioned experimental requirements on the wind tunnel results.

II. Understanding and interpreting the differences and controversies that presently exist among the literature studies.

III. Establishing practicable rules of procedure to be used in design- and codification-oriented studies to provide the necessary guidelines for accurately handling the concerned requirements.

Different sets of wind tunnel experiments are devised to achieve the research objectives. The dependence of wind pressures on solar panels on the concerned experimental requirements will be examined in detail from aerodynamic and design perspectives. In this regard, the surface and net mean pressures will be used to frame the flow development around the solar array. Whereas, the surface and net peak pressures will be used to highlight the potential uncertainties in the wind tunnel experimental results that could be deemed as actual design loadings considering several procedures adopted by various wind codes and standards, including North American Wind Codes and Standards (SEAOC, 2017; NBCC, 2020; and ASCE/SEI 7, 2022) and Japanese Standard (JIS C 8955, 2017).

All the experiments have been conducted in the Boundary Layer Wind Tunnel Laboratory of Concordia University.

1.4 Thesis Organization

The thesis is composed of nine chapters, including the current introductory chapter, and is organized as follows:

Chapters 2 and 3 comprehensively address the literature sources on two topics, including available refereed studies on wind effects on solar panels mounted on flat roofs and current wind standards

and codes of practice, respectively.

In Chapter 4, a description of the experimental methodology adopted in this thesis is provided. In addition, it includes a description of Concordia's boundary-layer-wind-tunnel facility, instruments, and equipment.

The subsequent three chapters are devoted to presenting the results and discussing the findings of the issues addressed in the present thesis referred to by the research objectives, separately as follows: Chapter 5 for the influence of the geometric scale of the test model, Chapter 6 for the influence of the air clearance underneath the solar array, and Chapter 7 for the influence of the pressure taps coverage.

Essential guidelines and recommendations are proposed in Chapter 8 to remedy the design provisions of the current wind codes and standards and to establish innovative rules of procedures for proper modeling of solar panels in atmospheric wind tunnels.

Finally, the thesis ends with conclusions and recommendations for future research work.

CHAPTER 2 REVIEW OF THE LITERATURE

The provided review discusses extensively the results of parametric literature studies on wind loads of solar panels tilted up on flat roofs. Also, the ASCE/SEI 49 (2021) requirements are introduced and reviewed along with their implementation in the parametric literature studies.

2.1 Comparison of Previous Studies

Wind effects on solar panels have been studied since the end of the seventies in the last century. In pioneering research (Chevalier and Norton, 1979), variable geometric parameters of ground-mounted solar panels have been investigated experimentally in a wind tunnel of uniform approaching airflow with low turbulence. Full-scale experiments have also been conducted by Chevalier and Norton (1979) on one module of solar panel mounted on a flat roof. A few years later, Radu et al. (1986) and Radu and Axinte (1989) conducted boundary-layer wind tunnel tests to investigate the characteristics of wind loads on solar collectors in clusters mounted on flat roofs of typically five-story building.

Since the start of the twentieth century, more experimental studies have been conducted on rooftop solar panels to assess the wind loads and to understand the geometric influencing parameters. Table 2.1 provides a summary of the geometric parameters of experimental parametric studies on solar panels mounted on flat roofs. Findings from these studies will be compared and discussed from two perspectives; firstly, factual information reported on the impact of the geometric parameters of the solar array and building on wind-induced loads on solar panels (qualitative results), and secondly, data on wind loads on solar panels (quantitative results).

Table 2.1 Wind-tunnel studies on solar panels tilted on flat roofs (Dimensions are in full scale, in meter and degree)

Reference	Building Geometry			Panel (row) Geometry					
	Height (H)	Width (W)	Length (L)	Length (L_C)	Width (L_S)	Tilt (ω)	Underneath Clearance (G)	Number of Rows	Setback (S)
Wood et al. (2001)	12.0	27.0	41.0	2.7	41.0	0	0.60 1.00 1.40	8	0.0
Ginger et al. (2011)	10.0	12.0	12.0	1.7	7.0	15 30	-	1	0.0 6.0
Kopp et al. (2012)	7.3	15.9 23.5 26.9	22.5 25.9	1.0	20.0	2 20	-	12	1.2 2.9
Browne et al. (2013)	10.0	30.0	36.0	1.1	32.4	10	-	16	2.0
Cao et al. (2013)	20.0	10.0 17.5 25.0	25.0	2.0	21.0	15 30 45	-	1 2 5 8	2.5
Kopp (2014)	7.3 14.6 18.3 21.9	15.9 17.4 20.8 23.5 27.1 32.2	22.5	1.0 2.0	20.4	2 5 10 20 30	0.09 0.41 1.02	12	1.2
Stathopoulos et al. (2014)	7.0 16.0	19.6	30.6	5.6	25.8	20 30 40 45	-	1	4.4 10.4
Naeiji et al. (2017)	6.6 10.6	13.7	9.1	2.0	1.0	20 30 40	0.30 0.45	4	0.2
Wang et al. (2018)	20.0	9.1 17.7 26.0	10.3 16.6 18.0 26.0	2.0	21.0	15	-	2 3 4 5 7	1.0 1.8 2.6

The literature studies have been mostly carried out in atmospheric boundary layer wind tunnels, except Naeiji et al. (2017) conducted in the Wall of Wind facility. It was observed that a whole variety of rooftop solar panel installations, including building geometry and solar panel configurations, were considered. Table 2.1 indicates that most of the experiments were performed for solar panels mounted on buildings with plane dimensions greater than 12.0 m and relatively low heights (H < 20 m). These studies have been carried out at different terrain exposures, mostly open-country terrain.

Over the past years, researchers have experimentally demonstrated several geometric parameters affecting wind-induced pressures on rooftop solar panels. Reviewing existing studies points out that findings and observations reported on the impact of some geometric parameters of the building and the configurations of the solar panels are fundamentally in conflict – as summarized in Table 2.2. Accordingly, the influence of building size, roof slope, array inclination, and inter-panels spacing on wind-induced pressures on solar panels is still an open question among the literature studies.

As to the quantitative results, data on wind loads on solar panels mounted on flat roofs are compiled for comparison purposes according to their availability in the current literature. The emphasis is placed on the extreme area-averaged peak force pressure coefficients (i.e., the envelope peak net pressure coefficients versus the effective area of the solar panel). Data and results from seven independent studies concerned with the generating design force coefficients are collected, namely: Browne et al. (2013); Cao et al. (2013); Kopp (2014); Stathopoulos et al. (2014); Naeiji et al. (2017); and Wang et al. (2018). The comparative results are presented in Figure 2.1. It should be noted that the original values of the force coefficients were converted following the same format of ASCE/SEI 7 for pressure coefficients (i.e., 3-sec basic-wind speed). Also, the

Table 2.2 Comparison of observations reported by previous studies on geometric parameters effects

Aspect	Observation and the corresponding study	
	Thesis	Anti-thesis
Building Size	Increased Stathopoulos et al. (2014) Banks (2013) Kopp (2014)	Not Influenced Cao et al. (2013)
Roof Slope	Increased Ginger et al. (2011) Stenabaugh et al. (2010)	Decreased Aly and Bitsuamlak (2014)
Panel Location - Isolated Panel	Not Influenced Stathopoulos et al. (2014) Cao et al. (2013)	None
Panel Location - Multi-panel array	Influenced Cao et al. (2013) Kopp (2014) Aly and Bitsuamlak (2014) Ginger et al. (2011) Stenabaugh et al. (2010)	None
Panel Size	Increased Kopp (2014)	Not Influenced Ginger et al. (2011)
Array Inclination	No clear pattern Kopp (2014) Stathopoulos et al. (2014) Cao et al. (2013) Ginger et al. (2011)	None
Inter-panel spacing	Not Influenced Kopp (2014) Wood et al. (2001)	Increased Cao et al. (2013)

typical configurations of the tested models with their dimensions in full-scale, to which the results are attributed, are shown. It should be mentioned that the GC_F curves are also the envelope from the configurations illustrated in the figure.
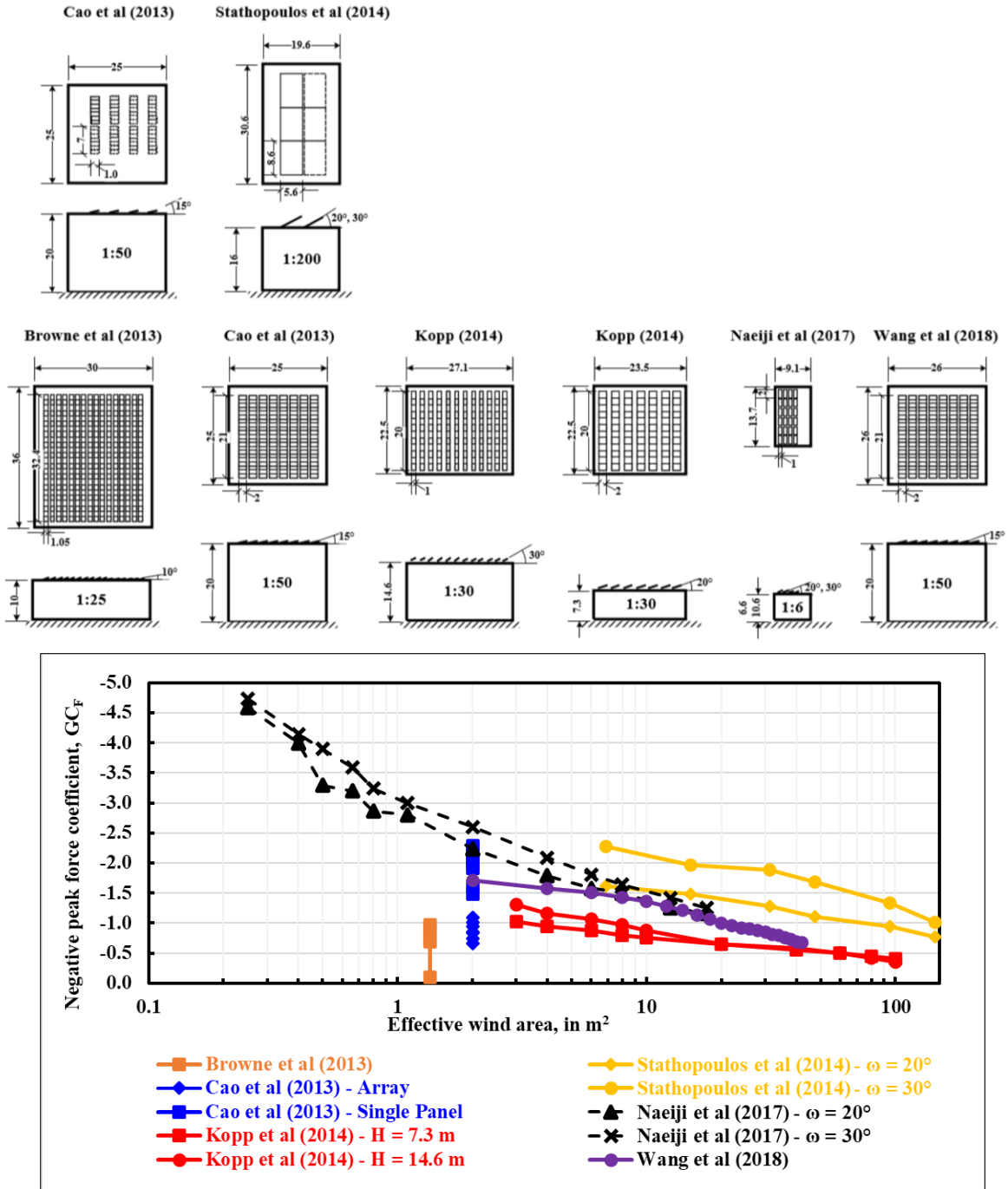
Figure 2.1 Peak net pressure coefficients, GC_F, versus the loading area and the schematic representation for the typical building and solar panels installation with their equivalent full-scale dimensions (in m).

The results of Cao et al. (2013) and Stathopoulos et al. (2014) were obtained from a single solar panel mounted at separate locations, whereas the results of the rest of the studies were obtained from a multi-panel solar array. Clearly, the set of the results presented in Figure 2.1 shows significant differences. These differences, which have a wide range within a factor of up to three, can be attributed to many factors, such as approaching flow characteristics, building and solar panel geometry, and conditions of the experiments, mainly including geometric test scaling and blockage ratio.

The experiments of Naeiji et al. (2017) were carried out in the Wall of Wind facility at geometric test scaling of 1:6 (overall largest scale). However, the largest geometric test scaling of those tested in the atmospheric boundary layer wind tunnel is the one used by Browne et al. (2013), 1:25. This has resulted in a very large blockage ratio of 15%, the largest among the other studies. Despite the technical precautions that have been taken by Browne et al. (2013) to counter the effect of high blockage ratios, such as placing the pitot tube directly above the model at a very high height of 1.525 m, their results are the lowest in comparison with other studies' results although the tested building is the larger in roof size among the other studies.

The higher peak force coefficients are those obtained by Cao et al. (2013) and Stathopoulos et al. (2014). This may reflect the influence of the wind sheltering effects and other local phenomena due to the wind interaction with the panels in multi-panel installation in reducing the net pressure, like those of Browne et al. (2013) and Kopp (2014).

Based on the comparisons made, it is evident that the inconsistencies among the results and findings of the literature studies could potentially be associated with experimental practices adopted in their experimental work, primarily the requirement of the geometric scale of the test model and the approaching flow. Testing models at a scaling ratio of 1:25 to 1:200 were utilized

to obtain larger geometries of solar panels that can be testable in wind tunnels.

In view of this background, the practices of modeling rooftop solar panels adopted by previous studies intended to generate the design pressure coefficients will be introduced and discussed.

2.2 Practices of Modeling Solar Panels in Atmospheric Wind Tunnels

The set of provisions adopted in the latest versions of North American Wind Codes/Standards recommends using the wind tunnel testing procedure for evaluating the wind load coefficients for codification and design purposes for solar array installations that do not fall within their scope of application. In this sense, the requirements of the Wind Tunnel Testing for Buildings and Other Structures (ASCE/SEI 49, 2021) standard will be introduced and reviewed along with their implementation in the parametric literature studies of rooftop solar panels.

In accordance with the criteria and conditions specified by ASCE/SEI 49 (2021), the simulated boundary layer in the wind tunnel for a particular site and wind direction should satisfy the longitudinal mean velocity profile $\left(\overline{U}/\overline{U}_{ref}\right)$, the integral length scale of the longitudinal turbulence $\left(L_{u,x}\right)$, the longitudinal turbulence intensity (I_u), and the power spectral density (S_u). ASCE/SEI 49 (2021) determines the limits for the Reynolds number of the simulated flow $(Re = \overline{U}_H H/\nu)$ or the simulated flow roughness Reynolds number $(Re_r = u_* z_0/\nu)$ to 11000 or 2.5, as a minimum, respectively.

In addition to the above, the geometric scale selected for the building shall result in a wind tunnel test model of a blockage ratio less than 5% and consistent with the simulated boundary layer in different aspects. The model size and the boundary layer size, represented by the roughness length and reference height, are matched. In this regard, the building height normalized with the

roughness length of the field mean velocity profile (H/z_0) should be duplicated in the wind tunnel within a factor of 3 and fully with the reference depth (H/Z_{ref}) for full- and partial-flow simulations, respectively. The integral scale of the simulated longitudinal turbulence must be at least three times as large as the model height in the wind tunnel. Furthermore, the confirmatory of the relative integral scale of the longitudinal turbulence $(L_{u,x}/H)$ of the field can be relaxed to a factor up to 3.0 in the wind tunnel. These conditions are all described in the following equations:

$$\left(\frac{H}{z_0}\right)_{WT} \approx \left(\frac{H}{z_0}\right)_{FS} \qquad 2.1$$

$$\left(\frac{H}{Z_{ref}}\right)_{WT} \approx \left(\frac{H}{Z_{ref}}\right)_{FS} \qquad 2.2$$

$$\left(\frac{L_{u,x}}{H}\right)_{WT} \geq 3.0 \qquad 2.3$$

$$\left(\frac{L_{u,x}}{H}\right)_{WT} \approx \left(\frac{L_{u,x}}{H}\right)_{FS} \qquad 2.4$$

Figure 2.2 presents the simulated atmospheric boundary layer profiles of longitudinal mean wind velocity $(\overline{U})$, normalized by the mean velocity at a height of 10 m $(\overline{U}_{10})$, and the longitudinal turbulence intensity (I_u) versus the normalized height $(Z/10)$ of previous parametric studies. The velocity profile of Exposure C of ASCE/SEI 7 (2022) "Open flat terrain; grass, few isolated obstacles" is regarded as a possible reference for comparison purposes with simulated profiles since this profile is widely adopted in wind-tunnel experiments for the wind loads determination and codification. It should be recalled that all the examined studies have considered open terrain for their experimental work, except Browne et al. (2013) and Naeiji et al. (2017) which were conducted in suburban terrain with respectively roughness length $z_0 = 0.3$ m and $z_0 = 0.2$ m. In

addition, Tables 2.3 and 2.4 summarize the experimental considerations of previous studies on the simulated atmospheric flow and the prototype modeling, respectively.
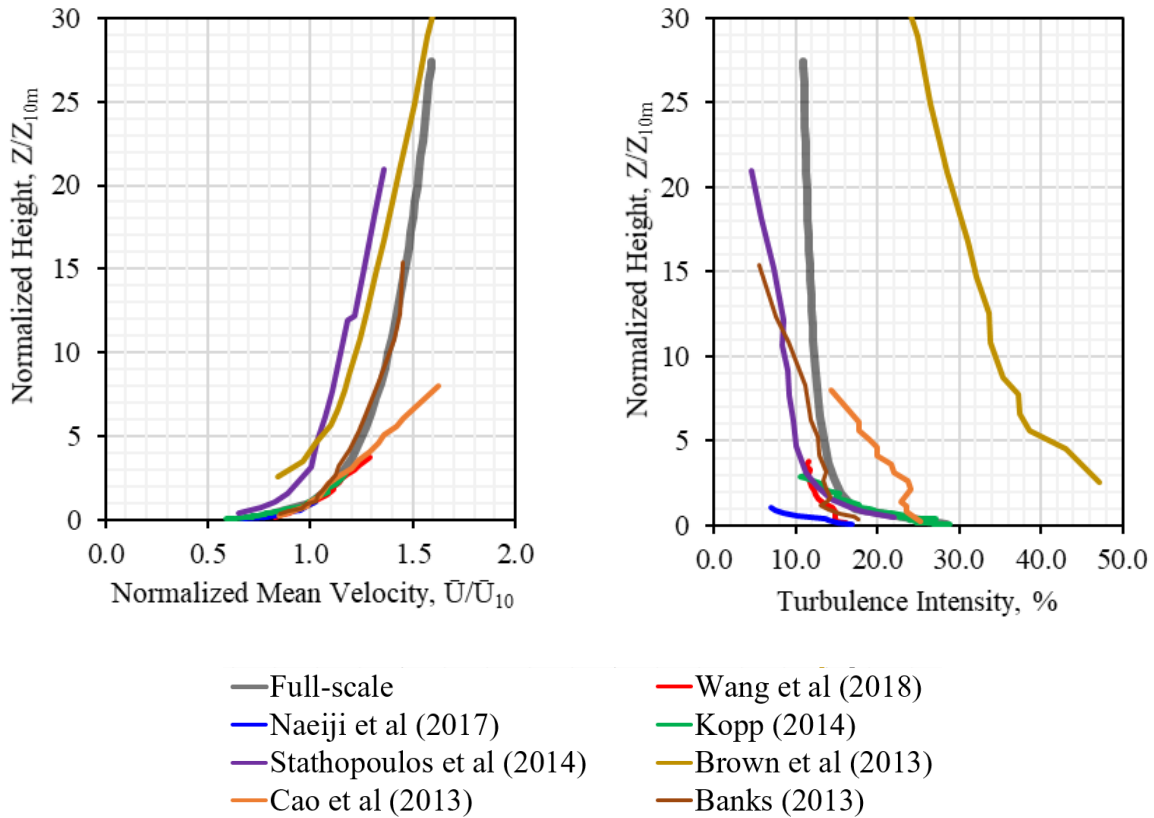
Figure 2.2 Vertical distribution of mean wind speed and longitudinal turbulence intensity of previous studies

Most of the previous studies have resorted to larger geometric scales with partial atmospheric boundary layer simulations (e.g., Cao et al., 2013; Kopp, 2014; Naeiji et al., 2017; Wang et al., 2018), at which the mean wind speed and turbulence intensity extended to the building height or beyond were primarily considered. As shown in Figure 2.2, the mean wind speed profiles of Cao et al. (2013), Kopp (2014), Naeiji et al. (2017), and Wang et al. (2018) show good agreement with

Table 2.3 Considerations on approach flow simulation in previous studies

Study	Type: Full depth (FD) Partial depth (PD)	Exposure z_0 in full-scale (m)	Re_r	$Re \times 10^5$ (Based on H)	I_u (Based on H, %)
Wang et al. (2018)	PD 2 times the building height 1:50	Open Terrain $z_0 = 0.01$ m	14.8	2.6	12.5
Naeiji et al. (2017)	PD Little height above the roof height 1:6	Suburban terrain $z_0 = 0.2$ m	-	16.0 ($H = 6.6$ m)	10.8 ($H = 6.6$ m) 8.0 ($H = 10.6$ m)
Kopp (2014)	PD Reasonable height above the roof height 1:30	Open Terrain $z_0 = 0.03$ m	-	1.9 ($H = 7.3$ m)	21.9 ($H = 7.3$ m) 14.6 ($H = 14.6$ m) 13.3 ($H = 21.9$ m)
Stathopoulos et al. (2014)	FD 1:400	Open Terrain $z_0 = 0.10$	11	-	17.7 ($H = 7.0$ m) 13.9 (H = 16 m)
Banks (2013)	FD 1:100	Open Terrain $z_0 = 0.03$	-	-	9.3 ($H = 15$ m) 10.3 ($H = 30$ m)
Browne et al. (2013)	FD 1:400	Suburban Exposure B $z_0 = 0.3$	-	-	31.1
Cao et al. (2013)	PD 2 times the building height 1:50	Open Terrain $z_0 = 0.01$	14.8	2.6	20.0

Table 2.4 Considerations on prototype modeling in previous studies

Study	Geometric Scale	$\left(\frac{H}{z_0}\right)_{WT}:\left(\frac{H}{z_0}\right)_{FS}$	$\left(\frac{H}{z_{ref}}\right)_{WT}:\left(\frac{H}{z_{ref}}\right)_{FS}$	$\left(\frac{L_{u,x}}{H}\right)_{WT}:\left(\frac{L_{u,x}}{H}\right)_{FS}$	$\left(\frac{L_{u,x}}{H}\right)_{WT}$	Blockage ratio (%)
Wang et al. (2018)	1:50	NA	1:0.14	1:4.4	1.0	4.9
Naeiji et al. (2017)	1:6	NA	1:1	1:18 (H = 6.6 m) 1:32 (H = 10.6 m)	0.4 (H = 6.6 m) 0.3 (H = 10.6 m)	16.0
Kopp (2014)	1:30	NA	1:0.10	-	-	8.0
Stathopoulos et al. (2014)	1:200	1:0.5	1:0.5	1:2.0	4 (H = 7.0 m) 2.4 (H = 16 m	0.5
Banks (2013)	1:50	1:0.5	1:0.5	-	-	< 7.0
Browne et al. (2013)	1:25	1:0.06	1:0.06	-	-	15.0
Cao et al. (2013)	1:50	NA	1:0.14	1:4.4	-	7.1

Z_{ref} in the wind tunnel corresponds to the depth of the simulated flow and in full-scale to the depth of ABL (Z_g = 273 m for open terrain).

the Exposure C of ASCE/SEI 7 (2022) for only a few dozen meters (10%-15% of the full boundary layer depth with $Z_g = 274$ m). Except for Banks (2013), Kopp (2014), and Stathopoulos et al. (2014) for a relative height up to Z/10 = 3, the turbulence intensity profile of ASCE/SEI 7 (2022) has been mostly underestimated among the profiles of the previous studies.

In addition to disregarding the entire mean wind speed profile similarity and the similarity of Jensen number $(J_e = H/z_0)$ in the wind tunnel and in the field, the uncertainty in such simulations lies in the estimation of the turbulence scale and the distortion of several parameters at once. For instance, using the partial flow models (i.e., partial atmospheric boundary layer simulations) in the experimental work had the effect of disregarding the power spectral density over the entire frequency range. It was found that the reduced power spectra of the partial flow model used in the study of Kopp (2014) were overestimated within the dissipation range (i.e., at long wavelength) of the full-scale reduced power spectra. Also, the partial flow model adopted in the study of Naeiji et al. (2017) has largely underestimated the full-scale reduced power spectra within the production and inertial ranges. Thus, in the case of Naeiji et al. (2017), the full-scale reduced power spectrum has been achieved within the dissipation range.

The distortion of the power spectra has been primarily prompted by disregarding the integral length scale of the turbulence and flow roughness aspects. The ratio of the integral turbulence scale to the building height $(L_{u,x}/H)$ has been widely underestimated in the wind tunnels used partial flow models with a factor up to 32 at the larger geometric scale of 1:6 – See Table 2.4. Also, the relative integral turbulence scale, $L_{u,x}/H$ simulated in the wind tunnel, has been found less than one, which is much lower than the limit specified by ASCE/SEI 49 (2021). Although it is correct that the similarity of the field and wind tunnel integral turbulence scale $(L_{u,x})$ is not of crucial importance for the application of evaluating wind loads on low-rise buildings, the similarity of the

relative integral turbulence scale $(L_{u,x}/H)$ is important. This is indeed a point worth considering, and from this point of view, the wind-tunnel and full-scale comparative study by Tieleman et al. (1997) will be re-visited.

Tieleman et al. (1997) have made a comparison between a full- and model-scale surface pressure. The field measurements were obtained from the Wind Engineering Research Laboratory (WERFL) at Texas Tech University. For the approach flow simulation, consideration has been given only to the streamwise and lateral turbulence intensities (I_u and I_v, respectively). On this basis, two simulations have been modeled, one with I_u $(H) = 20.6\%$ and $I_v(H) = 15.9\%$ and the other with I_u $(H) = 20.5\%$ and I_v $(H) = 13.1\%$. Two sets of experimental results have been obtained on a model scaled down at a ratio of 1:50 – details of the building prototype are shown in Figure 2.3. The turbulence integral scale has not received attention and was found to be 3.2 and 7.0 times greater than the simulated wind tunnel flows.

As shown in Figures 2.3 and 2.4, two sets of roof peak pressure coefficients were quoted from Tieleman et al. (1997) for further discussion, respectively: along the roof for 0° and 180° wind directions and close to the corner versus the wind direction. As indicated by Tieleman et al. (1997), maintaining the field integral turbulence scale in the wind tunnel flow is not deemed necessary for the evaluation of wind loads on low-rise buildings. That indeed sounds about right, as the wind tunnel results of Simulation 2 of the smaller integral length scale compared with the field flow integral scale (simulation 2 with $(L_{u,x})_{FS}/(L_{u,x})_{WT} = 7.0$) show better occasional similarity with the field results, particularly the peaks average and the upper-ceiling limit of the peak values – see Figures 2.3 and 2.4.

On the other hand, it is possible to interpret the results in terms of the similarity of the integral length scale with the prototype height referred to by Equation 2.4. The ratio of the integral scale

Dimensions in full-scale
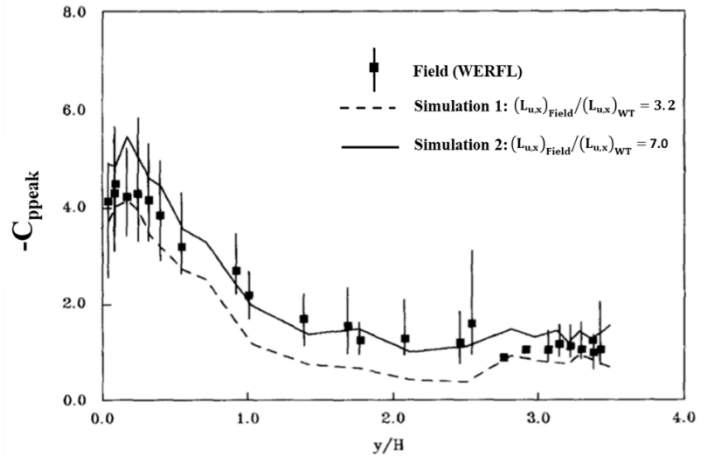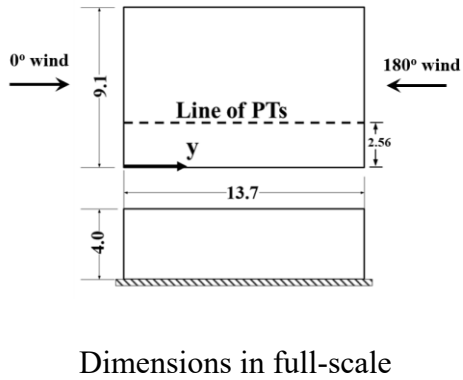
Figure 2.3 Roof peak pressure coefficients of wind tunnel results and full-scale along the

building edge (after Tieleman et al., 1997)
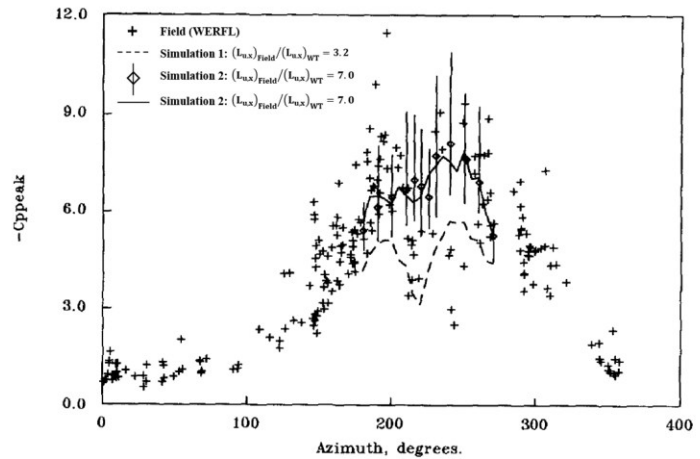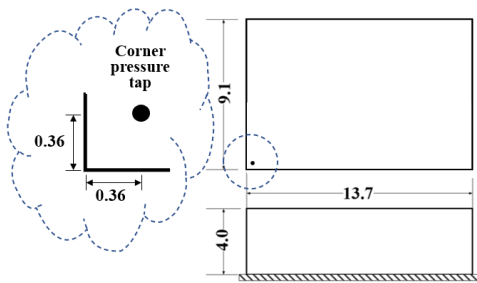
Figure 2.4 Peak pressure coefficients of wind tunnel results and full-scale for a corner pressure

tap (after Tieleman et al., 1997)

of the field turbulence to the building height and the integral scale of the simulated turbulence to

the wind tunnel model height is found to be 1:15.6 and 1:7.1 for simulations 1 and 2, respectively. This implies that the results obtained at wind tunnel modeling conformed to the closest level of matching between the integral length scale and the building height (simulation 2 with $\left(L_{u,x}/H\right)_{FS}\big/\left(L_{u,x}/H\right)_{WT} = 7.0$) tend more to better duplicate the field data.

Furthermore, the study by Hunt (1982) has experimentally addressed the issue of the wind tunnel geometric test scale on the surface mean and fluctuating pressures of a cube prototype of a height of 36.0 m. Two boundary flows have been simulated with a scale of 1:360 (full depth) and 1:180 (partial model). Three models of different scales have been independently tested in each flow for the wind direction perpendicular to the roof edge.

The results obtained by partially developed approaching flow had shown that doubling the correct model size leads to underestimating the mean pressure coefficients of the windward wall (5%), the leading edge of the roof (30%), and the leeward wall (40%). While, reducing the correct model size to half had resulted in overestimating the mean pressure coefficients of the windward wall (5%), the leading edge of the roof (25%), and the leeward wall (60%). Also, it was found that the root-mean-square values of the windward wall and roof's leading edge of models of double and half of the correct size were underestimated and overestimated by 30%, respectively. The results obtained by the more fully developed boundary flow demonstrated the same trend, but the results were less discrepant with violating the geometric test scaling.

The use of the Partial Turbulence Simulations for testing rooftop solar panels is permitted for the first time by the current edition of ASCE/SEI 49 (ASCE/SEI 49, 2021). It is specified that at using models at large scales (i.e., 1:50 or larger), the similarity of the power spectrum of the longitudinal turbulence at only high frequencies is to be considered in the simulated flow regardless of other similarity conditions and criteria discussed above.

The first systematic study of the partial turbulence simulation method was carried out by Mooneghi et al. (2016) in the Wall of Wind facility at Florida International University (FIU). In this study, two independent methods were considered regarding the simulated flow, the PTS and the 3DPTS methods. The simulation established among the PTS method focused on the similarity of reduced power spectrum within the dissipation range only (at high frequencies) in the streamwise direction only, while the 3DPTS method accounts additionally the effects of the lateral and vertical fluctuations at only high frequencies. The study has concluded upon comparing the experimental peak pressure coefficients with the full-scale results for the Silsoe cube and the TTU buildings that the PTS can lead to discrepancies depending on the wind direction, namely overvaluing the negative peak pressure coefficients at the critical wind direction and undervaluing tendencies at other wind directions. The 3DPTS method, despite being more costly and complex in modeling, has led to conservative results.

As indicated in Tables 2.3 and 2.4, the adoption of models at larger sizes in the simulations of the previous studies had further increased the Reynolds number, but it gave rise to problems associated with the blockage ratio. The blockage ratio of the above-mentioned wind loading studies on rooftop solar arrays was mostly found higher than the 5.0% limit on the wind-tunnel test section blockage specified by ASCE/SEI 49 (2021).

Air gap between the solar array and the roof, also referred to as array clearance off the roof, is also one of the challenges that remain in fulfilling the wind tunnel modeling requirements for testing solar panels. In line with earlier practices for modeling solar panels in atmospheric wind tunnels and the fact that ASCE/SEI 49 (2021) does not require modeling this layout feature, some studies of wind loading on solar panels in the literature tended to disregard the array clearance in their wind tunnel modeling due to the limitations on the wind-tunnel model size, either by setting

the solar array directly on the roof (e.g., Cao et al., 2013; and Wang et al., 2018) or, indiscriminately, at a certain possible clearance above the roof just to consider the airflow between the solar array and the roof (e.g., Stathopoulos et al., 2014).

In comparison, limited studies have touched upon the influence of the array clearance on wind loading of tilted solar panels on flat roofs – see Table 2.1. Wood et al. (2001) examined the effect of the air clearance of solar panels flushed on a flat roof for three heights of 0.60, 1.00, and 1.40 m (in full-scale). It is found that increasing the height of the solar panels above the roof has increased the magnitude of the negative pressure coefficients of the upper surface and the net pressure of solar modules located close to the leading edge of the building.

Kopp (2014) has examined experimentally the effect of the clearance on the extreme area-averaged force coefficients, i.e., the most critical peak net pressure coefficient values enveloped from all wind directions. In this investigation, the solar array has been placed at three heights above the roof (9, 41, and 102 cm, in full-scale) at two tilt angles 5° and 20°. It was found that the array clearance has a minimum impact on the pressure envelope curves for the configurations considered, except for the largest clearance (102 cm) and the lowest tilt (5°), at which a considerable increase in the envelope curves of the negative area-averaged force coefficients was observed in the range of 1.3 to 1.6. Naeiji et al. (2017) studied the extreme module force coefficients over the array at two heights above the roof, namely 30 cm and 45 cm, by using large-scale models (1:6) and found that the extreme net pressure coefficients averaged over the module area show minor differences with the array air clearance.

A recent computational study using Large Eddy Simulation (LES) by Wang et al. (2020b) has also dealt with the array clearance effect. The study has focused on the variation of the surface pressure coefficients at oblique wind directions, including 45° and 135°, at three different

clearances above the roof (0, 30, and 60 cm, in full-scale). It has been found that the clearance size has a slight impact on the mean pressure coefficients on the upper surface of the solar panels but a significant impact on the respective values induced on the lower surface. In particular, the local suction on the lower surface of the windward corner modules increases by a factor up to 2.0 in the presence of clearance.

As a geometric parameter in the set of the design variables, the current wind codes and standards do not address the impact of array clearance on wind loading, as will be discussed in the next chapter.

Another requirement of modeling solar panels in the wind tunnel is the spatial resolution for the pressure taps coverage on the solar panel surfaces. The pressure taps are practically wired discrete holes made on the structure surface to capture the wind-induced pressure. These taps are connected into specific tubes to transmit the recorded pressure signals at the surface to the measurement system. Obviously, high-density taps are recommended for regions of the building cladding that expose high surface pressure degradation, i.e., roof corners, edges, and ridges.

The ASCE/SEI 49 (2021) requires that pressure shall be measured at an adequate number of locations so that all significant aerodynamic events are captured. In the case of the models of solar panels, the flexibility of space is limited, since both surfaces of the solar panel are required to be equipped with pressure taps for the evaluation of the surface and net pressure across the panel. Besides the considerations on the location and density of pressure taps, the special alignment of the pressure taps on upper and lower surfaces of the panel is also a concern that remained for further examination.

By the lack of a procedural regularity framework, many experimental practices on the pressure taps coverage in the design of models of the literature studies have been noticed. This is

also partly because the degradation characteristics of the wind-induced surface and net pressures have not been sufficiently addressed in previous studies; and hence, there are no standardized arrangements and density for the pressure taps. In the studies of Banks (2013), Browne et al. (2013), and Kopp (2014), different numbers of pressure taps on each surface have been considered. The solar panel model test of Kopp (2014) has been equipped with 3 lines of pressure taps on the upper surface corresponding to only one line of pressure taps on the lower surface along the center of the panel, in a total of 12 and 4 pressure taps on the upper and lower surface, respectively. Banks (2013) considers 5 pressure taps on the upper surface and 2 pressure taps on the lower surface. Browne et al. (2013) have adopted opposite distribution for the pressure taps, where higher pressure taps coverage was on the lower surface. Although two lines of pressure taps close to the panel edges were considered on each surface, the pressure taps on each surface lack spatial alignment across the panel.

Other studies, for example, Cao et al. (2013), Stathopoulos et al. (2014), Naeiji et al. (2017), and Wang et al. (2018), have considered pressure taps identical in their distribution on the solar panel surfaces. In the studies of Cao et al. (2013) and Wang et al. (2018), pressure taps at very high-density are considered on both surfaces, which on the other hand made disregarding the air clearance between the solar array and the roof and placing the solar array directly on the roof was the only option to carry out the experimental setup. Naturally, models equipped with ill-suited pressure taps coverage led to mis-capturing and misrepresenting the actual degradation of the surface and net pressures of rooftop solar panels.

CHAPTER 3 CURRENT WIND CODES AND STANDARDS

This chapter examines the provisions of the current wind codes and standards for solar arrays tilted on flat roofs from various aspects, including their formulation, technical procedures, and approaches. Furthermore, comparisons with results from previous studies are included.

3.1 Procedures of Assessing Wind Loads on Solar Arrays Tilted on Flat Roof

Wind load provisions of different wind codes and standards, namely North American Wind Codes/Standards (SEAOC, 2017; NBCC, 2020; and ASCE/SEI 7, 2022) and Japanese Industrial Standard (JIS C 8955, 2017), will be discussed. The procedures used by these wind codes/standards to calculate the design wind loading for solar panels tilted on flat roofs are summarized in Table 3.1.

As illustrated, the existing wind load provisions are confined to the design net pressure coefficients. Such criteria are needed to prescribe wind loads on individual PV modules, panels, array, and their connections and supporting systems. Nevertheless, the existing provisions still do not provide design coefficients for the PV modules cover plate (e.g., PV film). However, such elements form the surface area and are directly exposed to the wind pressures.

The current set of wind load provisions of Canada and the USA, first adopted in the 2015 edition of NBCC and the 2016 edition of ASCE/SEI 7, are used to design rooftop solar panels at two installations (inclined on flat roofs or parallel to sloped roofs). These provisions, as well as of SEAOC (2017), were drawn from the older version of the Structural Engineers Association of California (SEAOC, 2012) with some adjustments applied based on the wind tunnel study of Kopp

(2014).

Table 3.1 Design wind pressure coefficients procedure for solar arrays mounted inclined on a

flat or nearly flat roof

	SEAOC (2017) ASCE/SEI 7 (2022)	NBCC (2020)	JIS C 8955 (2017)
Design Net Pressure Coefficients: GC_F	$K_h K_{ht} K_d K_e \gamma_P \gamma_C \gamma_E (GC_{rn})_{nom}$	$C_e C_t \gamma_P \gamma_C \gamma_E (GC_{rn})_{nom}$	$E_r^2 G_f C_a$
Exposure factor at roof height	K_h	C_e	E_r
Topographic factor at roof height	K_{ht}	C_t	-
Wind directionality factor	K_d	-	-
Ground elevation factor	K_e	-	-
Parapet factor	γ_P	γ_P	-
Panel chord-length factor	γ_C	γ_C	-
Array edge factor	γ_E	γ_E	-
Nominal net pressure coefficients	$(GC_{rn})_{nom}$	$(GC_{rn})_{nom}$	-
Gust effect factor	-	-	G_f
Wind factor	-	-	C_a

The design wind pressures of SEAOC (2017), NBCC (2020), and ASCE/SEI 7 (2022) are applicable to rooftop solar panels installed on enclosed or partially enclosed buildings of all heights and roof with a slope of $\theta \leq 7°$ - see Appendix A-1. The solar array geometry and configuration shall be confirmed to the following configurations: chord-length (L_P) < 2.04 m, tilt angle (ω) ≤ 35°, the height of the panels' lower edge off the roof (G) ≤ 0.61 m, the height of the panels' higher edge off the roof ≤ 1.22 m, and a minimum gap provided between the panels of the row of 0.0064 m but not larger than 2.04 m. Furthermore, the solar array shall be installed at a minimum setback

distance from the roof edges of max $\left[2\left(h_2 - h_{pt}\right), 1.2\ m\right]$, in which h_2 is the height of the higher

panel's edge above the roof and h_{pt} is the mean parapet height.

The considered North American wind codes and standards adopt different formulations for the determination of the Design Net Pressure Coefficients of the solar panels from those assigned traditionally by ASCE/SEI 7 and NBCC for components and cladding (C&C) external pressure coefficient. Besides the new factors associated with the array configuration (i.e., solar panel chord-length, array edge condition, or parapet existence), a new definition for the effective wind area of the design pressure has been incorporated, the so-called "normalized wind area (A_n)". However, nominal net pressure coefficients $((GC_{rn})_{nom})$ curves were established based on a methodology like that used for the ASCE 7 or NBCC components and cladding external pressure coefficient (i.e., enveloped of wind tunnel data from all wind directions), these curves are provided versus the normalized wind area of the solar panel.

Furthermore, the design nominal net pressure coefficients $((GC_{rn})_{nom})$ are provided for three loading zones depending on the solar module or panel location on the roof. These loading zones for PV modules are similar in layout to components and cladding roof external pressure coefficient loading zones (i.e., consist of a square corner, edge, and interior zones), but they differ in size. The corner and edge loading zones for PV modules are of the same size, which equals twice the building height. These definitions were introduced to reflect as much as possible the actual nature of the wind interaction with inclined rooftop solar panels on flat or nearly flat roofs; nevertheless, their application in practice may pose interpretation difficulties and problems.

The normalized wind area (A_n) is a new non-dimensional formulation for the effective wind area (A) of the panel in terms of the normalized building length (L_b), calculated as follows:

$$A_n = \frac{1000}{[max(5, L_b)]^2} \times A, \quad L_b = min[0.4(hL)^{0.5}, \ h, \ W] \qquad\qquad 3.1$$

in which h, L, and W are the building mean height, longest side of the roof, and shortest side of the roof, respectively.

The parapet factor (γ_P) and the panel chord-length factor (γ_C) accommodate the potential increase in wind loads at oblique wind directions due to the existence of the parapets and due to the increase in the chord length of the panel, respectively. γ_P and γ_C are given as follows:

$$\gamma_P = min\big(1.2, 0.9 + h_{pt}/h\big) \qquad\qquad 3.2$$

$$\gamma_C = max(0.6 + 0.2L_P, 0.8) \qquad\qquad 3.3$$

in which L_P is the panel chord-length and h_{pt} is the parapet height in meters.

The array edge factor $(\gamma_E = 1.5)$ is applied to solar panels or solar modules that are exposed to higher upward wind loads; otherwise, for non-exposed (shielded) solar panels or solar modules, it is not necessary to apply the edge factor (i.e., $\gamma_E = 1.0$). A panel can be regarded as exposed where it is installed at a distance greater than 0.5h from the roof edge and installed at distance greater than the $max(4h_2, 1.2 \ m)$ to the next panel. Solar modules located at the end of the panels over a length of $1.5L_P$ in the spanwise direction may be considered exposed if the panel ends maintained a distance greater than 0.5h from the roof edges.

The guidelines of JIS C 8955 (2017) for solar arrays mounted on flat roofs are limited to solar panels with a higher edge height that does not exceed 9.0 m above the roof and tilted at an angle less than 60°. The gust effect factor (G_f) of JIS C 8955 (2017) is evaluated as a function of the terrain category and array mean height above the ground. The wind factor of the array plane (C_a), which is comparable to the mean net pressure coefficients of ASCE/SEI 7 (2022), depends on the

solar panel installation (on flat roofs or gable roofs), the wind direction (either 0° or 180°), array inclination, and whether the module is considered end (exposed) or interior (shielded). Accordingly, a solar module is considered exposed, if it is located on the upstream solar panel or on the side edges of each panel within the array, as illustrated in Appendix A-2.

The design procedure of various wind codes and standards of practice is recognized. However, it is demonstrated that the design provisions of rooftop solar panels of JIS C 8955 (2017) have a wider scope of application than their counterparts in other wind codes and standards, and perhaps more practical and flexible because it includes a more designer-friendly procedure. The conceptual differences between the North America Wind Code/Standard and the Japanese Standard lie in wind direction for the design net pressure coefficient. As mentioned, the North American Wind Codes/Standards adopt the envelope from all wind directions on the building, while the JIS C 8955 (2017) considers only two wind directions for the design, either 0° or 180°. However, previous studies on rooftop solar panels have established that oblique wind directions are unfavorable wind conditions for extreme peak net pressure coefficients (Banks, 2013; Naeiji et al., 2017; Alrawashdeh and Stathopoulos, 2020; and Wang et al., 2020).

3.2 Comparison with JIS C 8955 (2017) and ASCE/SEI (2022)

The set of results from literature studies, presented formerly in Figure 2.1, are compared against the corresponding design force coefficients prescribed by JIS C 8955 (2017) and ASCE/SEI (2022). Figures 3.1 and 3.2 show the results of a single solar panel mounted at separate locations and the results of a multi-panel solar array, respectively. It should be mentioned that the purpose of these comparisons is not to evaluate the performance between wind codes and standards, but to address the conflicts and improve the procedures for the evaluation of the wind loads of solar

panels mounted on flat roofs.
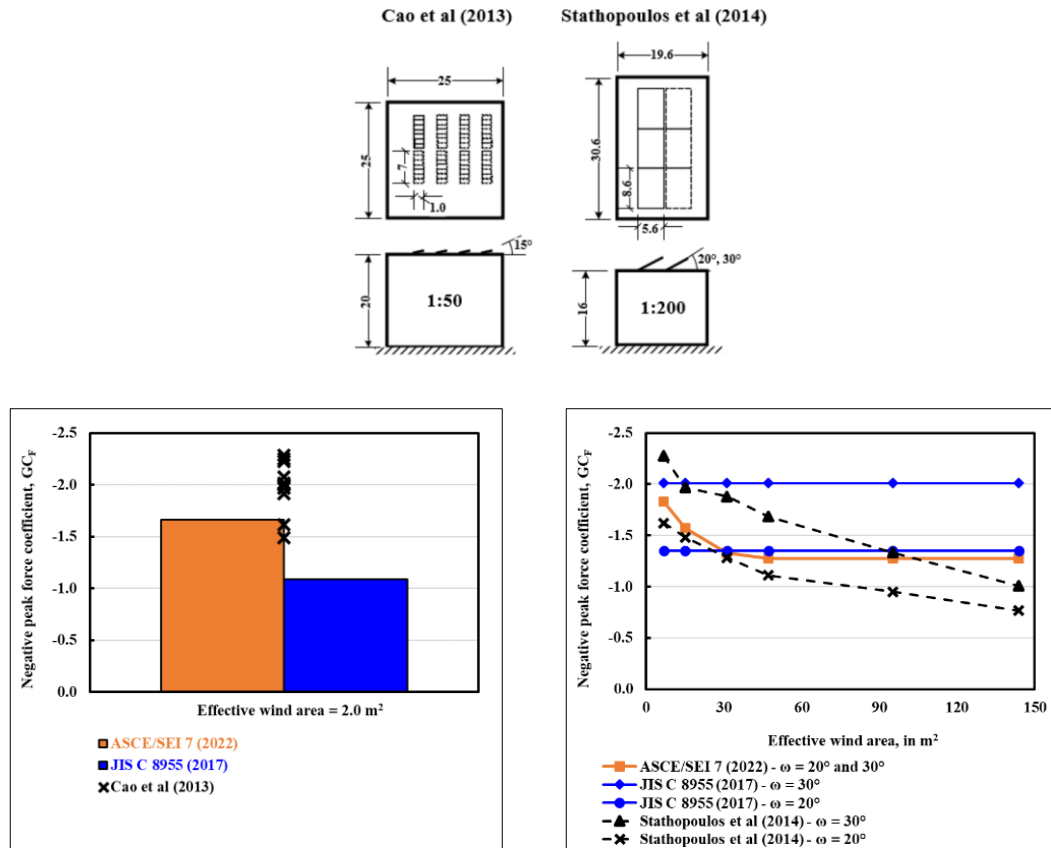
Figure 3.1 Extreme negative area-averaged peak force coefficients, envelope GC_F for single solar array: Comparison with JIS C 8955 (2017) and ASCE/SEI (2022)

It is obvious from Figures 3.1 and 3.2 that the outcomes of the considered wind standards are inconsistent, particularly with increasing the effective wind area of the panel. In the case of a single solar array presented in Figure 3.1, the solar panel is considered exposed by both wind standards. On the other hand, for the multi-panel solar array presented in Figure 3.2, the solar panels are only considered exposed according to JIS C 8955 (2017). In such installations, the solar panels within the array at their configurations are found shielded by ASCE/SEI 7 (2022). In addition, the effect of the area-average concept is clearly demonstrated. Thus, the design force coefficients of
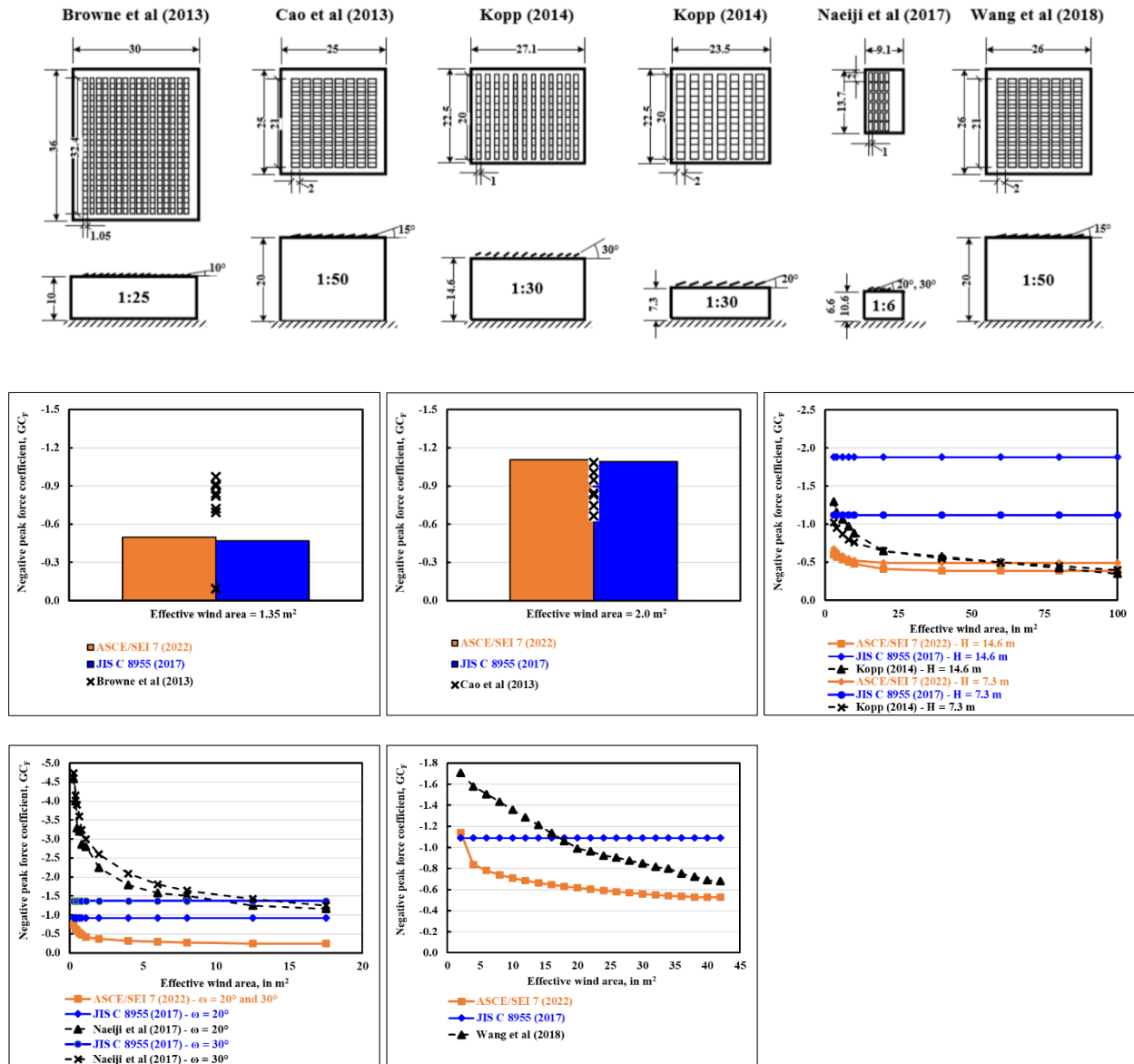
Figure 3.2 Extreme negative area-averaged peak force coefficients, envelope GC_F for multi-panel solar array: Comparison with JIS C 8955 (2017) and ASCE/SEI (2022)

ASCE/SEI 7 (2022) have collapsed with the effective wind area of the panel, but that is not the case with JIS C 8955 (2017). However, it is noticed that the application of the normalized wind area, defined by Equation 3.1, for the considered buildings with $0.4\sqrt{hL} < h$ and W has resulted in a high conversion factor between the effective wind area of the solar panel and the normalized

wind area (A_n). For instance, the conversion factor for the buildings of Kopp (2014) and Naeiji et al (2017) is found to be 36 and 40, respectively. This leads to adopting very low values of Nominal Net Pressure Coefficients, i.e., values on the right tail of $(GC_{rn})_{nom}$ curves – Appendix A-1.

Despite the amount of research carried out in attempting to create code/standard provisions suitable for the design of solar panels on building roofs, the design information for these structures is still in the process of genesis. Along with the notes made on the technical procedures, particularly on the panel condition of being exposed/shielded and the normalized wind area of the panels, a marked observation emerging from the data comparisons with the wind codes and standards values is that the design force coefficients of North American Wind Codes/Standards, represented by GC_F of ASCE/SEI 7 (2022), are significantly lower than the experimental results.

3.3 Thesis Justification

The examination of the previous studies on wind loads on solar panels mounted on flat roofs demonstrated inconsistencies and contradictions in their results and findings. These controversies are perceptibly attributed to the methodological exercises and criteria adopted in their experimental work, which have not been substantiated adequately yet. Certainly, this issue would have a direct bearing upon the credibility and reliability of the developed wind provisions of the current codes and standards of practice for rooftop solar panels.

Research on considerations for testing rooftop solar panels in atmospheric boundary layer wind tunnels is fully justified. By the lack of systematic studies or standardized regulations in this respect, the question of the implications of (1) enlarging the geometric scale of the test models, (2) modeling the air clearance between the solar array and the building roof, and (3) selecting pressure

taps coverage on wind loading of tilted solar panels on flat roofs became the incentive for conducting the present experimental research with the objective to thoroughly quantify the dependence of wind-induced pressure on these requirements from aerodynamic and design perspectives.

(1) Geometric scale for models of solar panels: Carrying out experiments at the correct scale in standard open-country exposure, commonly used for codification-oriented studies, is an end that could not be satisfied in the wind tunnel. Disturbing the characteristics of the atmospheric boundary layer flow in parallel with the model size to adopt larger models would be experimentally a suboptimal choice in the process of modeling prototypes of small sizes (i.e., rooftop solar panels) in conventional atmospheric wind tunnels. Certainly, a more convenient modeling technique and a procedure are still needed to solve this experimental dilemma, especially when it comes to generating the design pressure coefficients and codification-oriented studies.

(2) Air clearance between the solar array and the building roof: The impact of the clearance on the wind loads on solar panels mounted tilted on flat roofs has not yet been comprehensively studied and the aerodynamic potential consequences of the array clearance have not been well understood. Furthermore, the current national wind codes and standards commonly used in professional practice do not address the impact of array clearance on wind loading.

(3) Pressure taps coverage: Recognizing the perception that the net pressure of the solar panels is subjected to high degradation, the proper implementation of the pressure taps is also a concern that remained for further examination, i.e., considerations on their location, density, and their spatial alignment on the upper and lower surfaces of the panel.

In response to the research questions and for the absolute need of establishing practicable

rules of procedure for modeling solar panels in atmospheric boundary layer wind tunnels accurately duplicating the wind effects to be used in wind-tunnel studies oriented for design and codification, a series of experiments have been conducted in the Atmospheric Wind Tunnel of Concordia University.

CHAPTER 4 METHODOLOGY AND EXPERIMENTATION PROCESS

This chapter discusses the experimental methodology adopted to address the research questions of the present study on the properly modeling of solar panels in atmospheric wind tunnels, considering the geometric scale of the test models, air clearance underneath the solar array, and the pressure taps coverage as key practices in need of examination and standardization.

Furthermore, it includes a description of Concordia's boundary-layer-wind-tunnel facility, instruments, and equipment served to develop the experimental work of the present study.

4.1 Building Aerodynamic Laboratory at Concordia University

All tests for the current thesis have been implemented in the Boundary Layer Wind Tunnel (BLWT) at the Building Aerodynamics Laboratory, Concordia University. The blow-down tunnel is of the open-return design with a working section of 1.80 m in width, 12.2 m in length, and has adjustable roof height in the range of 1.40 m to 1.80 m to provide the necessary elevation for different exposures. The plan- and side-views are provided in Figure 4.1. The wind tunnel inlet flow is generated by a MARK HOT double inlet centrifugal blower with a flow rate capability of about 40 m^3/s. The freestream wind speed in the longitudinal direction (streamwise) at the test section can be set between 3.0 m/s and 14.0 m/s.

The tunnel floor is furnished with a polypropylene carpet of a specific roughness height and the ceiling consists of wooden panels of adjustable height to ensure the absence of pressure gradient in the streamwise direction at different terrain exposures. Different terrain exposures would be replicated by adding floor panels with specific roughness elements and configurations. At the test section, the tunnel is equipped with a turntable of 1.60 m diameter through which the
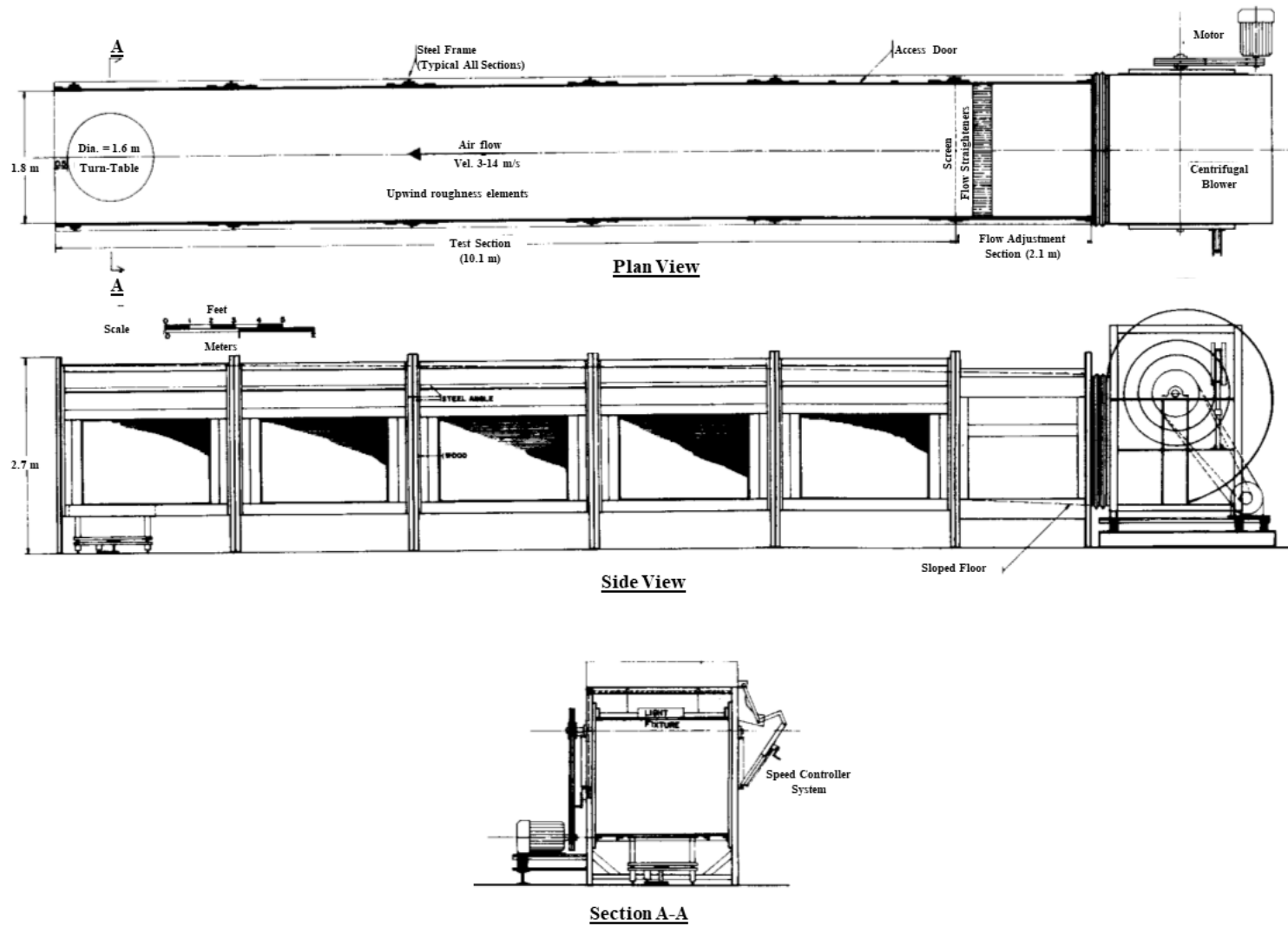
Figure 4.1 Construction plans of the boundary layer wind tunnel at Concordia University (after Stathopoulos, 1984*).*

effect of different wind directions can be examined. This wind tunnel has been used for many codification-oriented studies, i.e., Stathopoulos and Dumitrescu-Brulotte (1989); Stathopoulos and Mohammadian (1991); Saathoff and Stathopoulos (1992); Stathopoulos et al. (2000, 2013); Candelario et al., 2014; and Alrawashdeh and Stathopoulos (2015) , to name a few.

A description of the design and performance of this experimental facility is sufficiently served by Stathopoulos (1984).

4.2 Atmospheric Boundary Layer Simulation

All the experiments have been carried out in a fully developed open-country exposure to maintain the streamwise wind velocity and turbulence intensity similar in the wind tunnel and the field. It is a well-known fact that such a profile is used for codification studies and for studies concerned with generating the design wind pressure coefficients.

The boundary flow of the wind tunnel is developed using triangular boards, a steel plate, and carpet roughness. Four boards of the same triangular shape (spires), each of respectively base width and height of 19 cm and 120 cm, were set up side by side with a center-to-center distance of 36.5 cm on the screen of the tunnel entrance and tied up to the screen. The two end boards are positioned approximately 35 cm from tunnel sidewalls. The thick carpet furnished along the floor generates the intended velocity and turbulence profiles of open-country exposure. Figure 4.2 provides a photograph of the upstream view of the wind tunnel.

Figure 4.3 (b) shows the variation of the mean wind velocity ($\overline{U}$) normalized by the freestream mean wind speed ($\overline{U}_g$) and turbulence intensity ($I_u\%$) with the height above the wind tunnel floor. Both mean velocity and turbulence intensity were measured using a 4-hole Cobra-probe (TFI) at

Figure 4.2 Upstream-view photograph of the boundary layer wind tunnel of Concordia University

the test section in place of the test models. In this figure, Z is the height above the tunnel floor and Z_g is the gradient height above the floor. The freestream wind speed $(\overline{U}_g)$ was set at 12.6 m/s at a velocity scale of 1:3 to duplicate the full-scale gradient wind velocity of 37.8 m/s.

The parameters of the logarithmic law were determined by graphing the measured velocity against the natural logarithmic of the height above the wind tunnel, as shown in Figure 4.3 (a). It is found from the trend line that the roughness length of the simulated wind profile is $z_0 = 6.8 \times 10^{-5}$ m on the wind-tunnel scale. The profiles of the mean wind speed and turbulence intensity are cross-checked and verified with the corresponding profiles of the Standard Open Terrain of ASCE/SEI 7 (2022) with roughness length $z_0 = 0.03$ m and gradient height $Z_g = 273$ m. As illustrated in Figure 4.3 (b), the measured and the standard profiles are mutually compatible, indicating that the geometric ratio for this approaching flow is about 1:500.

For further validating the simulated flow, the simulated boundary flow spectrum is authenticated through fitting the measured wind tunnel flow spectra to the empirical power spectrum model of Kármán (von Karman, 1948) and the analytical model of Davenport (Davenport, 1961). As shown in Figure 4.4, the measured spectrum of the streamwise wind tunnel flow (at $Z = Z_g/4$) shows a fairly good agreement with the corresponding full-scale model spectrum. It should be noted that the von Kármán spectrum shown is generated for an integral scale of $L_{u,x} = 135$ m in full scale.
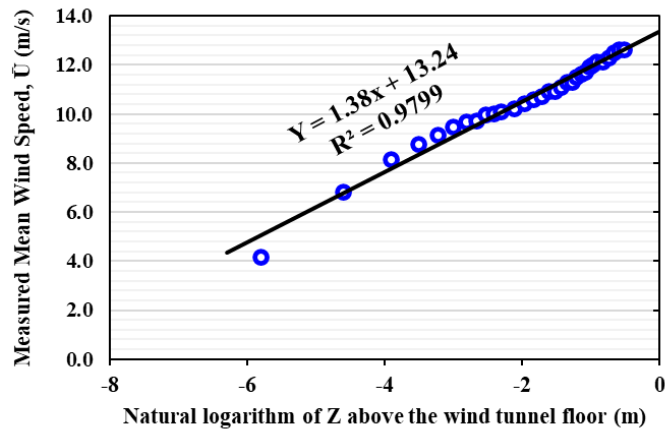
(a)
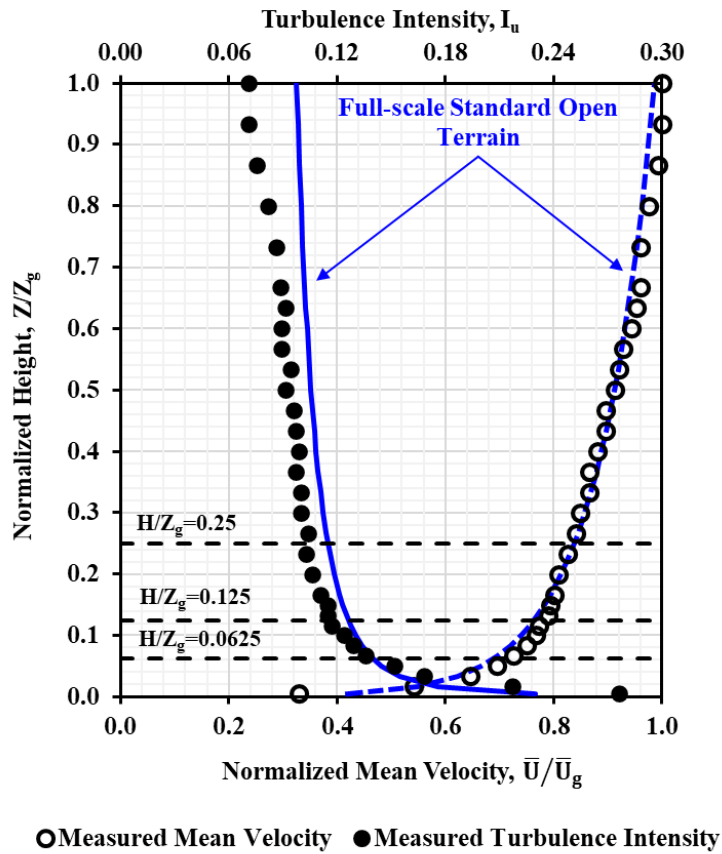
(b)

Figure 4.3 (a) Wind tunnel flow roughness length, and (b) Comparison of the wind tunnel mean wind speed and turbulence profiles with the Standard Open Terrain of ASCE/SEI 7 (2022)
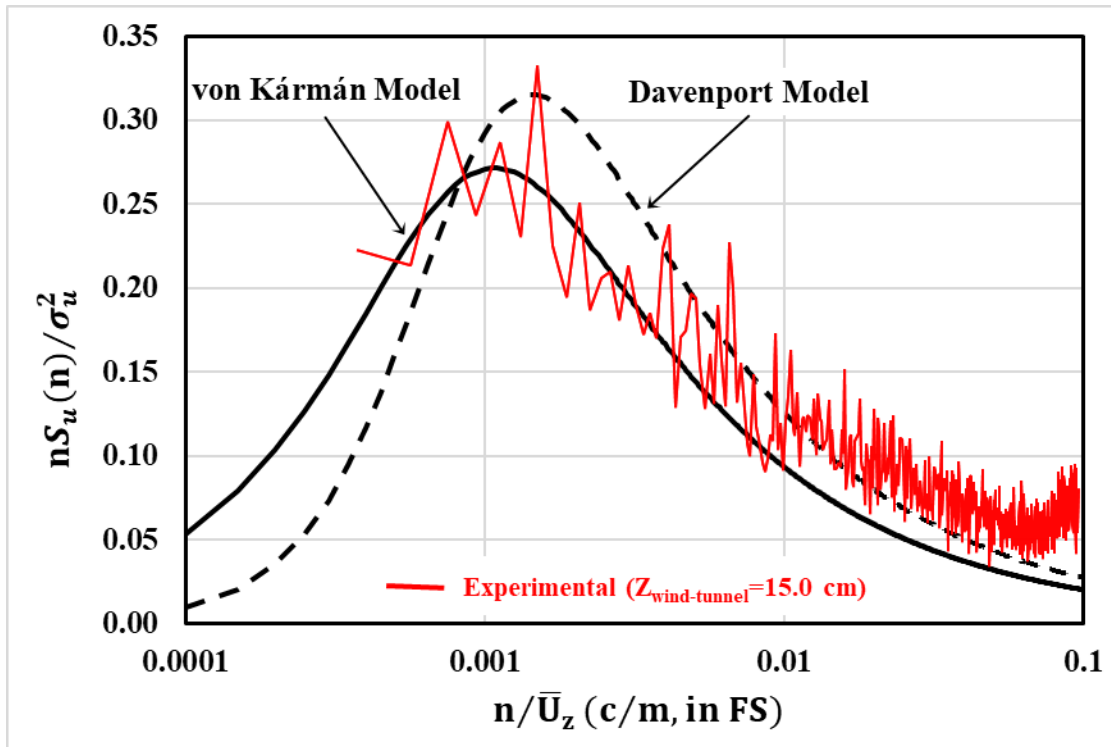
(b)

Figure 4.4 Comparison of the dimensionless spectrum measured at a height Z=0.15 m (above the wind tunnel floor) with the counter-part models of von Kármán and Davenport

4.3 Experimental Models

The selection of the building and the solar array configuration for the present study was guided by the fact that the building plane size has a significant impact on the solar panel wind loading (Kopp et al., 2012; Kopp, 2014; Stathopoulos et al., 2014) and a larger number of panels would lead to better capture the complexity of the wind interaction with the solar panels; and hence, more aerodynamic events are promoted.

A solar array consisting of eight panels (rows) has been considered for the experimental tests. Each panel is composed of 10 PV modules of a standard commercial size (2.0 m in chord length

and 1.0 in width). The array is mounted on a flat roof of a building with 7.5 m height, 14 m width, and 27 m length. Details of the full-scale building geometry and layout are provided in Figure 4.5. As shown, the solar array is placed at an air clearance height of $G = 0.4$ m above the roof and a setback distance of 2.0 m from the roof edges.

It should be mentioned that the testing building has satisfied the ASCE/SEI 49 (2021) requirements for the layout and geometry of solar arrays on buildings to be used for codification purposes.
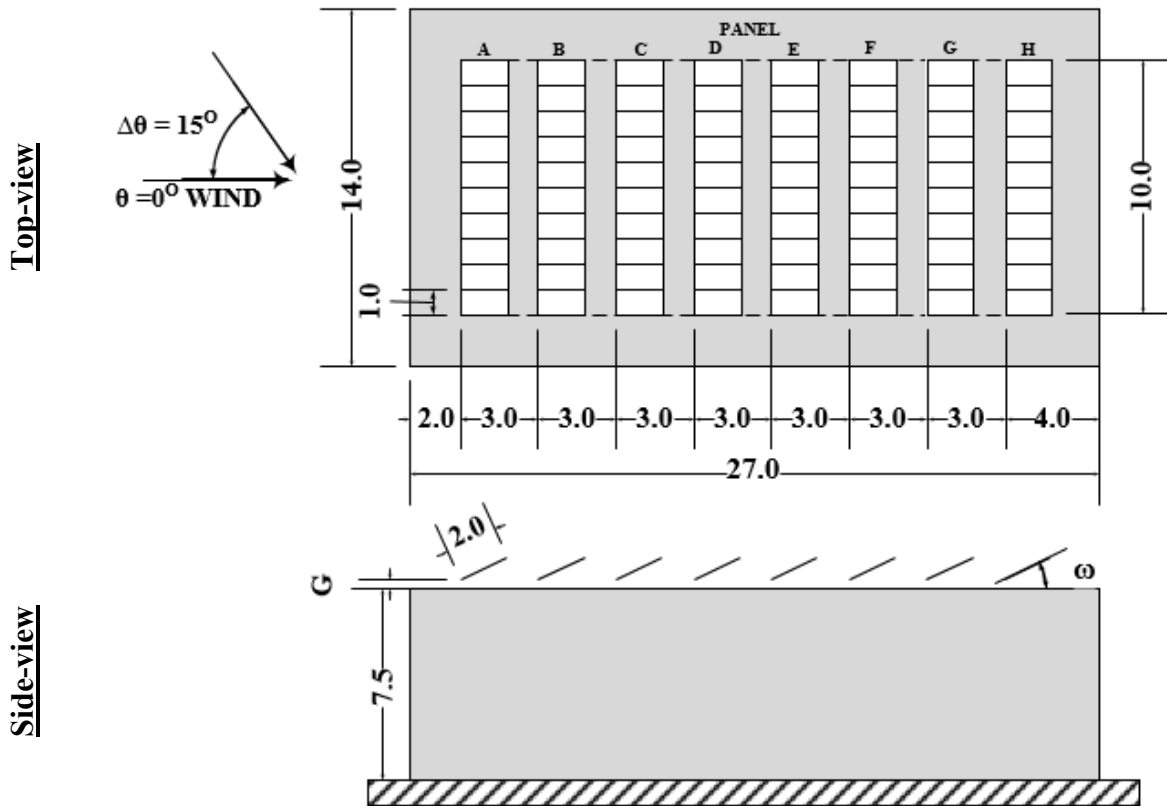
Figure 4.5 Schematic illustration of the full-scale equivalent installation (dimensions in m)

Three sets of models have been designed to separately address the research questions of the

present study. The summary of modeled solar arrays is provided in Table 4.1 with equivalent wind-tunnel dimensions.

Table 4.1 Details of the experimental models in wind-tunnel scale (dimensions in cm and degree)

Research Question	Model Scale	Building Geometry			Solar Panel Geometry			
		Height H	Length L	Width W	Chord length L_P	Span length L_S	Tilt ω	Clearance off Roof G
Geometric scale	1:200	3.75	13.5	7.0	1.0	5	15	0.2
	1:100	7.50	27.0	14.0	2.0	10	25	0.4
	1:50	15.0	54.0	28.0	4.0	20	35	0.8
Air Clearance	1:50	15.0	54.0	28.0	4.0	20	15	0.0 0.4 0.8
Pressure Taps Coverage	1:50	15.0	54.0	28.0	4.0	20	15	0.8

4.3.1 Models for Testing Geometric Scale

Building on the outcome of the study of Hunt (1982) which showcased that results obtained at fully developed flow are less discrepant with the model size, the experimental methodology of the present study gave the highest priority for the simulated atmospheric boundary flow that satisfies the similarity conditions of the longitudinal velocity and turbulence characteristics with the field at full depth at the expense of the model size which is relaxed; and hence, the designed models of the present study are utilized to mainly diagnose the impact of the non-conformity between the simulated approaching flow and the wind tunnel models to be used in the tests. It should be recalled that the simulated atmospheric flow, discussed in Section 4.2, is appropriate for rightfully testing models at the scale of 1:500, but adopting this scale is indeed out of the question as the model will be very small and physically untestable in the wind tunnel.

All things considered, three models are designed and manufactured at three geometric scales (1:50, 1:100, and 1:200). Thus, all geometric details shown in Figure 4.5 are scaled down at the considered scale ratios, including the size of the building, the solar panels size, air clearance, the setback distance from the roof edges, and inter-panels spacing. The array is tilted at three angles, namely ω = 15°, 25°, and 35°. Figure 4.6 (a) represents a photograph for the upstream view of the wind tunnel and the test models. It should be noted that the model of 1:200 scale is the smallest testable model that could be manufactured so that the pressure taps can be inserted from both surfaces, while the model of 1:50 scale is the largest model that could be tested without distorting the wind tunnel blockage limit.

Table 4.2 summarizes the main test parameters for the models involved in the experiments and their similarity in connection with the simulated flow and the field. As indicated, the selection of the experimental models considered in this study (1:200, 1:100, and 1:50) resulted in some dissimilarities between the approaching flow and the models in three aspects, as follows:

(1) The ratio of turbulence integral-scale to building height, $L_{u,x}/H$, in which discrepancies of 1:2.5, 1:5.0, and 1:10.0 between the wind-tunnel simulation and full-scale incur.

(2) The ratio of the building height to roughness length embodied by Jensen's number ($J_e = H/z_0$) shows discrepancies of 1:0.4, 1:0.2, and 1:0.1 between the wind-tunnel simulation and full-scale.

(3) The level of turbulence intensity of the approach flow at the model height is different.

The first and second points above state that the size of the tested models at the scale of 1:200, 1:100, and 1:50 are two and a half-, five-, and ten-fold the rightful size, respectively. Further recalling that the relative height of the model (H/z_0) and the relative length scale of the simulated flow $(L_{u,x}/H)$ shall agree with the field within a factor of 3.0, the model scaled at the
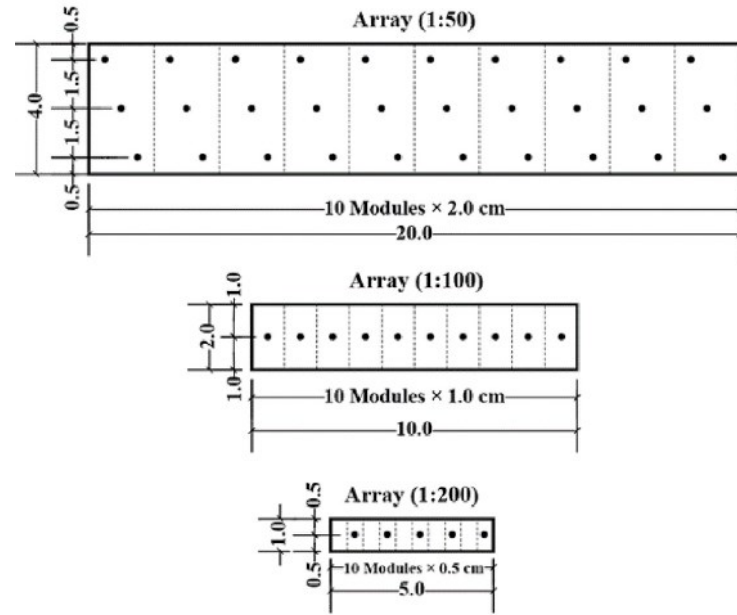
(a)   (b)

Figure 4.6 (a) Upstream view of the wind tunnel with the test models, and (b) Schematic illustration of solar panel

models with pressure taps (dimensions in cm)

Table 4.2 Similarity considerations on the experimental modeling

Geometric Scale	$\left(\frac{H}{z_0}\right)_{WT} : \left(\frac{H}{z_0}\right)_{FS}$	$\left(\frac{L_{u,x}}{H}\right)_{WT} : \left(\frac{L_{u,x}}{H}\right)_{FS}$	$\left(\frac{L_{u,x}}{H}\right)_{WT}$	Blockage ratio (%)	Re_r	$Re \times 10^4$ Based on		I_u (%)
						H	L_P	
1:200	1:0.4	1:2.5	4.5	0.1	2.5	2.3	0.6	14.0
1:100	1:0.2	1:5.0	3.0	0.6	2.5	4.8	1.3	11.6
1:50	1:0.1	1:10.0	1.8	3.6	2.5	10.5	2.8	10.5

ratio of 1:200 fulfills the requirements referred to in ASCE/SEI 49 (2021).

It is worthwhile noting that the Reynolds number of the local flow (e.g., inter-panel flow and the roof-array flow) differ at the geometric scale of the test model. In fact, no specified definition for the Reynolds number of the local flow is provided in the literature, and full-scale measurements would be needed to identify the corresponding field limits of the local flow Reynolds number (Stenabaugh et al., 2015; Naeiji et al., 2017). In the present study, the wind tunnel Reynolds number based on the chord length (i.e., $Re = \overline{U}_H L_P / \nu$) for the scales considered is much greater than the limit of turbulent flow (i.e., $Re \gg 2000$) – as provided in Table 4.2.

The solar panels of the test models were made of thin "sandwiched metallic plates" of a total of 2.3 mm thick. The detailed location of the surface pressure taps for the models of the arrays at the considered geometric scales is illustrated in Figure 4.6 (b). Both surfaces (upper and lower) of each panel are equipped with pressure taps, identical in their distribution. As shown, the panels at geometric ratios 1:200 and 1:100 are equipped with one line of pressure taps on each surface along the center of the panel. The panel at the geometric ratio of 1:50 is equipped with three lines of pressure taps on each surface, along the center and close to the edges of the panel.

4.3.2 Model for Air Clearance

During the experiments of Section 4.3.1, the size of the air clearance of the solar array off the roof has been preserved at the considered scale (i.e., $G = 0.40$ m in full-scale) – See Figure 4.5. Although there is no standard regulation on size of the air clearance above the roof for solar panels tilted on flat roofs, Alberta Roofing Contractors Association (ARCA) standards (Alberta Infrastructure, 2017) requires the solar panels to be installed at a minimum clearance of 30.0 cm above the roof

for construction warranty eligibility considerations.

As indicated in Table 4.1, to experimentally examine the impact of the solar array clearance during the modeling in the wind tunnel and carry out a parametric study, the solar array scaled down at ratio 1:50 with a tilt angle ω = 15° has been placed at two additional clearance heights, including G = 20 cm and G = 0 cm which respectively represent half of the typical clearance and no clearance – see Figure 4.7.
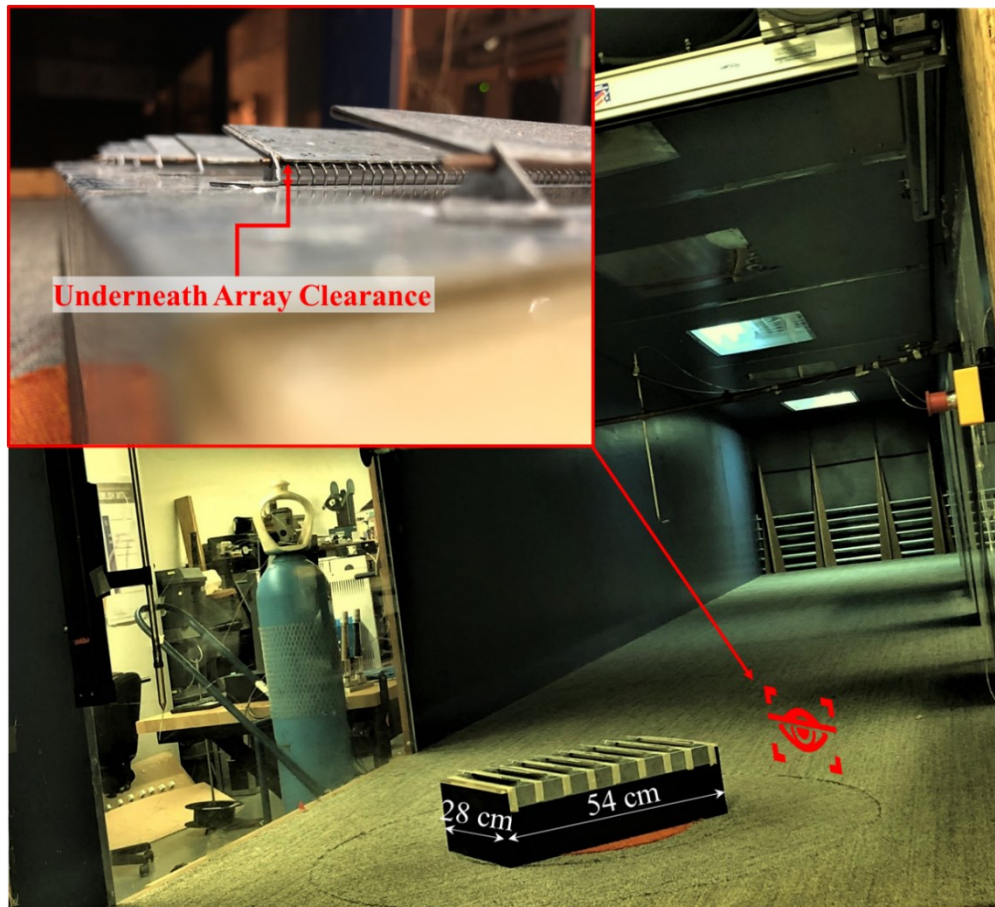
Figure 4.7 Test model in the wind tunnel of Concordia University (panels are placed at typical clearance above the roof, G = 40 cm in full-scale)

In total, the effect of the air clearance will be examined at three heights 0.00, 0.20 m, and 0.40 m in full-scale.

4.3.3 Model for Pressure Taps Coverage

The array scaled down at the ratio of 1:50 with the tilt angle $\omega = 15°$ has been adopted in this investigation, since it is physically equipped with the highest coverage of pressure taps (30 taps on each surface) – see Figure 4.6 (b).

To examine the influence of the pressure taps coverage on the surface and the design net pressure coefficients, the pressure taps coverage at six practical configurations has been presumed – as illustrated in Figure 4.8. These virtual configurations were established to address the research questions on this experimental practice from various aspects, including the taps' location, density, and alignment on the panel's surfaces.

Pressure taps coverage at configurations named 1 to 5 is mirror-image on the panel upper and lower surfaces, while pressure taps at configuration 6 have different pressure taps coverage on each surface. It should be stated that Configuration 5 will be used as a benchmark for comparisons making with other configurations.

4.4 Instrument and Data Acquisition

Two independent measurement systems have been utilized to conduct the experimental work of the current thesis. The first system, a dynamic multi-hole pressure probe called Cobra Probe, was used to measure the turbulence intensities, mean wind speeds, and turbulence spectrum. The Cobra
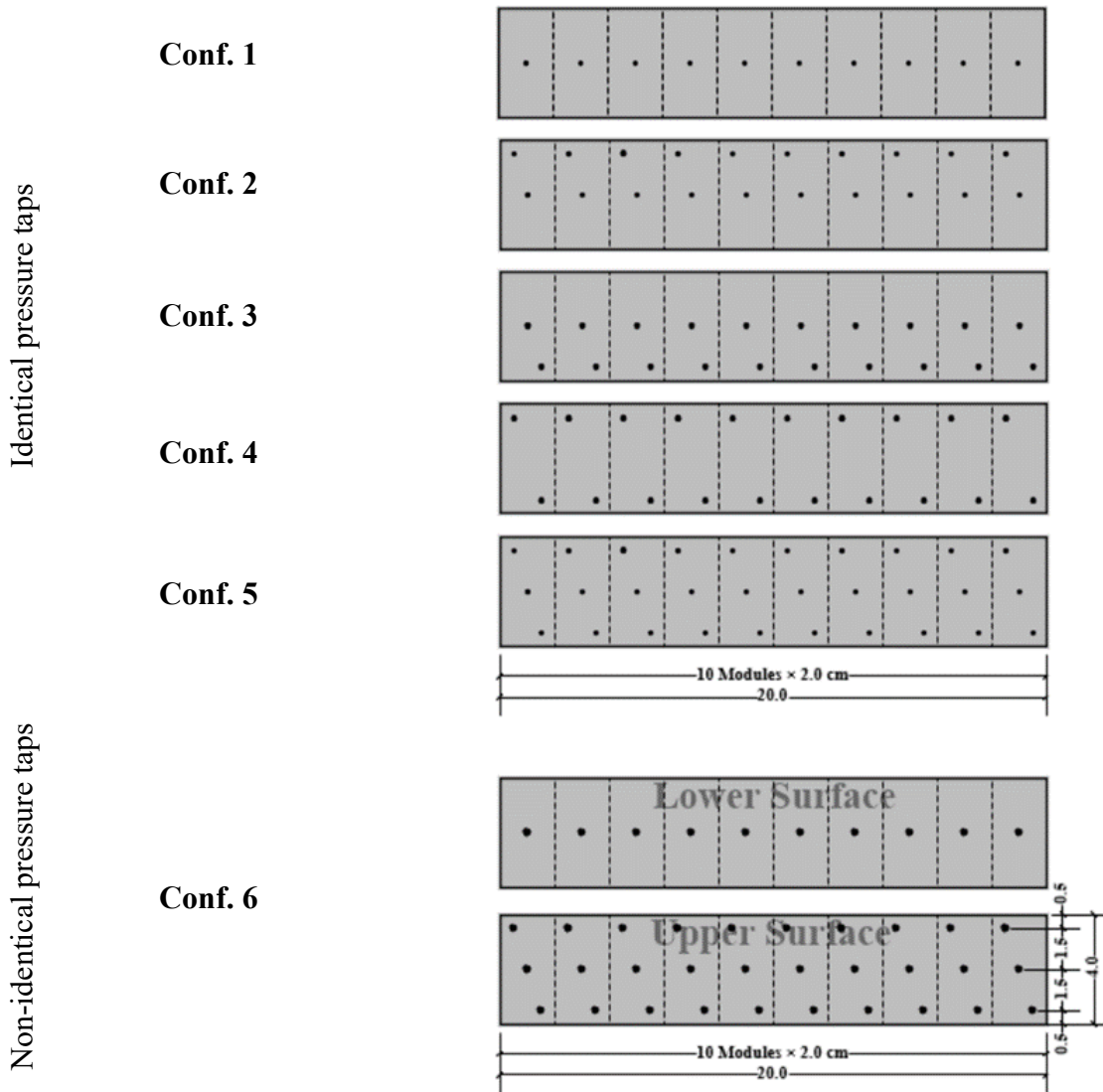
Figure 4.8 Typical solar panel with different pressure taps configurations: Identical (Conf. 1 to 5 and Non-identical (Conf. 6) on the surfaces

Probe is manufactured by Turbulent Flow Instrumentation (TFI) company. The Cobra Probe body, which has an overall length of 15.8 cm, comprises four of 0.5 mm pressure taps in a multi-faceted head and pressure transducers through which the three components of the wind velocity and turbulence intensities are measured. The Cobra Probe is attached to the axis of a three-dimensional traversing system through which the Cobra Probe can be moved remotely in three dimensions

53

inside the wind tunnel – See Figure 4.2. The Cobra probe is connected to a computer with a Windows operating system to collect the measurement results during the testing process.

The second system, sensitive pressure scanners, was used to measure the wind induced pressures on models. The system consists of a Digital Service Module (Model DSM 3400) and Miniature Pressure Scanners (ZOC33/64 Px) manufactured by Scanvalve. DSM 3400 is designed to be connected up to eight Miniature Pressure Scanners of 64 channels each. DSM 3400 incorporates an impeded computer, RAM, and a hard disk drive and works with windows embedded XP as an operating system. The DSM 3400 module is designed to interface Miniature Pressure Scanners to digital Ethernet system. For insulation purposes, the ZOC scanner is placed inside a thermal unit to maintain the temperature of the scanner constant during the scanning process. PC-computer with windows interface is utilized to host the DSM 3400 system through an Ethernet network and to control the data acquisition by the ScanTel program.

The surface pressure taps are connected to the channels of the Miniature Pressure Scanner using urethane tubes of 550 mm length (URTH-063 for use on 1.6 mm outside diameter stainless steel channels). Traditional custom-made brass restrictors were placed within the tubes at a distance of 300 mm from the model pressure tap to add damping to minimize the Gain and Phase shifts of pressure signals due to Helmholtz's resonance effects. The cross-section diagram of the wind tunnel and wind tunnel facilities set up is schematically presented in Figure 4.9.

The time history wind pressures on the solar panel surfaces at the measurement pressure taps are measured in the wind tunnel for all considered wind directions. As shown in Figure 4.5, the measurements were carried out for wind directions from 0° to 180° at increments of 15°. Considering similarity requirements, geometric (H), time (T), and velocity ($\overline{U}$) scales in the wind tunnel must be in parity with respective atmospheric conditions; therefore, the time scale of the

Inlet Section Flow Transition Section (12.8 m) Test Section (2.1 m)

Triangular boards

Pitot tube

Total (stagnation)
Pressure, Pt

Static Pressure, Ps

Pressure tap (i)

Turn Table

ZOC33/64 Px

Pi
Pt
Ps

DSM 3400

Pi-Ps
Pt-Ps

Air Supply (65 Psi)

$Cp=\dfrac{Pi-Ps}{Pt-Ps}$

Host Computer

Pressure Scan
Computer
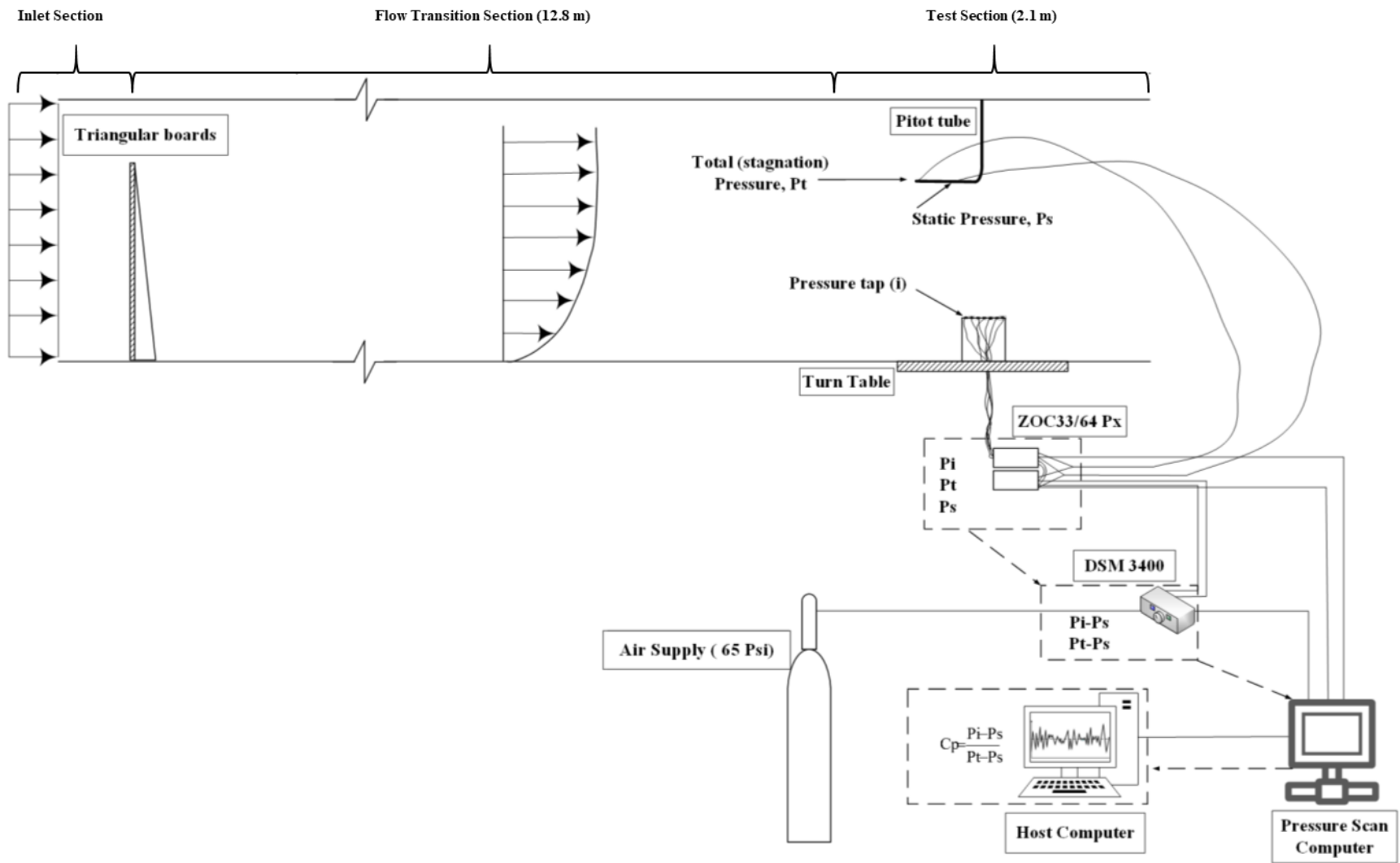
Figure 4.9 Schematic illustration of the wind tunnel instrumentation and measurement systems (after Alrawashdeh, 2015)

55

pressure measurements are determined in combination with the geometric and velocity scales as follows:

$$\frac{T_{WT}}{T_{FS}} = \frac{\overline{U}_{FS}}{\overline{U}_{WT}} \times \frac{H_{WT}}{H_{FS}} \qquad\qquad 4.1$$

in which the subscripts FS and WT refer to full scale and wind tunnel, respectively.

Accordingly, the time scale of the pressure measurement records of the tested geometric scales 1:50, 1:100, and 1:200, considering a velocity scale of approximately 1:3, are respectively 1:17, 1:34, and 1:68. The pressure scanners are calibrated to scan the pressure signals at a frequency of 300 Hz for a total period of 27 sec on the wind-tunnel scale, and therefore the 27 seconds of pressure records are equivalent to 450, 900, and 1800 seconds in full-scale for the tested geometric scales 1:50, 1:100 and 1:200, respectively. For "like to like" comparison, adjustments were applied to the pressure records associated with solar arrays of scales 1:50 and 1:100 to reference them to 1800-sec dynamic velocity pressure using the well-known Durst curve (Durst, 1960).

The integrity of the instrumentation setup and measurements was evaluated based on two sound technical procedures, including obtaining the dynamic pressure of the freestream flow by two independent systems available in the wind tunnel (i.e., Cobra Probe and Miniature Pressure Scanners) and by conducting repeatability (reliability) tests for specific experiments. Within an acceptable margin of error on the surface pressure coefficients, which is about 5%, the instrumentation setup and measurements were validated.

4.5 Data Analysis Procedure

The non-dimensional wind pressures of a particular measurement tap either on upper or lower surface - as laid down in Figure 4.6 (b) - is given by the instantaneous pressure coefficient, $C_p(t)$,

as:

$$C_p(t) = \frac{P(t) - P_0}{\frac{1}{2}\rho \bar{U}_H^2}$$

4.2

in which P is the measured wind pressure at the tap, P_0 is the freestream static pressure, ρ is the density of the air, and $\bar{U}_H$ is the mean value of the wind velocity at roof height (H).

The instantaneous local net pressure coefficient (referred to as force coefficient) is provided as the pressure difference between the upper and lower surfaces at a particular location, as follows:

$$C_F(t) = C_{P,Upper}(t) - C_{P,Lower}(t)$$

4.3

in which $C_{P,Upper}(t)$ and $C_{P,Lower}(t)$ are respectively the instantaneous wind pressure coefficients of the counterpart measurement taps on upper and lower surfaces at a particular location on the panel. It should be noted that the upper and lower surface of the panel is the surface facing the sky and the building roof, respectively.

In addition to the local pressure and force coefficients obtained respectively by Equations 4.2 and 4.3, force coefficients versus the effective wind area of the panel, as called the area-averaged force coefficients, are also the focus of the present study's attention. The instantaneous area-averaged force coefficients over effective panel area (A) are calculated for each wind direction by simultaneously integrating the local wind force coefficients after being factored by the contributing area to each location being considered in the effective area, as follows:

$$C_{F,A}(t) = \frac{1}{\sum_{i=1}^{n} A_i} \sum_{i=1}^{N} C_{Fi}(t) \times A_i$$

4.4

in which $C_{F,A}(t)$ is the area-averaged wind force coefficients at an instant (t), A_i is the contributing area to the ith local force coefficient, and N is the number of local force coefficients in the specified

area ($A = \sum_{i=1}^{N} A_i$).

The area-averaged force coefficient is determined for various effective areas (A) ranging from 2.0 m^2 (area of one module) to 20.0 m^2 (area of entire panel) with an increment of a module area (2.0 m^2). For each effective area, the force coefficient has been calculated at every possible existence on the panel. By way of illustration, Figure 4.10 shows the possible effective wind areas of force coefficients that correspond to an area of three modules ($A = 6.0$ m^2).
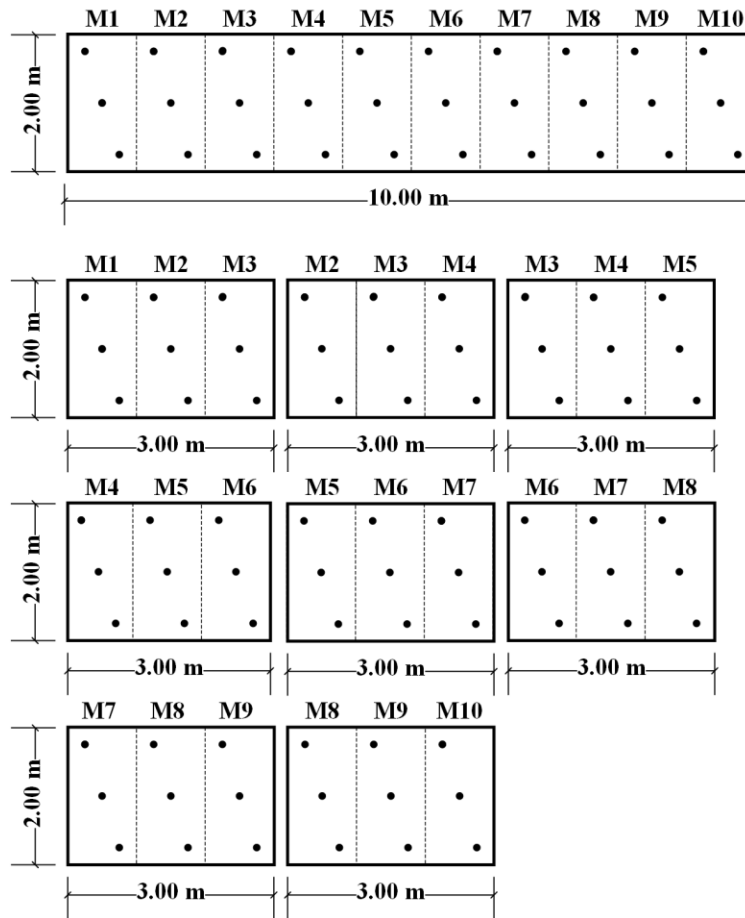
Figure 4.10 Illustration for possible effective areas for C_F and GC_F corresponds to 6.0 m^2

As illustrated in Figure 4.10, there are 8 possible effective wind areas within the panel area for the

force coefficients. The same operation is applied to calculate the force coefficients at effective wind areas ranging between 2.0 m^2 and 20.0 m^2 (e.g., 9 effective wind areas are considered to determine the force coefficient of $A = 4.0$ m^2). In the ultimate analysis, 55 effective areas are considered for the calculation of the area-averaged force coefficients for each panel at each wind direction. If the effective wind area (A) is equal to the area of a module or a panel, the area-averaged force coefficient is referred to as module force coefficient and panel force coefficient, respectively.

The mean and peak values of the time histories of the surface pressure coefficients and the force coefficients obtained by Equations 4.2, 4.3, and 4.4 are determined. The mean coefficient values (C_P and C_F) are taken as the average of the records in the time history; whereas, the peak values (GC_P and GC_F) are calculated as the average of the maximum or minimum 10 records over the time history for the positive and negative peaks, respectively.

Figure 4.11 depicts the sign convention adopted for the key measurement results provided in this thesis. Accordingly, the surface mean and peak pressure coefficients (C_P and GC_P) are positive when the pressure acts towards the surface; negative when the pressure acts away from the surface (suction).
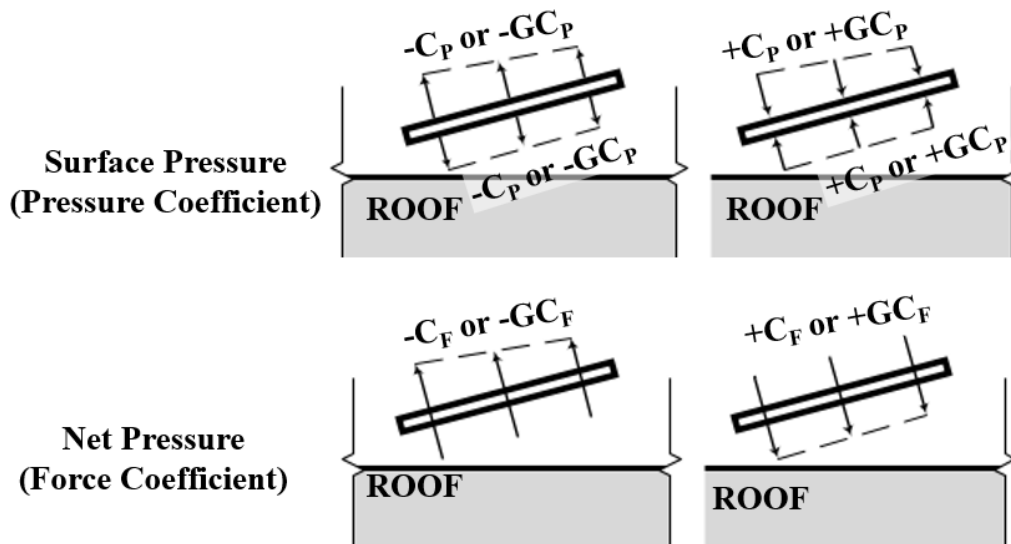
Figure 4.11 Sign conventions for the pressure coefficients and force coefficients

Also, the local and the area-averaged mean and peak force coefficients (C_F and GC_F) are negative if the net pressure tends to peel off the solar panel away from the roof and positive when the net pressure tends to push the array towards the roof.

Finally, it should be noted that the interpretation of the negative results (i.e., pressure and force coefficients) throughout the thesis is provided in absolute sense without regard to their sign.

CHAPTER 5 EFFECT OF GEOMETRIC SCALE

In terms of enlarging the geometric scale of the test models, the results of pressure coefficients developed on the upper and lower surfaces of the panels of the considered arrays will be discussed. Furthermore, the force coefficients will be examined and compared. It should be recalled that models at geometric ratios 1:100 and 1:50 are considered enlarged, while model at 1:200 geometric ratio is the most rightful one that fully satisfies the ASCE/SEI 49 (2021) requirements for modeling in the wind tunnels.

Results provided in Sections 5.1 and 5.2 are confined only to the array at tilt angle $\omega = 15°$ as considered as a demonstrative case, while results of Section 5.3 are obtained on arrays at tilt angles of 15°, 25°, and 35°.

A portion of the work presented in this chapter has been published in the Journal of Wind Engineering and Industrial Aerodynamics (Alrawashdeh and Stathopoulos, 2020) and presented at several conferences (Alrawashdeh and Stathopoulos, 2019a, 2019b, 2022a, 2022c).

5.1 Pressure Coefficients of Upper and Lower Surfaces

In this section, the results of pressure coefficients produced on the upper and lower surfaces of the panels of the considered arrays will be discussed. In approaching this issue, the mean and peak values will be explored against the wind direction.

5.1.1 Mean Pressure Coefficients

It is recognized that the distribution of surface mean pressure coefficients is important to

understand the flow development around the array. Responding to that fact, the distribution of mean pressure coefficients on the upper and lower surface of the panels at the considered geometric test scales 1:200, 1:100, and 1:50 will be followed and assessed. Figure 5.1 shows the variation of the mean wind pressure coefficient (C_P) for the lower and upper surface for solar modules located at the middle of the arrays of the considered geometric test scales.

As shown, the upper and lower surfaces have often exposed negative mean pressures. The lower surface mean pressures are generally higher than the mean pressure coefficients of the upper surface for wind direction between 0° and 75°. Conversely, the opposite trend is observed with respect to the distribution of the surface mean pressures at wind direction between 105° and 180°.

As can be seen in Figure 5.1, relaxing the geometric scale has affected the mean pressures of the upper and lower surfaces. With enlarging the test model, the upper surface mean pressure coefficients obtained at wind directions from 0° to 75° of all panels except the front (A) are decreased showing discrepancies of a factor within 0.6 and those obtained at wind direction from 105° to 180° are increased by discrepancies in a range up to 1.7. Also, the mean pressure coefficients of the lower surfaces are generally decreased with enlarging the test model showing higher disparities of the range down to 0.6 and 0.2 for wind directions from 0° and 75° and 105° to 180°, respectively.

To further realize the underlying causes of the disparities of the surface mean pressure coefficients, particularly in view of relaxing the geometric test scaling, reference is made to computational studies carried out by Wang et al. (2020a and 2020b) for additional details of the flow patterns around solar panels mounted on flat roofs.

According to Wang et al. (2020a), the largest negative mean pressure coefficients induced on upper and lower surfaces of the solar panels at 0° and 180° wind directions are mainly connected with
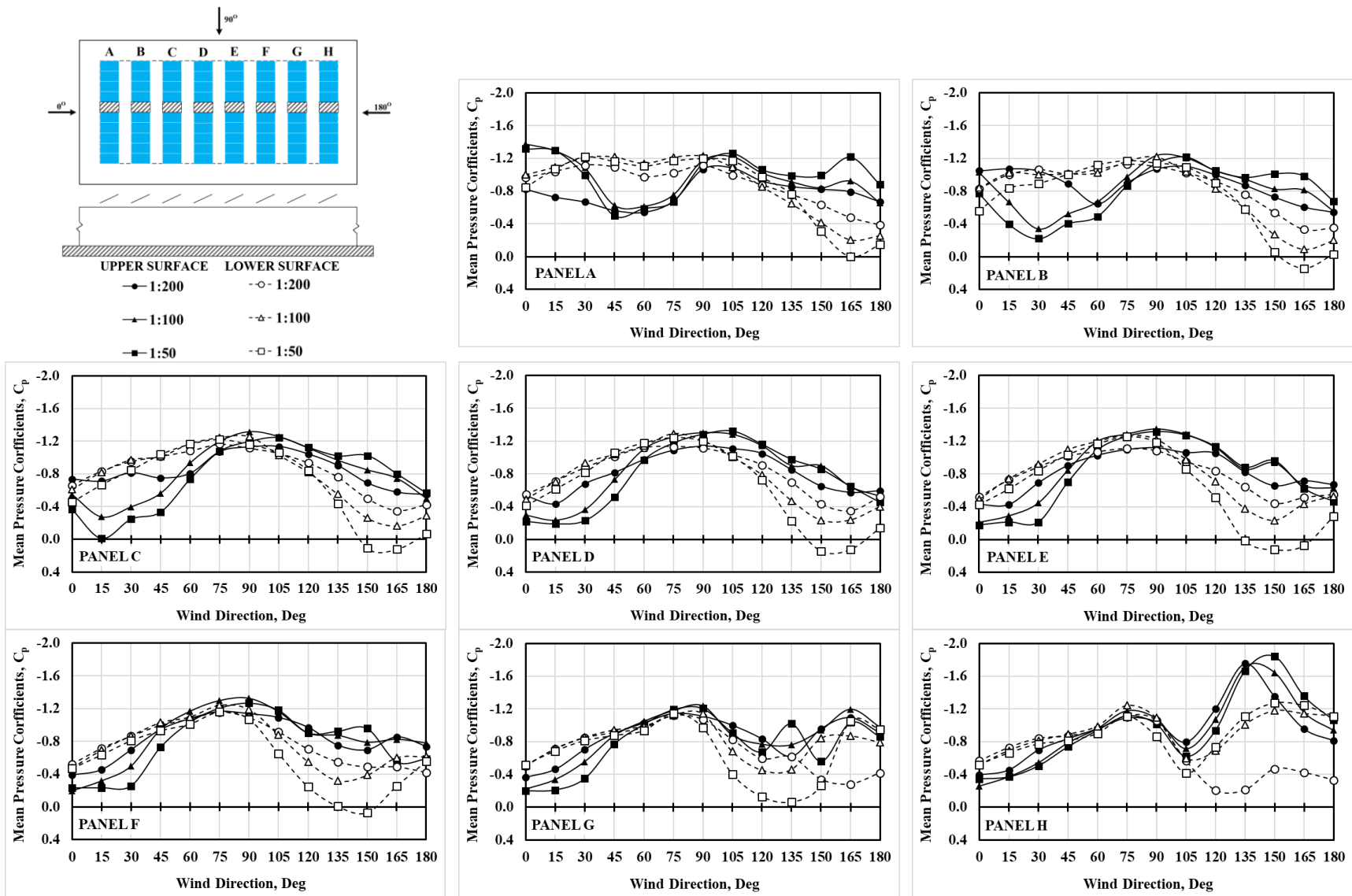
Figure 5.1 Variation of mean pressure coefficients (C_P) over the lower and upper surfaces of modules located in the middle of the array (marked with ▨) with the wind direction

the interaction of the reverse flow of large-scale separation bubble, developed due to the incoming flow interaction with the windward building edge, with the windward panels and the interaction of the forward reattached flow with the leeward panels, which are responsible for producing local vortices on the panel surfaces. Also, Wang et al. (2020b) have investigated the flow pattern at the oblique wind directions (i.e., 45° and 135°). Two conical vortices have been generated from flow separation at the windward edges of the building. The interaction among these conical vortices and solar panels has yielded localized phenomena, such as wake regions and stagnation points beneath the solar panels and separation bubbles above the panels, which are very influential in impacting the surface and net pressures. For this reason, the distribution of mean pressure coefficients of the upper and lower surfaces will be traced on models located in the middle, windward edge, and leeward edge of the array for 0°, 45°, 135°, and 180° wind directions; as provided respectively by Figures 5.2, 5.3, and 5.4.

Figure 5.2 shows the distribution of the mean pressure coefficients over the lower and upper surfaces along the center of the array for the wind blowing perpendicular to the building wall (0° and 180° wind direction). For 0° wind direction, the lower surface mean pressure coefficients of the downstream panels (F, G, and H) show good similarity, whereas increasing variance is observed towards the upstream panels among the considered scales. Similar values are observed on the modules of 1:200 and 1:100 arrays, but much greater than the corresponding values of the 1:50 panel.

Following the distributions of the surface mean pressure coefficients at 0° wind direction provided in Figure 5.2 (a), the upper surface mean pressure coefficients of the 1:200 array show little variation along its panels. Whereas, the mean pressure coefficients of the 1:100 and 1:50 solar panels have been rapidly decayed along the panels in the downstream direction. Also, the lower

surface mean pressure coefficients of the considered arrays show gradual decay for 0° wind.

Generally, the lower and upper surface mean pressure coefficients are decreased with enlarging

(a)

(b)

Figure 5.2 Distribution of mean pressure coefficients (C_P) over the lower and upper surfaces of PV modules located at the center of the array for: (a) 0° and (b) 180° wind direction

the test model, except the mean pressure on the upper surface of the upstream panel (Panel A). This is due to the background of the freestream which has greatly affected the upper surface mean pressure coefficients of the panel (A), in that the array models of larger size are placed at a lower

level of turbulence. Moreover, the discrepancy of the lower and upper surface mean pressure coefficients of the downstream panels among the considered scales is likely due to enlarging the size of the solar panel which has played a role in impacting the local flow separation at tips of the panels and lowering the intensity of the vortex shedding; and hence, lowering the suction on the panel surfaces of the larger array.

The distribution of the lower surface mean pressure coefficients of the 1:200 array provided in Figure 5.2 (b) shows little variation along its panels, where the values of pressure coefficients are increased along the first four upstream panels and then start to slightly decrease in the downstream direction; whereas, the lower surface mean pressure coefficients of the 1:100 and 1:50 arrays have been gradually decayed along the panels in the downstream direction for 180° wind direction.

As can be seen in Figure 5.3 for the mean pressure coefficients obtained at 45° wind direction, the mean pressure coefficients of the lower surface of different modules locations show good similarity among the considered scales. On the other hand, the upper surface mean pressure coefficients show discrepant results with decreasing tendency against enlarging the test model for modules located in the middle and in the leeward edge of the array. The upper surface mean pressure coefficients of the modules in the windward edge show an increasing tendency with enlarging the test model. Running off the downflow streams of the large-scale conical vortex over the upper surface of the windward edge modules has yielded higher upper surface negative suction on the larger array. This may be attributed to the characteristics of the flow background (i.e., the 1:50 array is placed at a lower level of turbulence), which played a role in elevating the upper surface mean pressure.

Regarding the upper surface mean pressure coefficients of the modules on the middle and the
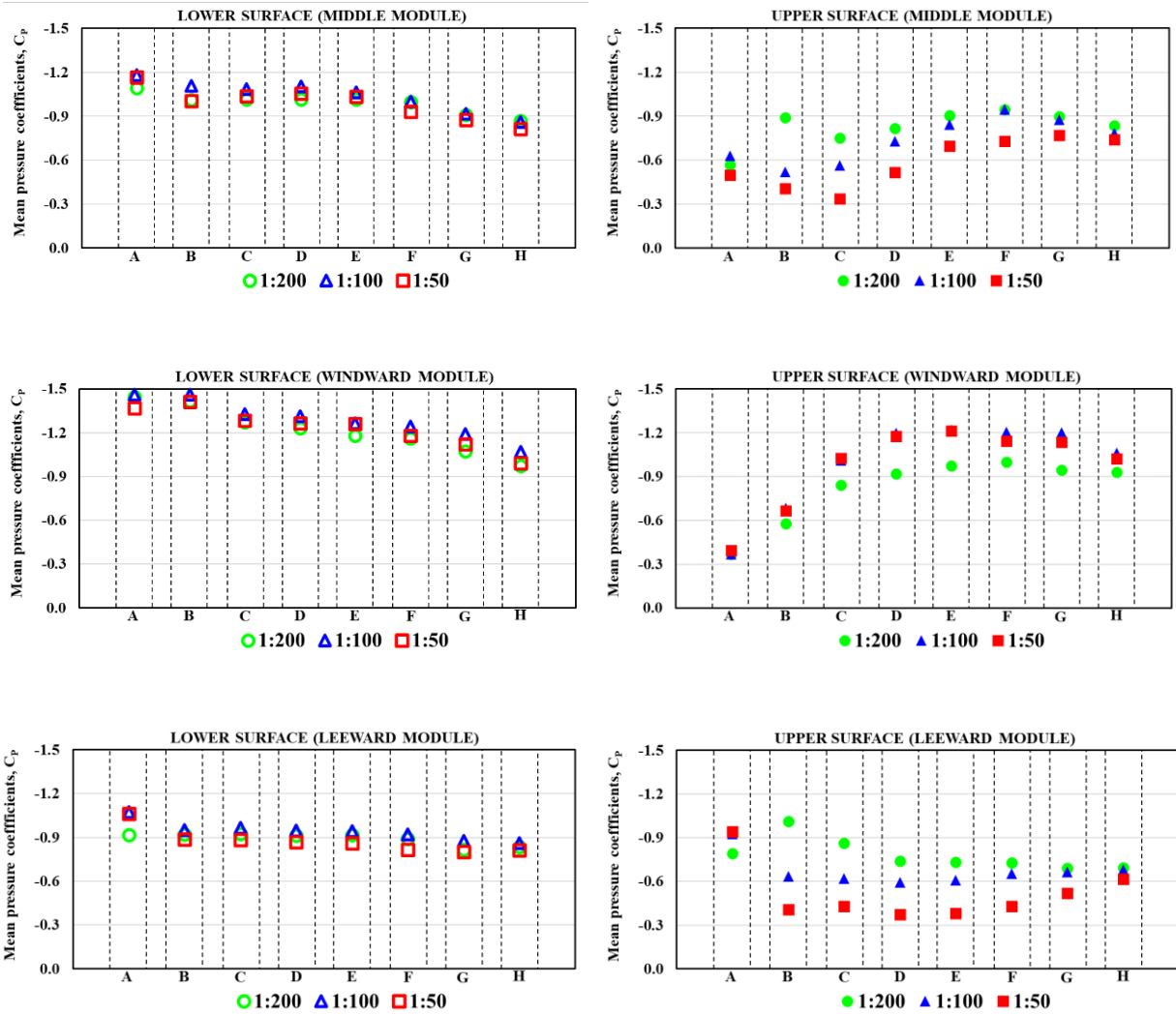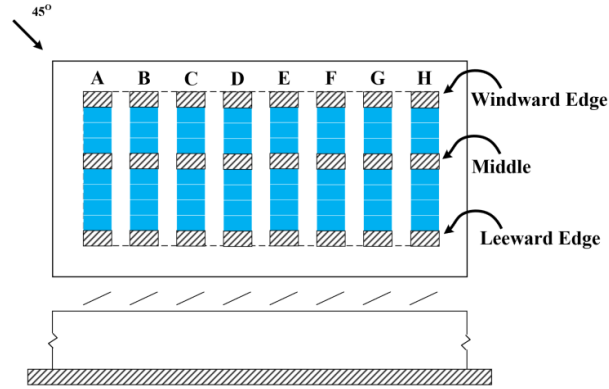
Figure 5.3 Distribution of mean pressure coefficients (C_P) *over the lower and upper surfaces of*

PV modules located at middle, windward edge, and leeward edge of the array for 45° wind

direction

leeward edge of the arrays shown in Figure 5.3, the decreasing tendency on the mean pressure coefficients with enlarging the test model is attributed to the intensity of the vortex shedding of the local separation developed at the tips of the panels, as these modules are unlikely being affected by the large-scale conical vortex at the building edges.

To some extent, an opposite trend was observed regarding the surface mean pressure coefficients at 135° wind direction, provided in Figure 5.4. The upper surface mean pressure coefficients of the modules at different locations of the array (middle, windward, and leeward edge) among the considered scales are in good similarity except for the back-panels (G and H). Whereas, the lower surface mean pressure coefficients of modules located in the middle and leeward edge of the array show clear decreasing tendencies with enlarging the geometric test scaling. The most likely scenario describes that the downflow streams of the large-scale conical vortex are separated at the tips of the modules producing a wake region beneath the panels and separation bubble on the lower surface. With larger panels (i.e., longer chord length), the downstream flow of the conical vortex has enough space to roll over the panels and producing a non-confrontational separation at the tips of the panels which results in vortices on the upper surface of lower intensity and wake region of lower vortex frequency. On the modules of the upstream panels (G and H), it is clear that the induced suctions on the panels' surfaces have been mostly dominated by the background characteristics of the freestream flow (i.e., higher mean suction produced on the larger model).

The observations made on the mean pressure coefficients at 0°, 45°, 135°, and 180° wind directions in view of relaxing the size of the test model may reflect the importance of the accurate similarity of geometric test scale between the approach flow and the solar panels to ensure the validity of the flow field developed around roof-mounted solar panels. It is observed that enlarging
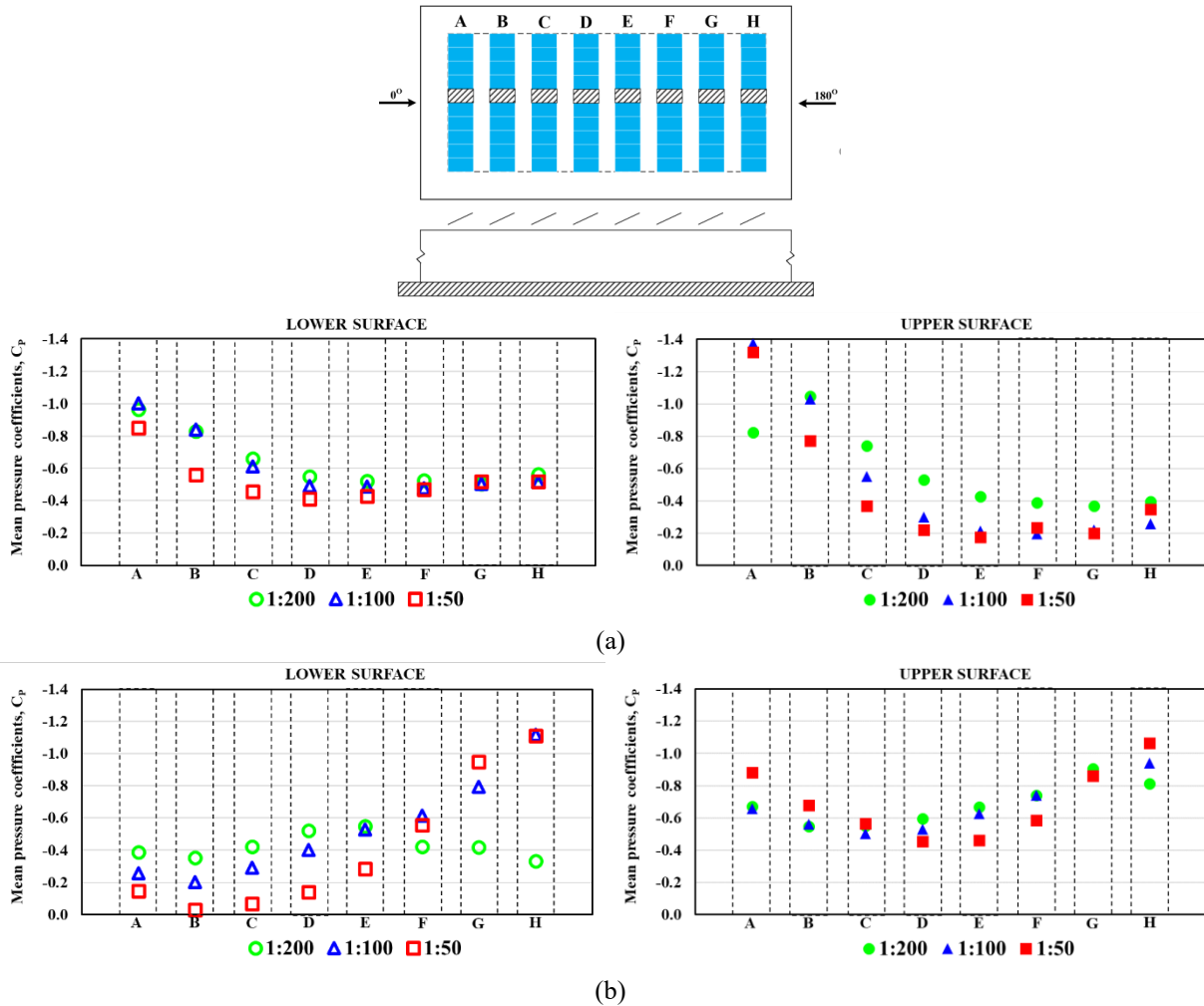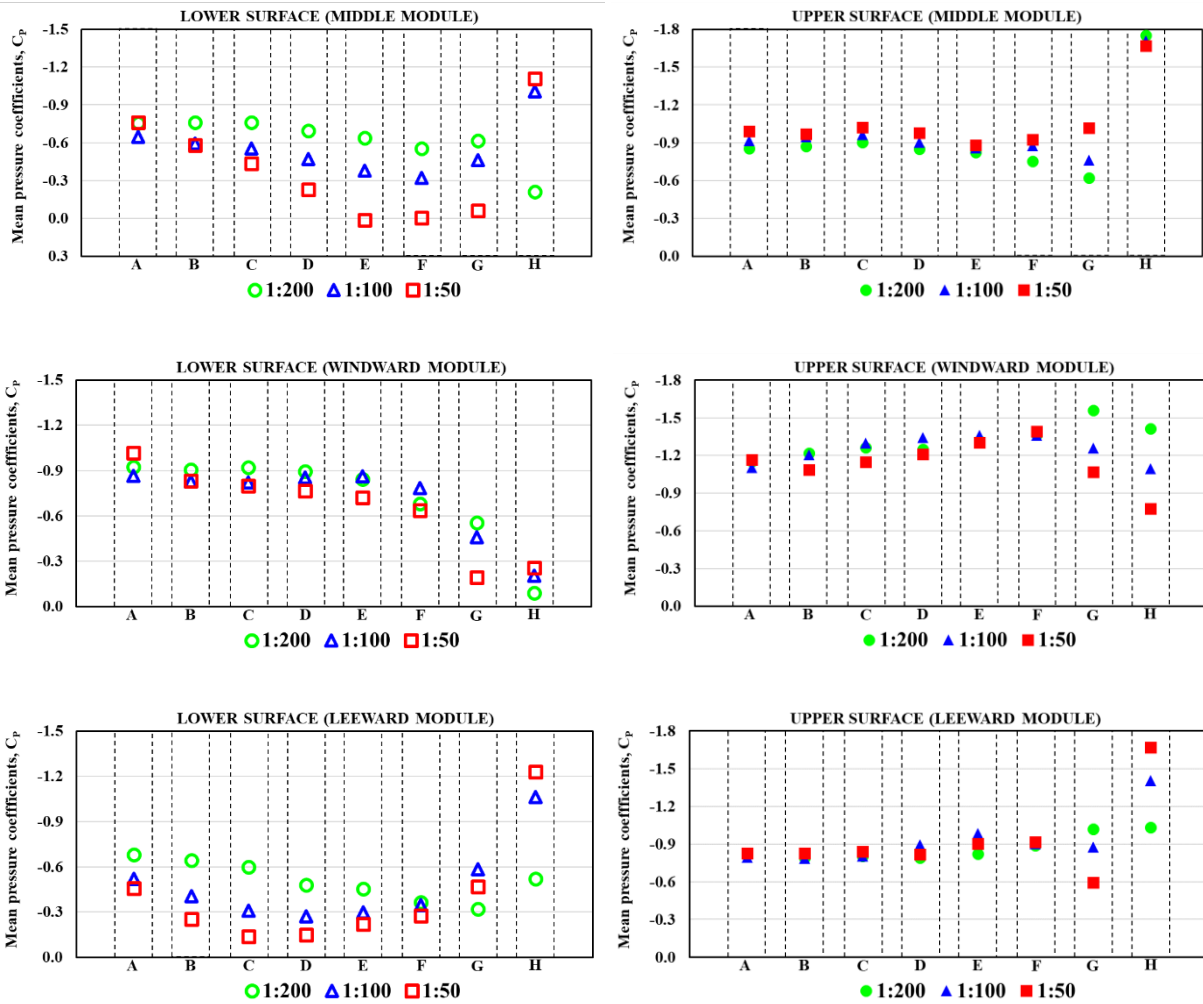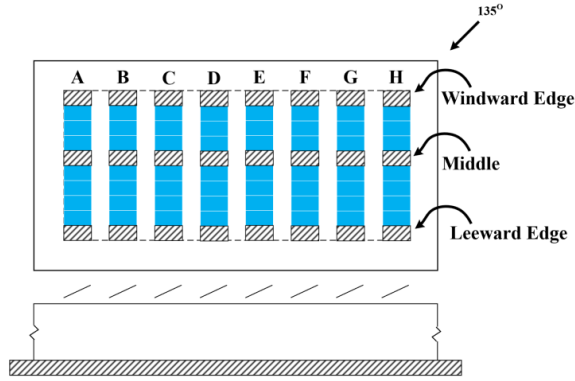
Figure 5.4 Distribution of mean pressure coefficients (C_P) over the lower and upper surfaces of PV modules located at middle, windward edge, and leeward edge of the array for 135° wind direction

69

the size of the test model exhibits the greatest influence clearly on wind-induced surface pressure of the downstream modules (i.e., those away from the freestream-building generated separation bubble or conical vortices), where the surface pressure of these modules is largely dominated by the local flow developed at the panels' tips with decreasing scale of influence.

A likely scenario would suggest that larger models enable larger space for the building-generated flow to be tamed, which may result in reducing the curvature of the local separation developed at the modules' tips; hence the strength of the vortices shed from the panels' tips may be strongly attenuated compared to the smaller models. On the other hand, the surface pressure of the upstream panels (i.e., the upper surface of the front-panel A at 0° wind direction, the lower surface of the back-panel H at 180° wind direction, and the upper surface of edge modules at oblique winds) greatly influenced by the characteristics of the freestream flow, as the mean pressure coefficients on these surfaces among the scales show congruent behavior tendency of roof pressures of low-rise buildings.

5.1.2 Negative and Positive Peak Pressure Coefficients

In the same manner, the impact of relaxing the geometric scale is assessed on the negative peak and positive peak pressure coefficients on the lower and upper surfaces. Figure 5.5 shows the distribution of negative and positive peak pressure coefficients (GC_P) of the upper and lower surface of modules located in the middle of the array versus the wind direction. The upper and lower surfaces are particularly vulnerable to negative peak pressure coefficients. However, solar panels of larger scales (1:100 and 1:50) have exposed positive peak pressure on the upper surface for wind directions of 0°, 15°, and 30° and on the lower surface for wind directions of 150°, 165°,
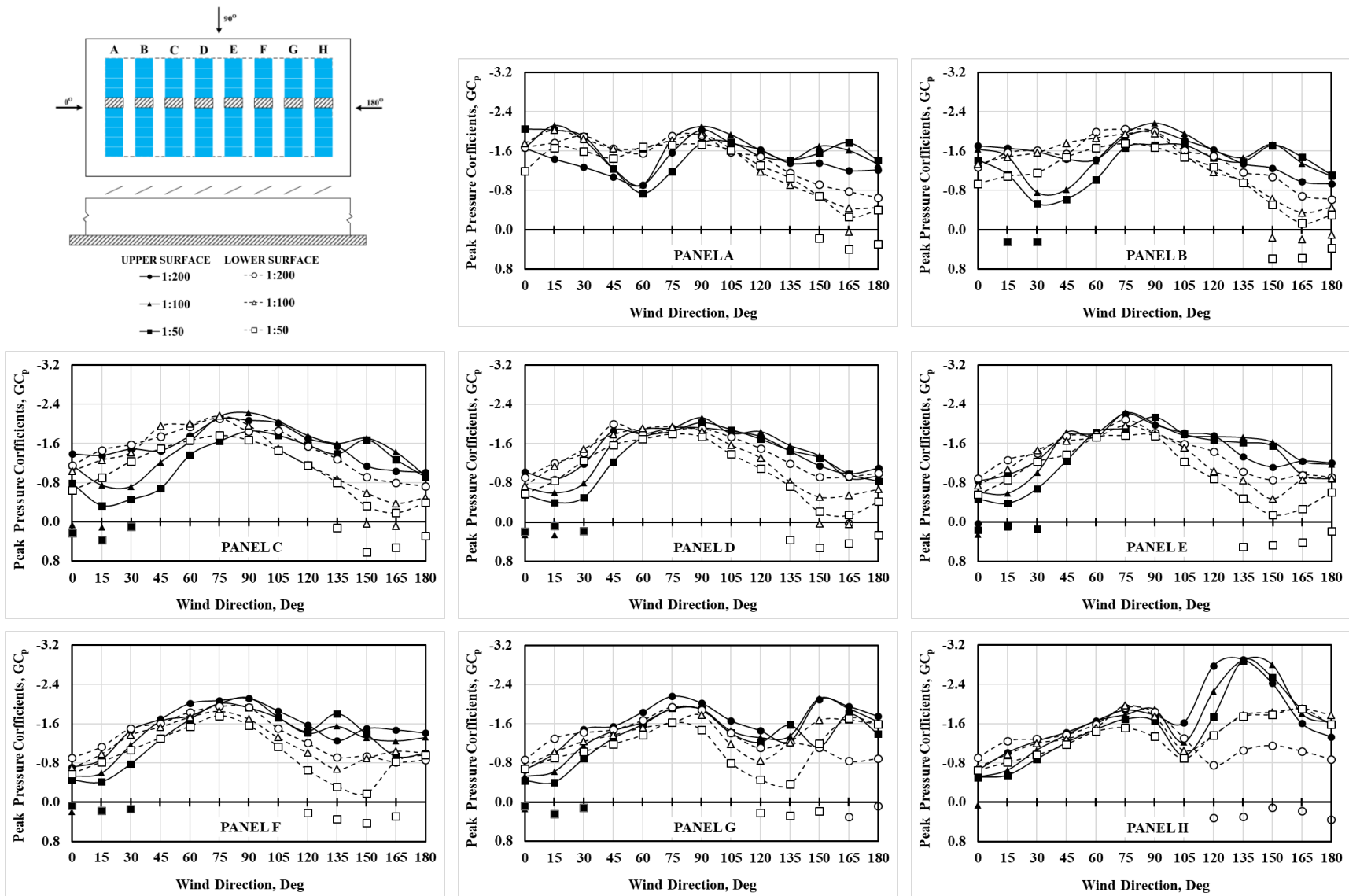
Figure 5.5 Variation of negative and positive peak pressure coefficients (GC_P) over the lower and upper surfaces of PV modules located in the middle of the array (marked with ▨) versus wind direction

71

and 180° with a peak pressure coefficient value did not go beyond +0.6. A similar pattern for each panel is exhibited, as the negative peak pressure coefficients for wind direction range from 0° and 75° on the lower surface are found to be higher than those on the upper surface, but less for winds range from 105° and 180°.

As for the effects of enlarging the test model, strong parallels can be seen between the mean and negative peak pressure coefficients of the panels' upper and lower surfaces. Thus, the panels' lower surfaces of the 1:50 array have experienced the lowest negative peak pressure coefficients and the higher values were experienced by panels of 1:200 array, but the opposite trend is shown on the back panel (H) for 120° to 180° wind direction. The upper surface peak pressure coefficients have shown a large discrepancy of decreasing tendency with enlarging the test model for wind direction ranging from 0° to 90°, and less discrepancy of increasing tendency with relaxing the geometric scale is noticed for 105°-180° wind directions excluding, however, the negative peak pressure coefficients of the front panel (panel-A) which are increased with enlarging the test model size for the considered wind directions.

The distribution of the surface peak pressure coefficients observed among the considered scales has served to confirm the observations and scenario made previously through the mean pressure coefficients on the impact of relaxing the geometric scale. For instance, the larger negative peak pressure coefficients observed on the upper surface of the middle module of the upstream panel (A) for 0° wind direction is (GC_P = -2.0) at the larger array, compared to GC_P = -1.7 at the scales of 1:100 and 1:200. The trend has been reversed at the downstream panels (Panel B and ones beyond); considering the middle panel (Panel E), the upper surface negative peak force coefficients among the considered scales 1:200, 1:100, and 1:50 are -0.8, -0.6 and -0.5, respectively. Thus, the upper surface of the upstream panel has been affected by the flow

interaction with the building edge; while, the downstream panels, the flow is affected by the panel size.

5.2 Local Force Coefficients

It has been observed that enlarging the geometric scale of the test model has left an impact on the flow pattern that immersing the solar array, as it turned out from the distribution of the surface mean pressure coefficients among the considered scales, which greatly inflected the distribution of the negative peak pressure and slightly the positive peak pressure. Therefore, it is also important to directly examine the impact of relaxing the geometric scale on the local force coefficient as representative of pressure difference across the solar module (net pressure). In view of that, this section will examine the influence of enlarging the test model size on the mean, negative (upward net pressure) peak, and positive (downward net pressure) peak force coefficients.

5.2.1 Mean Force Coefficients

Figure 5.6 shows the variation of the mean force coefficient (C_F) for modules positioned in the middle of the panels with the wind direction. As can be seen, the module of the front panel (A) of the smallest array has experienced a positive pressure for a wind direction almost straight into the building edge (0°, 15°, and 30°); whereas, the panel of the larger arrays (1:100 and 1:50) have experienced negative wind pressure. For wind directions 30° and 45°, the entire array at the considered scales has experienced positive force coefficients. With further changing the wind direction (i.e., 60°, 75°, and 90°), the negative mean force coefficients have appeared on the modules of the downstream panels (E, F, G, H). For wind directions from 105° to 150°, the entire array at the considered scales was subjected to negative mean force coefficients. Similar observations were found at wind directions 165° and 180°, but the windward panels (G and H) of
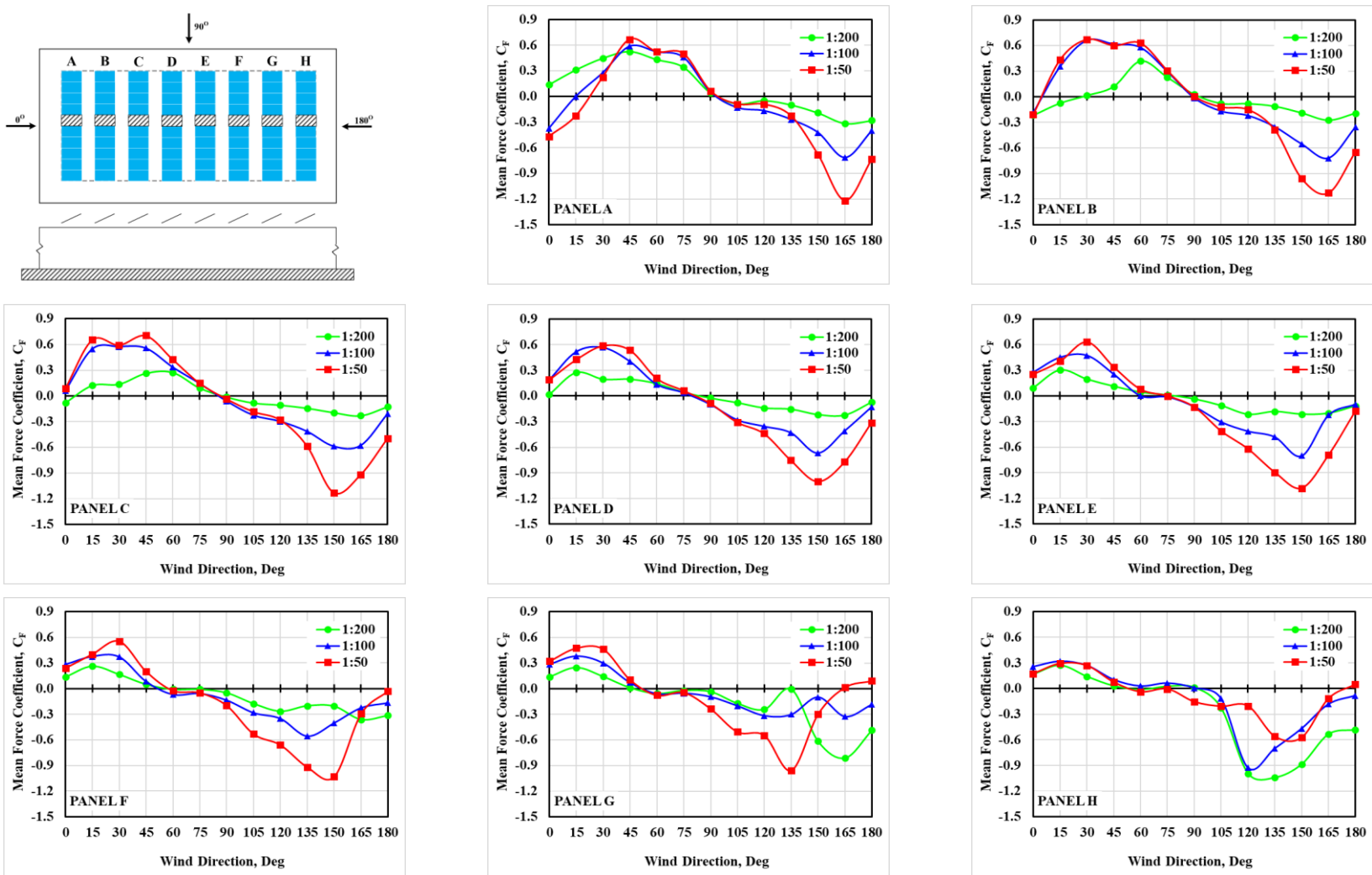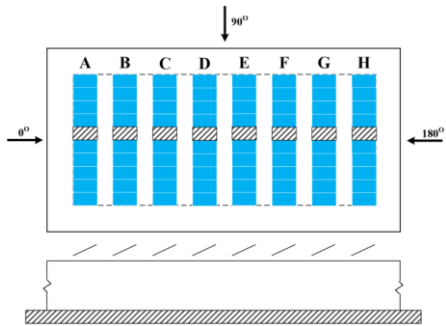
Figure 5.6 Variation of mean force coefficient (C_F) of PV modules located at the middle of the array (marked with ▨) versus wind direction

74

the 1:50 array have experienced positive mean force coefficients.

Clearly, this is associated with the distribution of the surface pressure. Recalling that both panel surfaces have exposed suction pressure with higher severity on the lower surface for wind directions between 0° and 90°, and lower severity at 105° -180° wind directions – refer to Figure 5.1. Thus, the lower surface suction has outstripped the upper surface suction for 105°-180° wind directions, hence the resulted net pressure will be in the same direction (i.e., positive net pressure tends to pull the module towards the roof). The opposite is the case regarding the negative net pressure for wind directions ranging from 105° to 180°, where the upper surface suction has outstripped.

Concerning the impact of relaxing the geometric scale, the observed mean force coefficients are generally increased with enlarging the geometric test scaling for most panels and wind directions. The mean force coefficients induced at larger scales (1:100 and 1:50) show discrepancies with the corresponding results of the 1:200 array in order of 1.5-2.0 and 1.5-3.5, respectively. Whereas, the results of the 1:100 and 1:50 arrays show better agreement, which is most likely in the order of 1.0-1.5.

5.2.2 Peak Force Coefficients

Figure 5.7 shows the variation of the negative and positive peak force coefficients of PV modules located at the middle of the array with the wind direction. As shown, the negative peak force coefficients show higher discrepancy compared to the positive peak pressure coefficients with the geometric scale, particularly at critical wind direction range from 120°-180°.

As shown in Figure 5.7, all panels of the array scaled at 1:200 have experienced negative peak force coefficients at all wind directions. Nevertheless, some panels of larger arrays have not

experienced negative peak force coefficients, such as the leeward panels (E, F, G, and H) for 0°

and 15° winds and some middle panels for 30° to 60° winds. Thus, there is inconsistency in the

spatial distribution pattern of the negative peak force coefficients among the considered scales for

wind directions between 0° and 75°. Therefore, the assessment of the negative peak force

coefficients variability among the considered scales are restricted to those from wind directions

ranging from 75° to 180°.

As shown, the negative peak force coefficients obtained at 1:100 and 1:50 arrays have generally

approached slight levels of concordance (i.e., within a factor of 1.3) with the corresponding results

obtained by the 1:200 array for wind directions 75°, 90°, and 105°. For winds from 120° to 180°,

the results on the upstream panels (A, B, C, D, and E) increase in magnitude with increasing the

geometric test scaling but the exact opposite pattern is noted for the downstream panels (E, G, and

H). In general, the negative peak force coefficients obtained by 1:100 and 1:50 arrays are barely

below the level of acceptable concordance with the results of the 1:200 array, showing an

escalation factor ranging from 1.4 to 3.0 for the modules of the panels A to E and a reduction factor

up to 3.0 on the modules of the panels F to H. On the other hand, the results of the 1:50 array for

these wind directions attain a slight concordance with a factor of about 1.3 to the results of the

1:100 array.

With regard to the positive peak force coefficients, all panels of the array at the considered

scales have experienced positive peak net pressure for wind direction ranging from 0° to 105° -

see Figure 5.7. The positive peak force coefficients generally increase with increasing the

geometric test scaling – except the modules of the front panel (A), where the positive peak force

coefficients of 1:100 and 1:50 panels are less than the coefficients of 1:200 panel.

Generally, the positive peak force coefficients obtained on the 1:100 array approach a slight
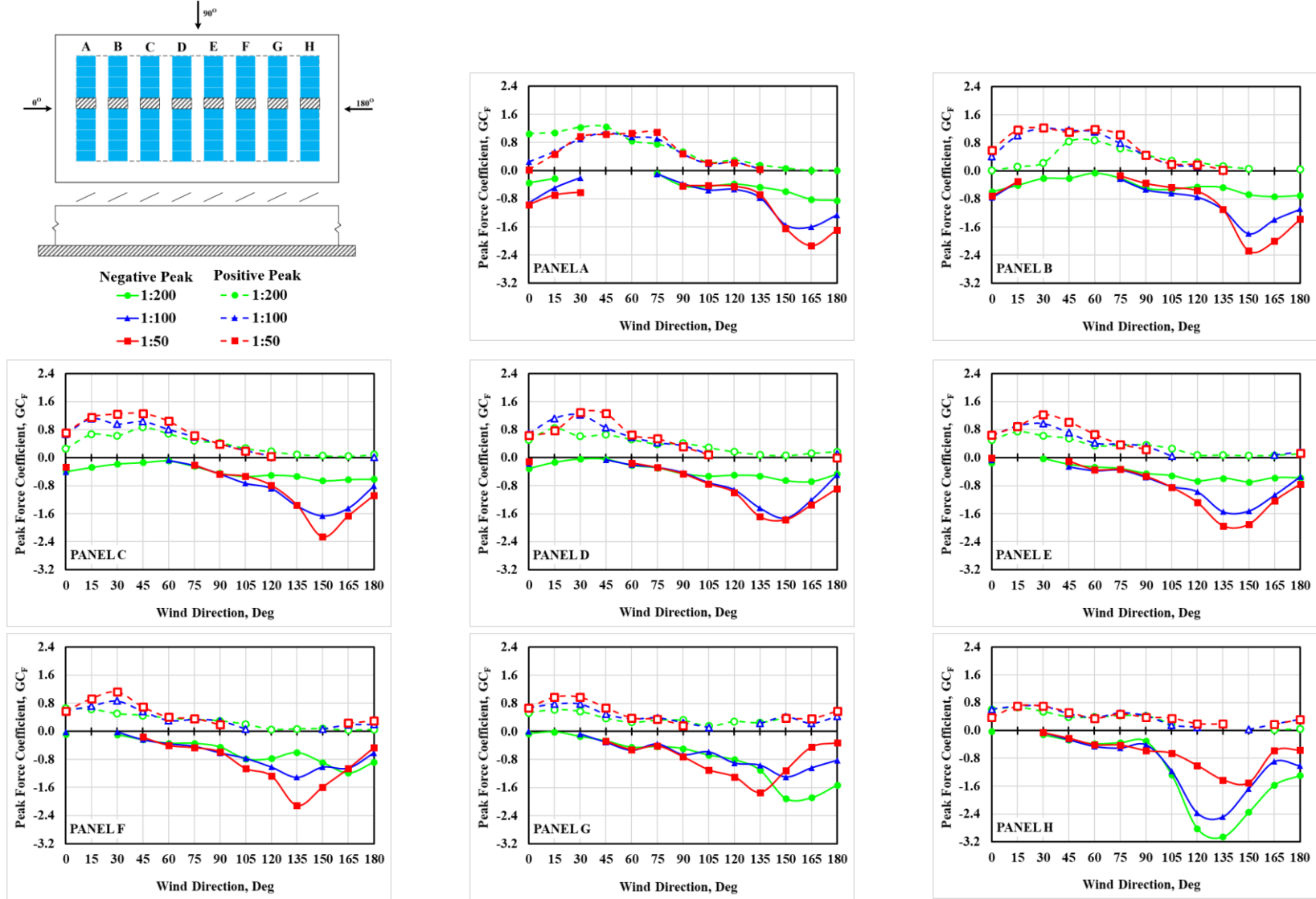
Figure 5.7 Variation of positive and negative peak force coefficient (GC_F) of PV modules located at the middle of the array (marked with ▨) versus wind direction

concordance with a 1.6 factor compared with the results of the 1:50 array. Also, the positive peak force coefficients of the 1:100 array show significant concordance with the results obtained on the 1:200 array; on the other hand, the results of the larger array show less concordance with the results of 1:200 array – roughly greater by a factor ranging between 1.1 and 2.0.

5.3 Design Force Coefficients

In this section, the results obtained on the arrays at tilt angles ω = 15°, 25°, and 35° will be explored to discuss the impact of enlarging the geometric scale of the test models on the force coefficients deemed to be relevant in the design, including the positive and negative peak force coefficients.

It is understandable that the surface pressures at oblique wind directions, including the upper surface pressure developed at winds blowing from behind (i.e., between 105° and 165°) and the lower surface pressure developed at the wind blowing from front (i.e., between 15° and 75°), are the most severe; and hence, the unfavorable wind directions for upward (negative) and downward (positive) force coefficients are 15° - 45° and 135° - 165°, respectively.

Appendix B provides the local distribution of extreme positive and negative mean and peak force coefficients (envelope values from the accounted wind directions) in conjunction with the corresponding most critical wind direction for the solar array with a tilt angle $\omega = 15°$ at the considered scales. As illustrated, the most critical wind direction for the extreme values of the force coefficients shows great similarity among the considered scales, where the extreme values for the positive and negative peak force coefficients are developed at wind directions of 15° - 45° and 135° - 165°, respectively. Therefore, the positive and negative peak force coefficients developed at these wind directions can be regarded as the design force coefficients.

For the considered geometric test scales, Figures 5.8-5.10 show the local distribution of the positive peak force coefficients obtained at wind directions of 15°, 30°, and 45°; whereas Figures 5.11-5.13 show the local distribution of the negative peak force coefficients obtained at wind directions of 135°, 150°, and 165°.

As shown in Figures 5.8-5.10, the windward edge modules and the modules of the upstream panels (A and B) have experienced the highest positive peak net pressures among the considered scales and wind directions. The negative peak force coefficients followed a similar trend, but it is observed that the interior modules of the middle and leeward panels of the larger arrays (scaled at 1:100 and 1:50) have experienced the highest downward net pressures compared with the upstream and edge modules, as illustrated in Figures 5.11-5.13.

The distribution of the results provided in Figures 5.8-5.13 indicates that the local positive and the local negative peak force coefficients vary depending on the geometric test scaling. However, the variations with relaxing the geometric test scaling are random in nature according to the solar module location within the array, the tendency of the results with enlarging the size of the model can be qualitatively summarized as follows:

- Decreasing tendency of the positive peak force coefficients of the modules of the upstream panel (A) and on the windward edge. The peak force coefficients of the upstream panel at 1:100 and 1:50 scales are found to be in the range of 0.3-0.7 and 0.1-0.6 times the results obtained on the corresponding panel scaled at 1:200. The peak force coefficients of the windward edge modules revealed a slight concordance within a factor of 1.4 among the considered scales. The highest variations are observed at wind direction of 15° and on the array at a tilt angle of 25°.

- Increasing tendency of the positive peak force coefficients of the modules in the middle and
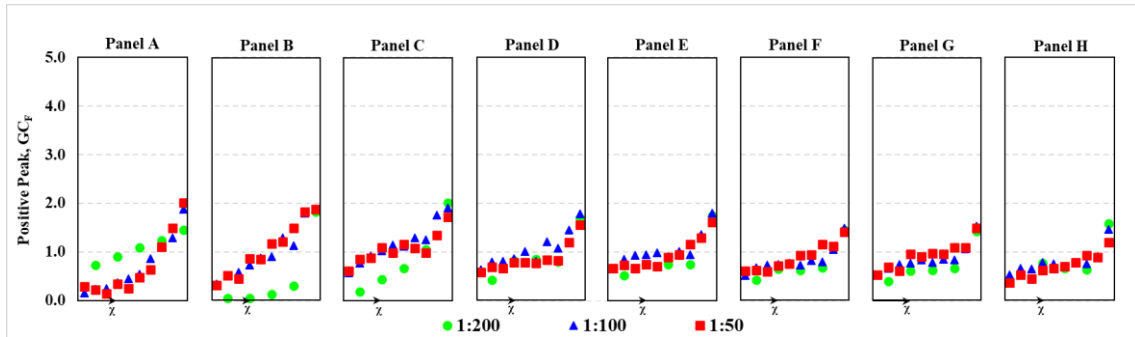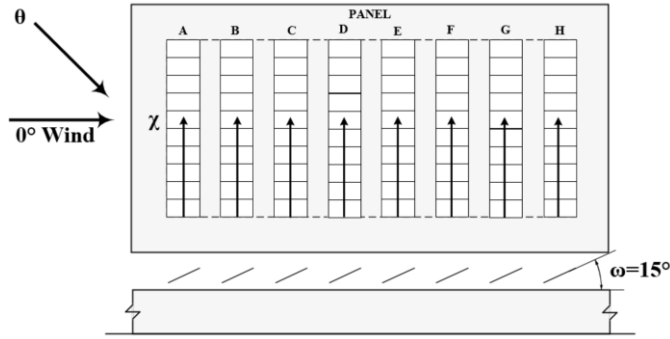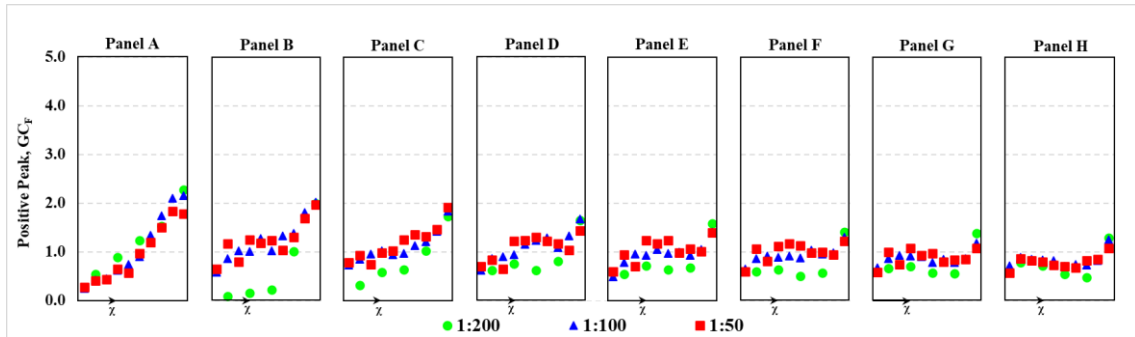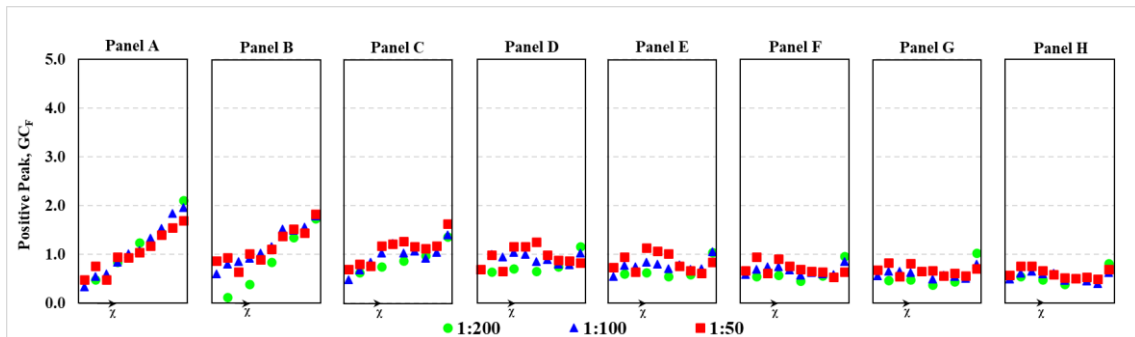
Figure 5.8 Positive peak force coefficients of solar array at inclination ω = 15° for wind direction, θ, of: (a) 15°, (b) 30°, and (c) 45°
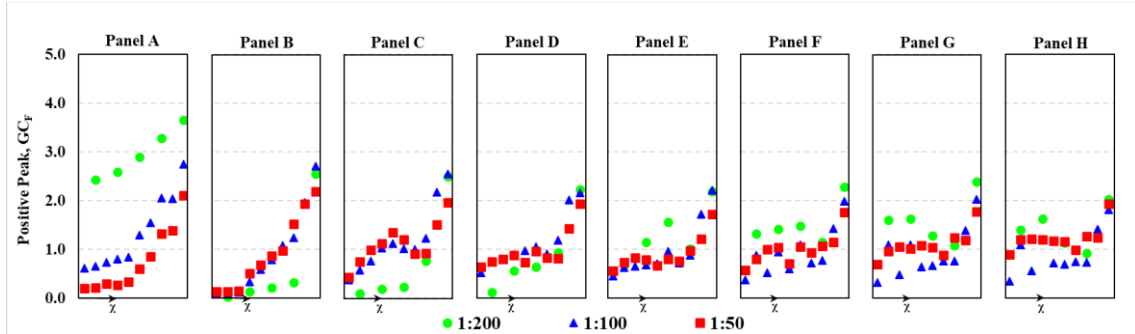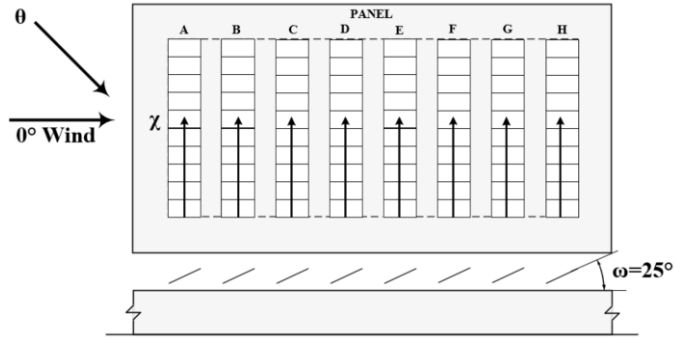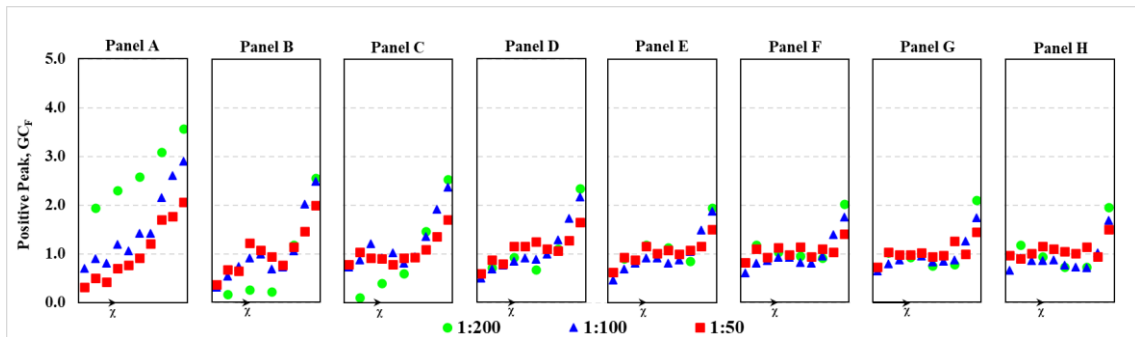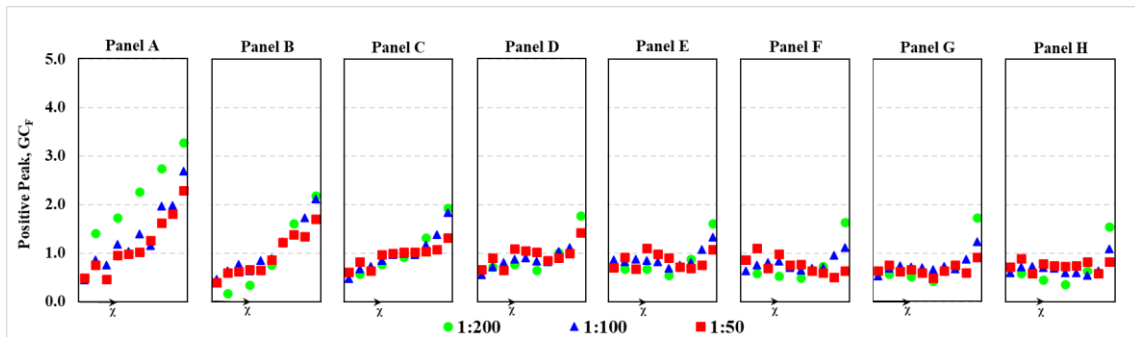
Figure 5.9 Positive peak force coefficients of solar array at inclination ω = 25° for wind direction, θ, of: (a) 15°, (b) 30°, and (c) 45°
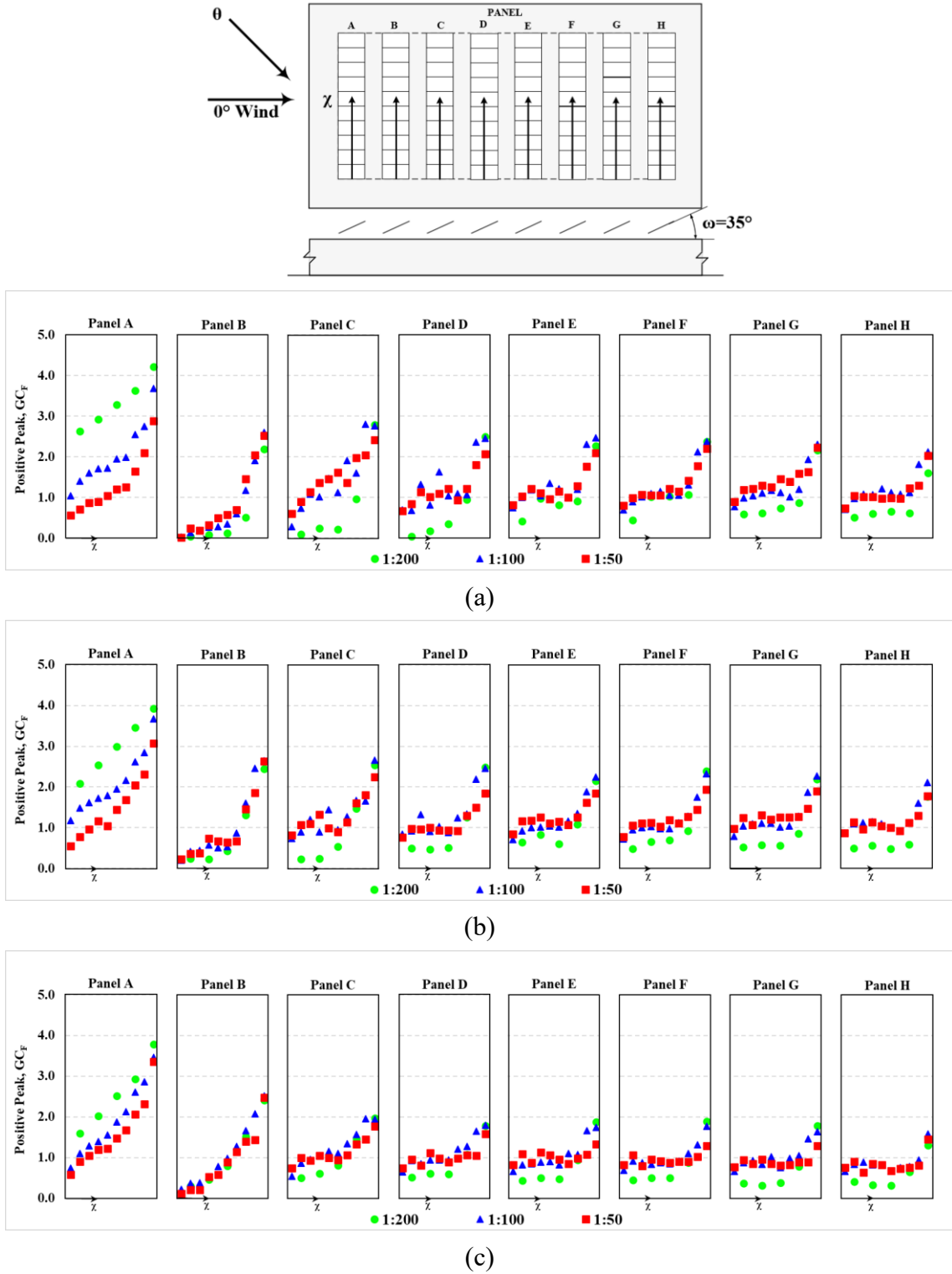
Figure 5.10 Positive peak force coefficients of solar array at inclination ω = 35° for wind direction, θ, of: (a) 15°, (b) 30°, and (c) 45°
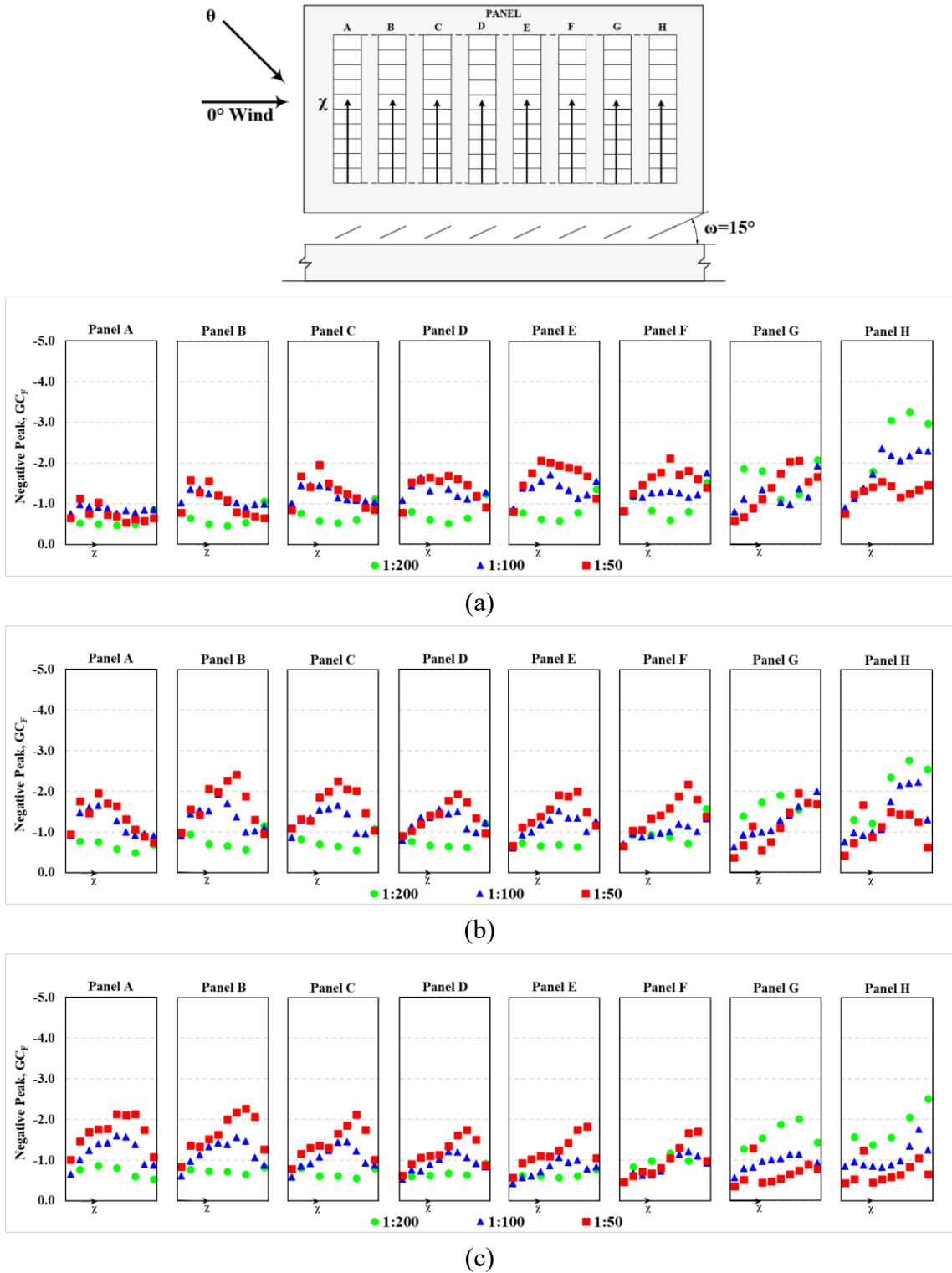
Figure 5.11 Negative peak force coefficients of solar array at inclination ω = 15° for wind direction, θ, of: (a) 135°, (b) 150°, and (c) 165°
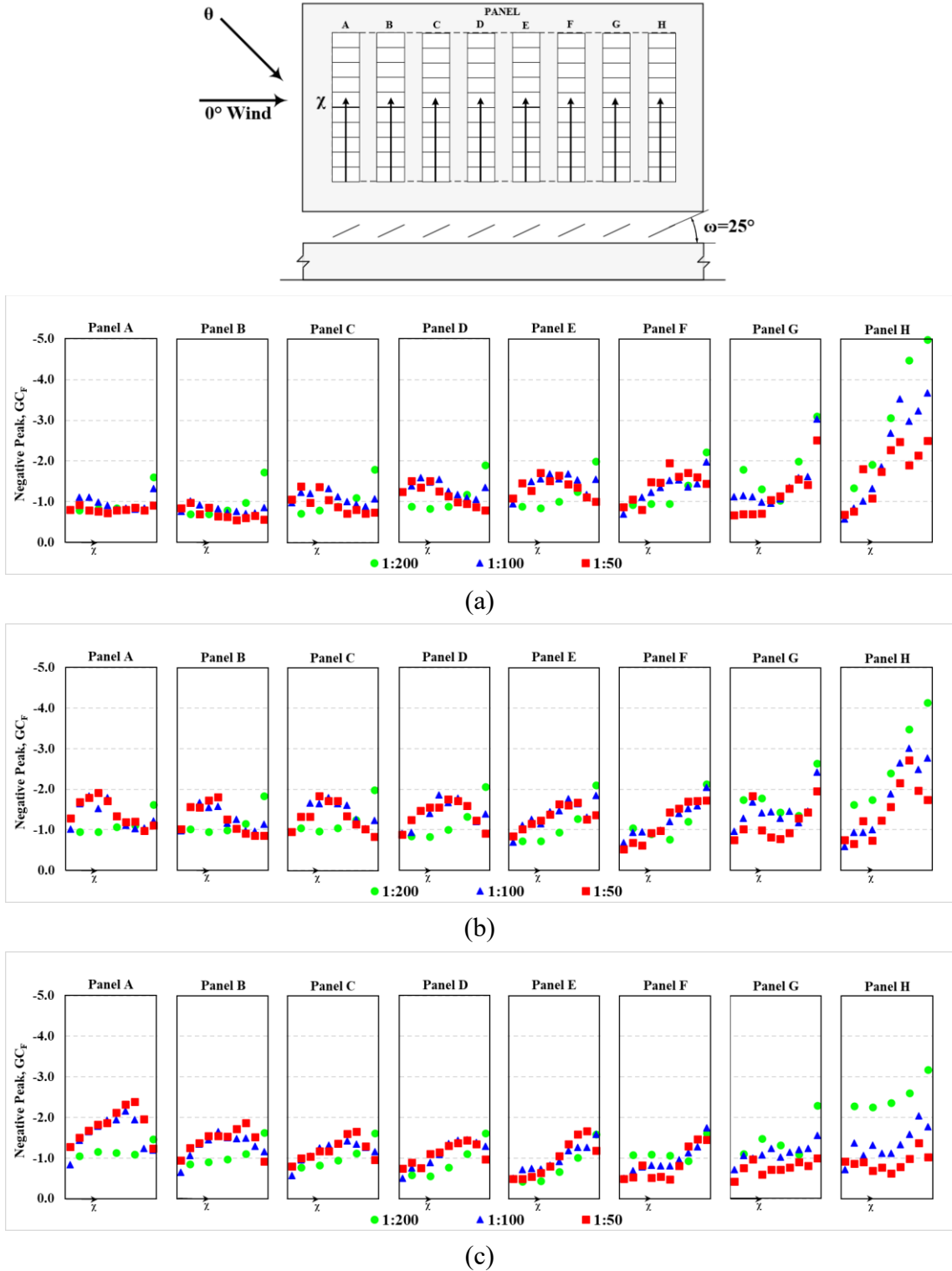
Figure 5.12 Negative peak force coefficients of solar array at inclination ω = 25° for wind

direction, θ, of: (a) 135°, (b) 150°, and (c) 165°
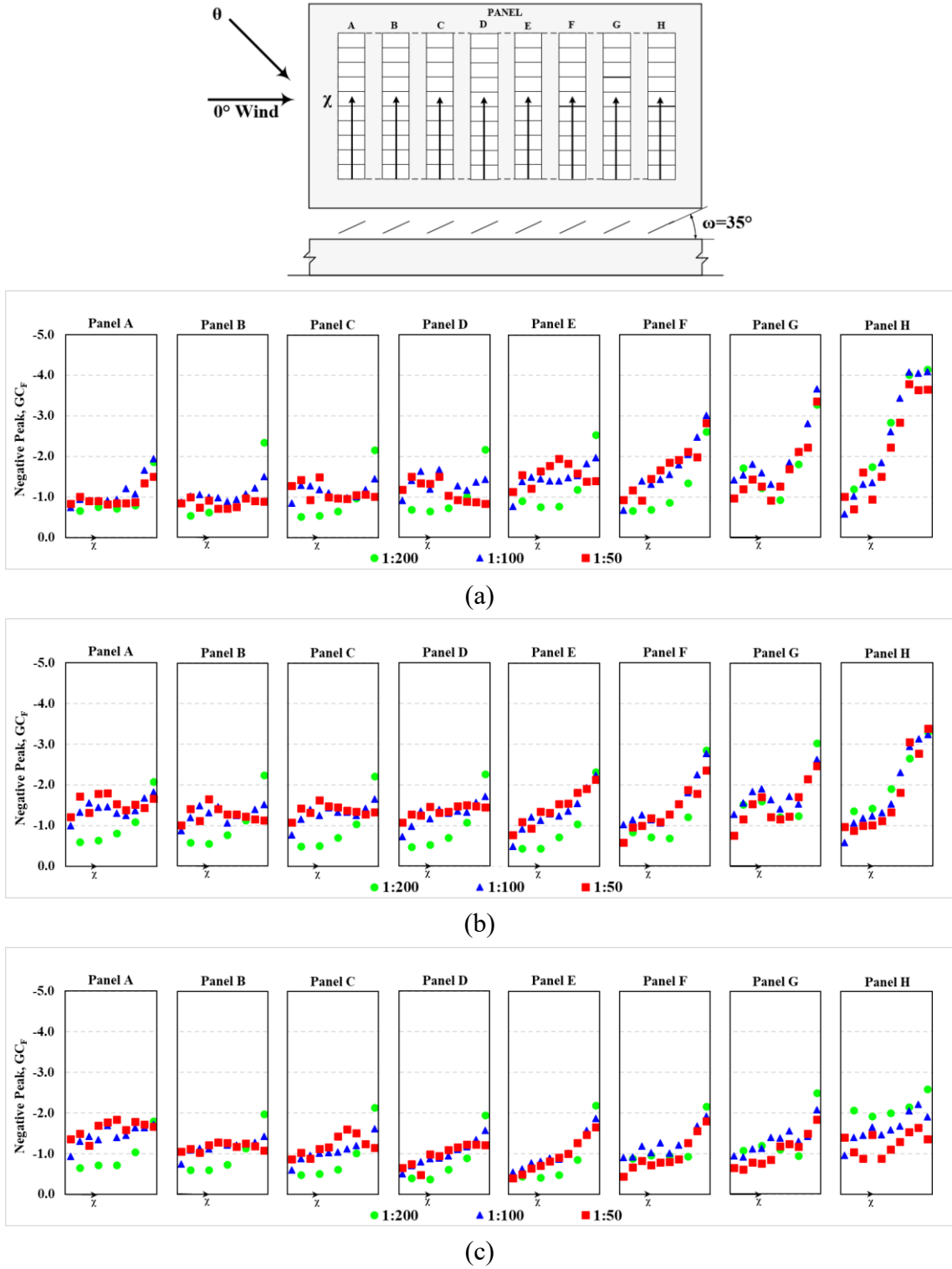
Figure 5.13 Negative peak force coefficients of solar array at inclination ω = 35° for wind direction, θ, of: (a) 135°, (b) 150°, and (c) 165°

the leeward edge of the array. The variation is nearly constant with the wind direction and array tilt angle.

- Decreasing tendency of the negative peak force coefficients of modules of the upstream panels (Panel G and H) and on the windward edge modules. The force coefficients of modules of 1:100 and 1:50 arrays were respectively found to be in a factor of 0.5-0.8 and 0.3-0.7 compared with the results of the corresponding modules of the 1:200 array. The highest variations are observed at wind direction of 165° and the lowest variations have been observed at the array of higher tilt angle (i.e., 35°).

- Increasing tendency of the negative peak force coefficients of the interior and leeward edge modules, in which the modules of the large arrays (1:100 and 1:50) have experienced negative wind pressure almost twice and higher than the results of 1:200 array. The variation is quasi constant with the wind direction and the tilt angle.

Such tendencies on the positive peak force coefficients at critical wind directions are attributed mainly to the influence of relaxing the geometric test scaling on the suction developed on the upper surface, in that enlarging the model size resulted in alleviating the severity of the suction on the upper surface of modules located in the middle and in the leeward edge of the array and heightening the severity of the suction on the upper surface of the modules in the windward edge. The tendencies of the negative peak force coefficients at critical wind directions against the testing model scale are attributed to the impact of relaxing the geometric test scaling on wind-induced pressure on the panel surfaces. As discussed formerly, enlarging the model size has increased the severity of upper surface suction of the upstream panels (G and H) and has decreased the severity of the lower surface suction of modules located in the middle and leeward edge of the array.

CHAPTER 6 EFFECT OF AIR CLEARANCE BENEATH THE SOLAR ARRAY

In this chapter, the impact of the air clearance size between the solar array and the roof will be examined on the solar array tilted at angle $\omega = 15°$. The mean and peak pressure coefficients (surface pressures) and mean and peak force coefficients (net pressures) are examined for three clearance heights, namely $G = 0$, 0.20, and 0.40 m (in full-scale) – refer to Table 4.1. The experimental force coefficients that could be treated as design loading will be examined and compared in the condition of changing the underneath array clearance.

A portion of the work presented in this chapter has been published in the Journal of Structural Engineering (Alrawashdeh and Stathopoulos, 2022b) and presented at several conferences (Alrawashdeh and Stathopoulos, 2022a, 2022c).

6.1 Mean Pressure Coefficients and Force Coefficients

Investigation of the wind pressure induced on the upper and lower surfaces of the panels shows that the panel surfaces are dominated by negative pressure (suction) for all wind directions. Figures 6.1 and 6.2 provide the maximum negative mean pressure coefficients over the panel's lower and upper surface (in an absolute sense) for each wind direction, respectively. Thus, the values provided in these figures are the worst local mean suction induced on the panel surfaces at each particular wind direction. As illustrated, the lower surface mean suctions within the individual array clearance are generally of higher severity than the corresponding values of the upper surface for wind directions from 15° to 45°. Conversely, the opposite trend for a certain clearance height is observed with respect to the distribution of the surface suctions at wind direction between 135° and 165°. The presence of vortices detached from the leading edges of the roof at oblique wind
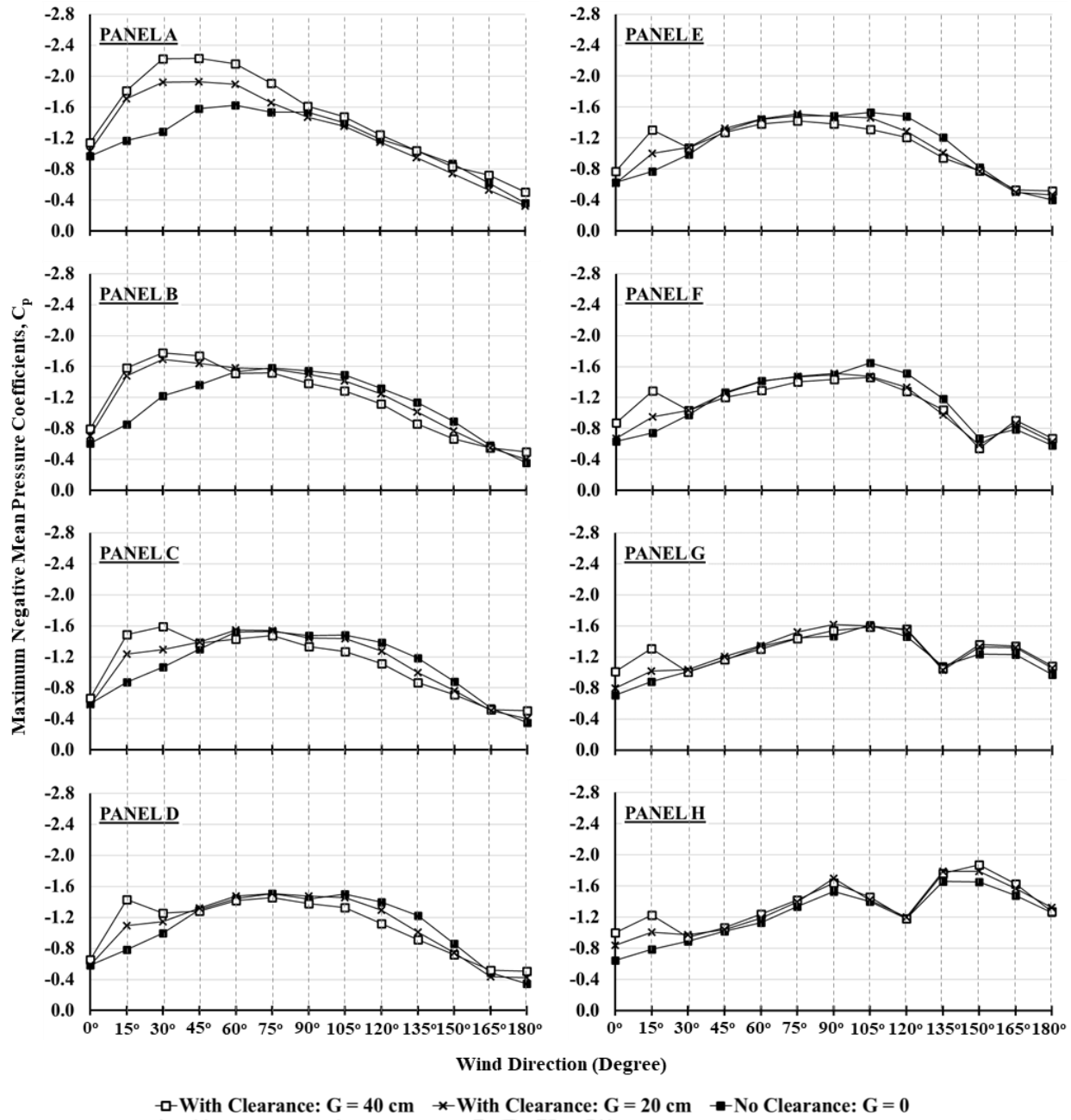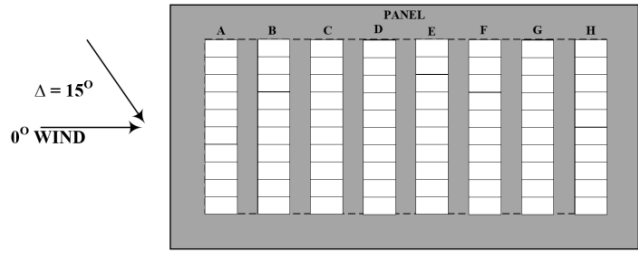
Figure 6.1 Maximum local negative mean pressure coefficients over the panel lower surface for

each wind direction
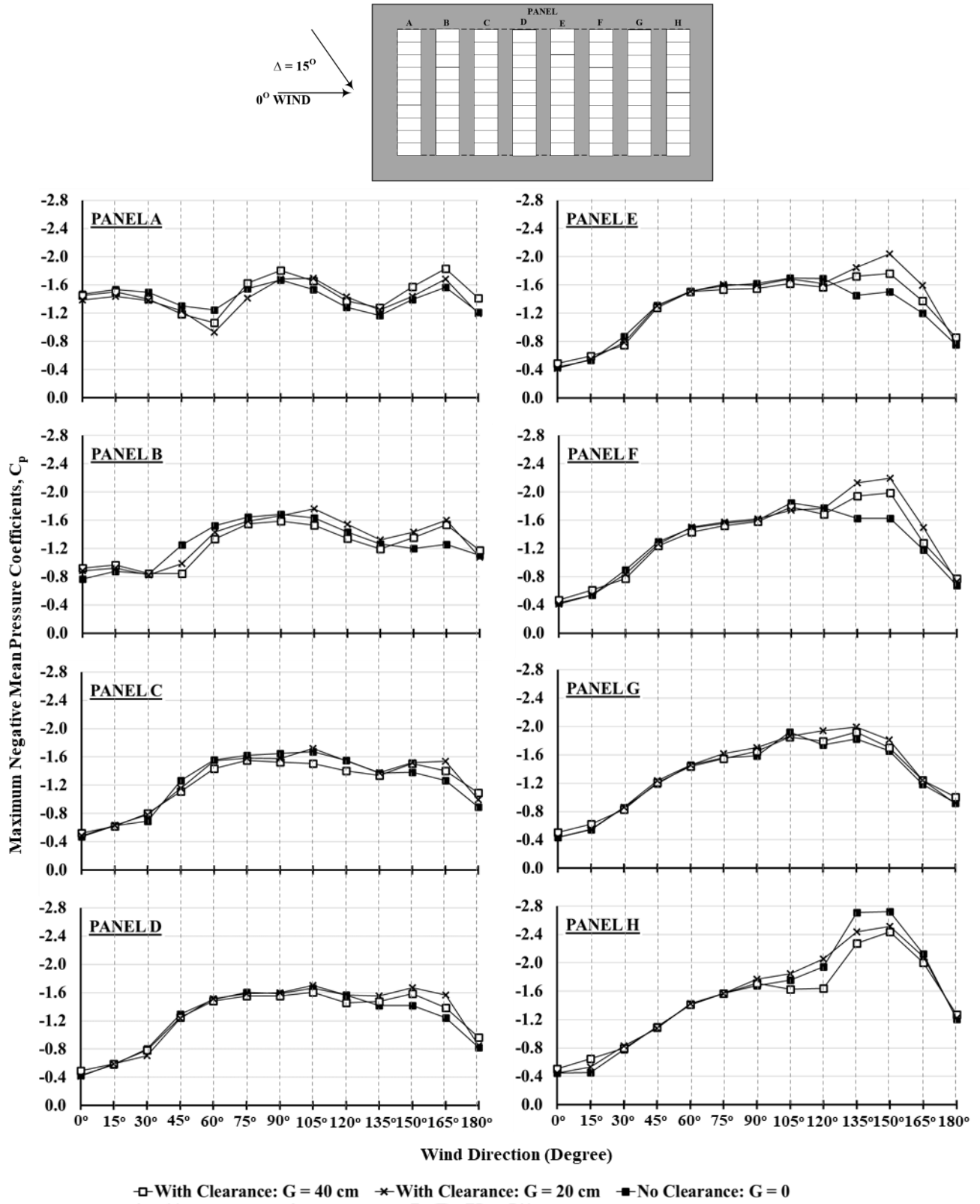
Figure 6.2 Maximum local negative mean pressure coefficients over the panel upper surface for

each wind direction

directions have surely played a significant role in influencing the distribution of the surface pressure (Banks, 2013; and Wang et al., 2020b). The wind suctions induced on the surfaces have further escalated and spread to a larger region over the array's panels mainly due to the separation of the conical vortices which has a downflow nature at the higher edge of the panels. The interaction among these conical vortices and solar panels has yielded localized phenomena, such as wake regions and stagnation points beneath the solar panels at wind directions from 15° to 45° and separation bubbles above the panels at wind directions from 135° to 165°, which are influential in impacting the surface pressures with the wind direction.

In line with the previous study of Wang et al. (2020b), the effect of the array clearance on the lower surface mean pressure coefficients is more pronounced than those of the upper surface. As shown in Figure 6.1, the maximum mean pressure coefficients on the lower surface have greatly decreased in value with decreasing the clearance above the roof, particularly marked at wind directions from 15° to 75° for the front panel A and from 0° to 30° for the other panels of the array. A likely scenario would suggest that disturbance of the wake region formulation on the lower surface for winds blowing from front (i.e., 0° - 30°) might have accounted for the decrease in the mean suction of the lower surface with decreasing the size of the array clearance. In this regard, the distribution of the local mean surface pressure and force coefficients will be examined at particular wind directions, including 0°, 45°, 135°, and 180°.

Figure 6.3 provides the local distribution of the mean wind pressure coefficients on the lower and upper surface and the mean force coefficients for modules located at the side edge of the array for wind directions of 0° and 180°. As shown in Figure 6.3 (a), placing the array at a smaller clearance ($G = 20$ cm) or directly on the roof ($G = 0$ cm) has reduced the positive mean force coefficients (downward net pressures) at 0° wind direction, greatly at regions close to the edges of
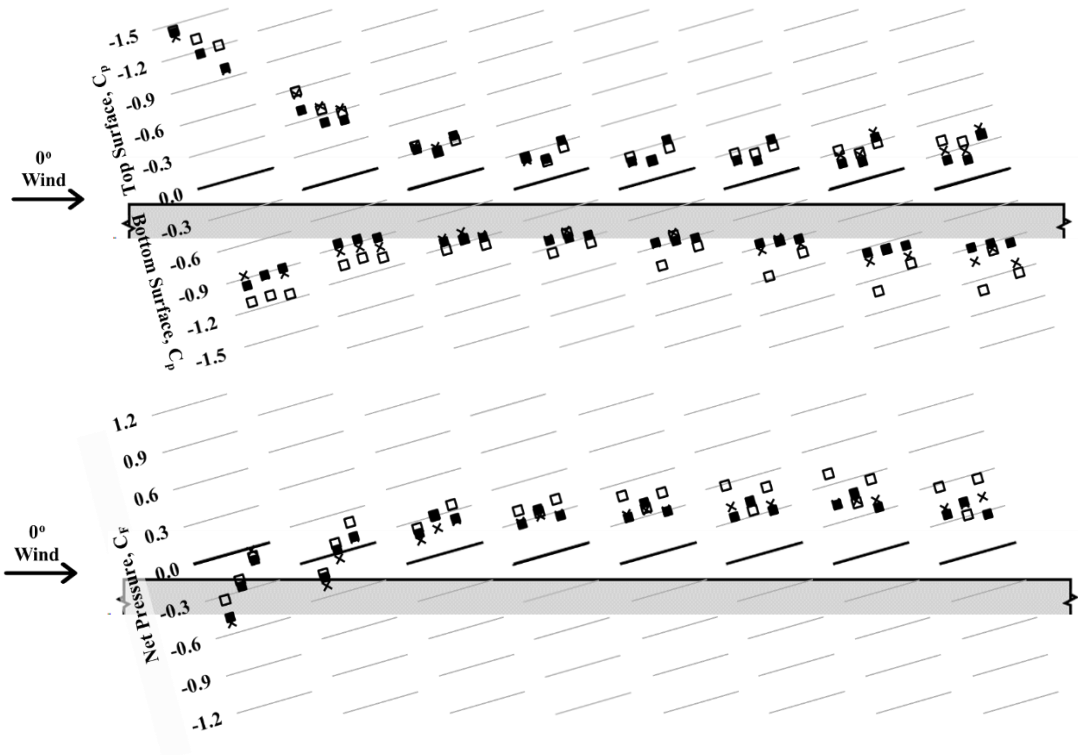
(a)
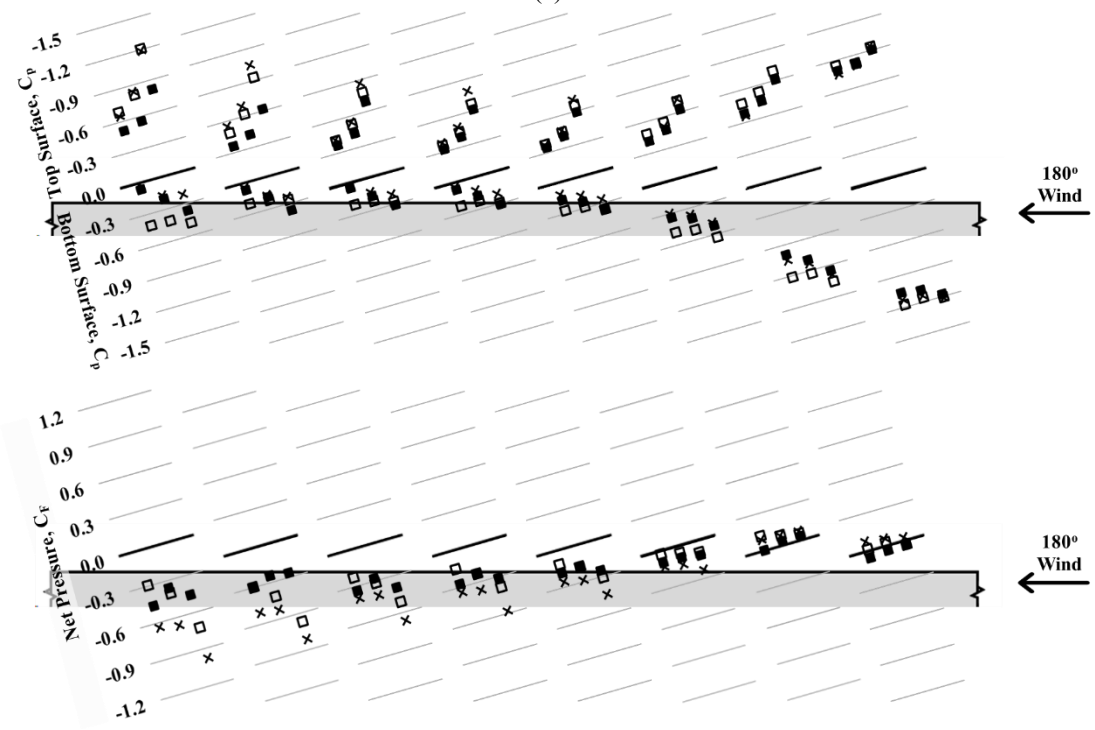
(b)

□ With Clearance: G = 40 cm   × With Clearance: G = 20 cm   ■ No Clearance: G = 0

Figure 6.3 Clearance effect on local mean pressure and force coefficients (C_P and C_F) at the

edge of the array (Module: M1) at wind direction: (a) 0°, and (b) 180°

the modules. This tendency comes as a result of the reduction in the mean pressure coefficients on the lower surface of the modules installed at clearance height $G = 0$ and $G = 20$ cm.

As shown in Figure 6.3 (b) for 180° wind direction, minimizing the array clearance, either to $G = 0$ or $G = 20$ cm, tends to decrease the negative mean pressure coefficients of the lower surface, particularly at regions close to the lower edge of the modules of the downstream panels. Regarding the upper surface, the negative pressure coefficients of the modules of the downstream panels at no clearance (panel A and B at $G = 0$) have only been affected. Therefore, the decrease in the array clearance to $G = 20$ cm and the concomitant decrease in the lower surface pressure have naturally led to increasing the negative mean force coefficients (higher upward net pressures).

Figure 6.4 shows the local distribution of the surface mean pressure and mean force coefficients of modules located at the side of the array (M1) at 45° and 135° wind directions. As clearly shown, the suctions on the upper surface seem to have been slightly affected by the air clearance. The mean pressure coefficients of the lower surface of the upstream panels (A at 45° wind and H at 135° wind) are significantly reduced at no clearance ($G = 0$) – see the upper charts of Figure 6.4 (a) and (b). As reported by the CFD study of Wang et al. (2020a), these modules are mostly far from the building edge conical vortices. On the other hand, an inverse correlation between the clearance height and the lower surface mean pressure coefficients of the downstream panels (G, F, E, D, C, and B) at 135° wind direction, such that the highest suctions are induced when the array is placed at no clearance ($G = 0$).

Consequently, the positive mean force coefficient of modules less interfered by the conical vortices, namely windward modules of the solar panels A, B, and C at 45° wind direction, are decreased when placing the panels at no clearance, largely at regions close to the lower edge of the panels, as shown in Figure 6.4 (a). Otherwise, the positive mean force coefficients do not
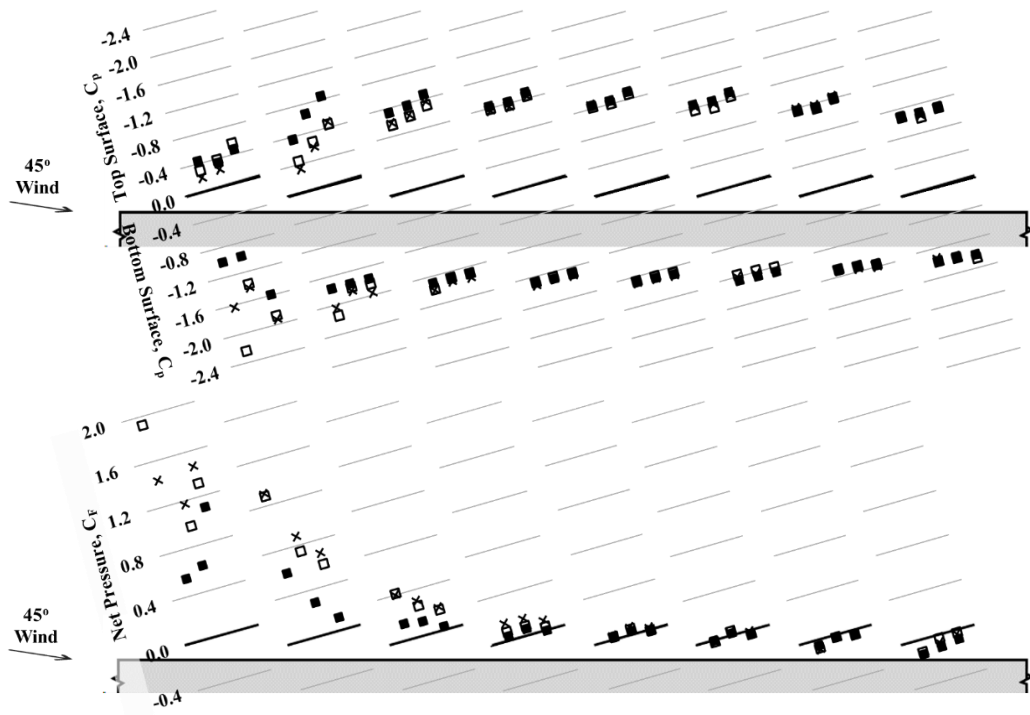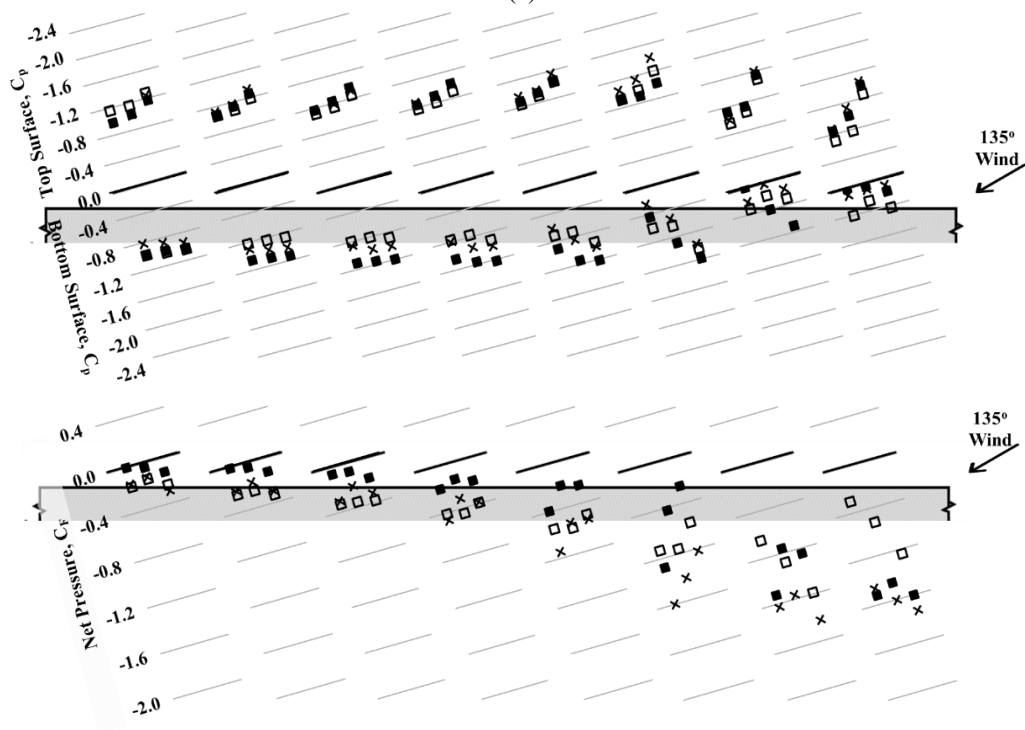
Figure 6.4 Local mean pressure and force coefficients (C_P and C_F) at the windward edge of the array (Module: M1) at wind direction: (a) 45° and (b) 135°

necessarily depend on the underneath array clearance. Furthermore, the negative mean force coefficients of the downstream modules (G to A) are greatly decreased at no clearance ($G = 0$), significantly at the regions close to the higher edge of the panels, as shown in Figure 6.4 (b).

The effects of the air clearance on the wind suction induced on the lower surface of the solar modules are indeed associated with wind interference of the solar panels. Thus, the size of the air clearance affects the impact of the wind interference of the solar panels. As clearly shown from the mean pressure distribution on the lower surface of all panels at 0° wind and the upstream panels at 45° wind, placing the array at lower clearance would enhance wind interference of the solar panels and disturb the flow separation at the higher edge of the panels. This results in a wake region formulation of a lower vortex frequency.

The same applies to the distribution of the mean pressure coefficients on the lower surface at winds blowing from behind (i.e., all panels at straight wind and upstream panel for oblique winds such as 180° and 135°, respectively). Placing the array at no clearance would confine the airflow underneath the lower surface of the panels, and hence, this will further disturb the wake region formulation. Regarding the downstream panels at oblique wind direction, the shear layer of the confined wake region is enhanced by the shear layer of the upper surface of the upstream panel inducing higher suction on the lower surface. On the other hand, when there is enough clearance underneath the panels the flow will reattach on the roof and penetrate with less interference with the wake region on the lower surface of the upstream panel.

Finally, another point that should be stressed is the highly elevated negative mean force coefficients observed at reducing the array clearance to $G = 20$ cm - see for instance chart (b) of Figures 6.3 and 6.4. This is indeed a result of the increased suction on the upper surface at wind directions from 135° to 180° (see Figure 6.1), which enhances the net pressure to act upwards.

Thus, the array at lower clearance would augment the wind interference of the solar panels, causing further attenuation in the wake region on the lower surface and further intensifying the vortices on the upper surface shed from the higher edge of the panels.

6.2 Peak Pressure Coefficients and Force Coefficients

Previously, it has been demonstrated through the distribution of the mean surface pressure and the mean force coefficients that the solar array clearance above the roof led to alter the conditions of the flow around panels of the solar array. Therefore, it is important to further assess the impact of underneath array clearance on the peak pressures on the surfaces and across the panels represented by the peak pressure and force coefficients, respectively.

Figures 6.5 and 6.6 show the maximum local positive and negative peak pressure coefficients on the lower and upper surface for each wind direction, respectively. As illustrated, the surfaces (upper and lower) of the panels have been, however, dominantly exposed to peak suction pressure at different clearance conditions underneath the solar array, changing the clearance has resulted in disturbing their severity. A trend is clearly demonstrated on the lower surface for the most critical wind directions, including the front panel A at 15° - 75° winds, middle panels for 15° - 30°, and back panels for 0° - 30° winds. Conversely, with reference to Figure 6.6, the maximum negative pressure coefficients of the upper surface are relatively unaffected by the clearance height, except for some panels in the middle of the array (e.g., E and F) at the most critical wind directions ranging from 120° to 165°.

In detail, it has been noticed that the negative peak pressure coefficients on the lower and upper surfaces are significantly decreased when the array is placed at no clearance ($G = 0$). Also,
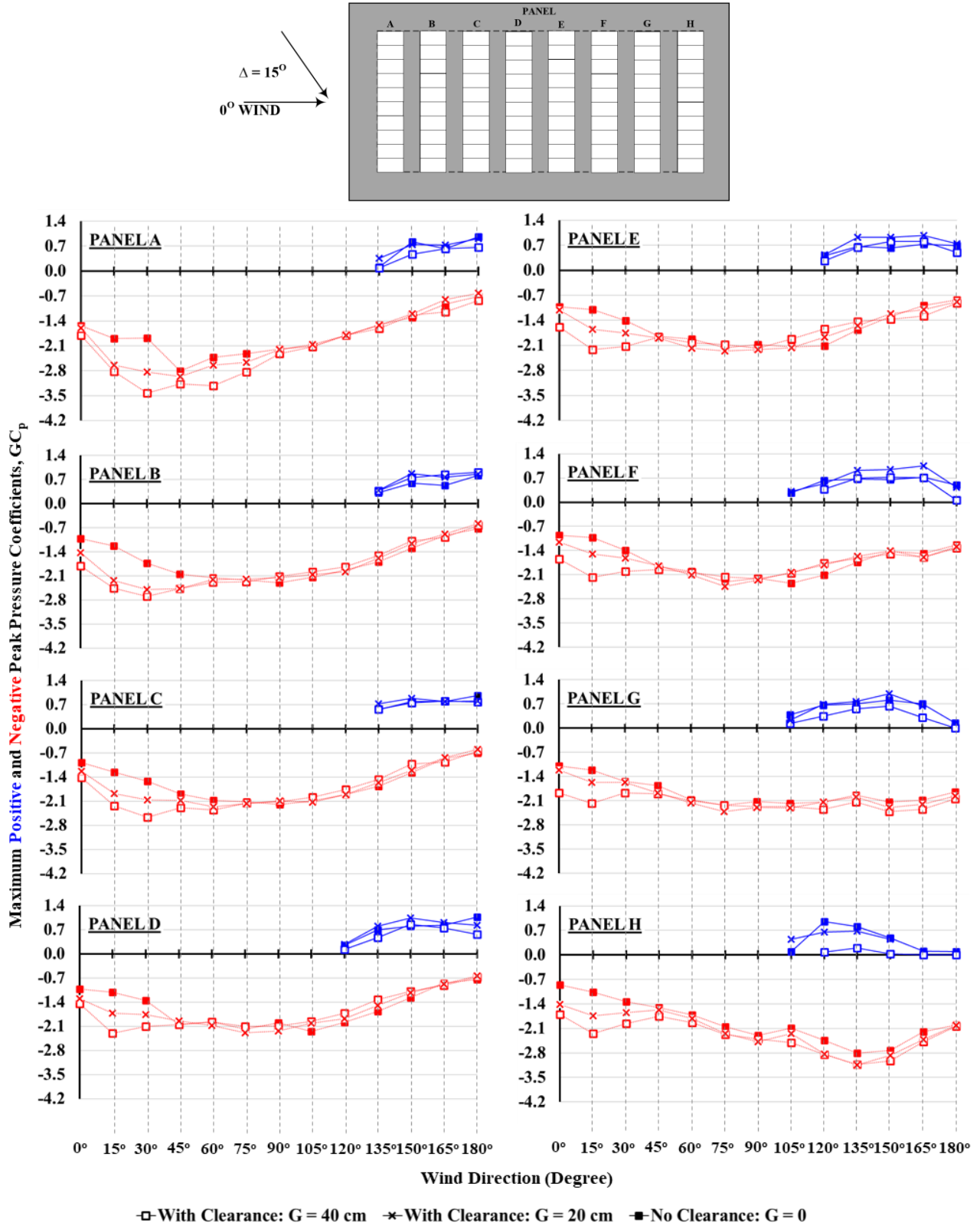
Figure 6.5 Maximum local positive and negative peak pressure coefficients of the panel lower

surface at each wind direction

96
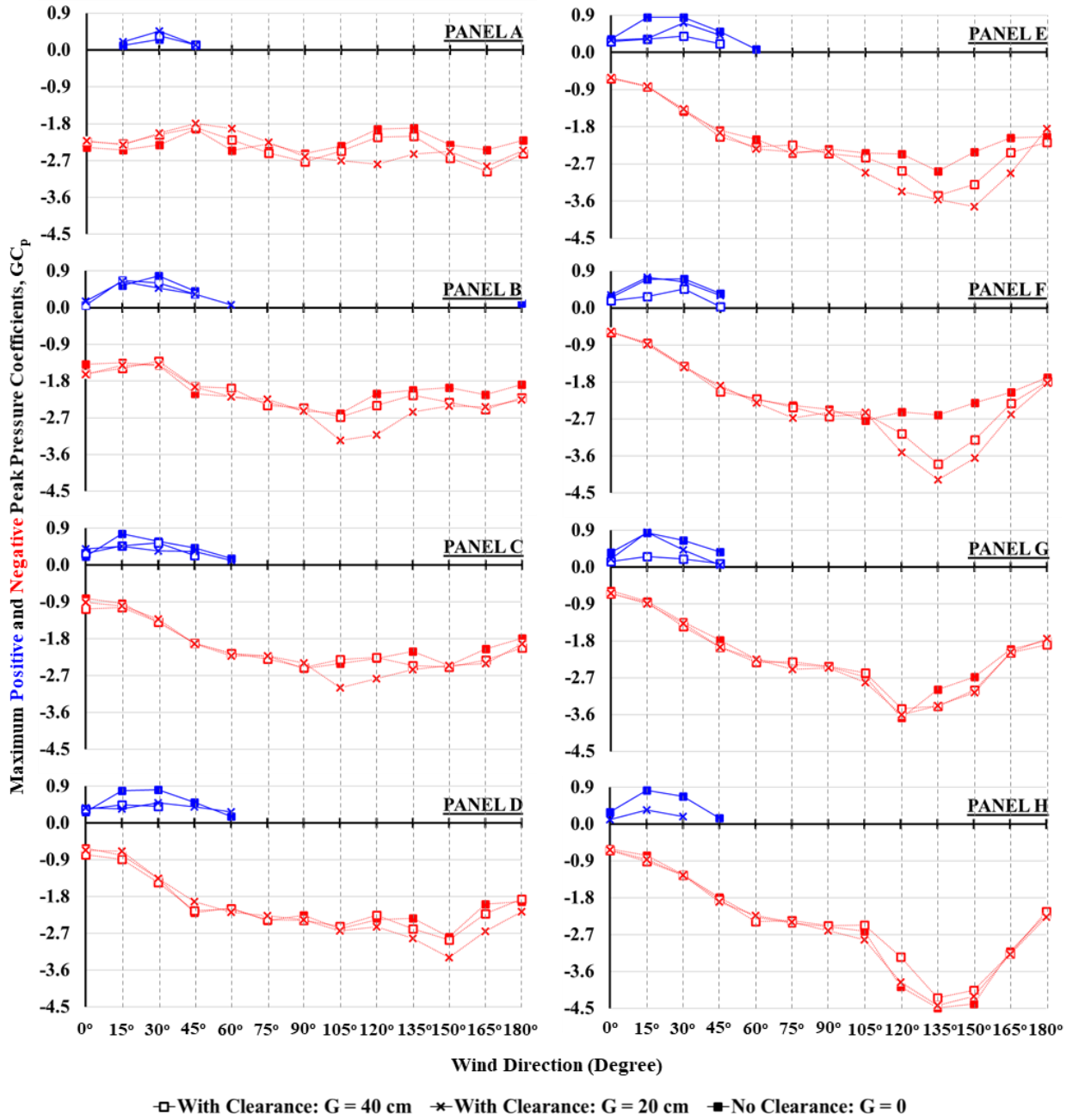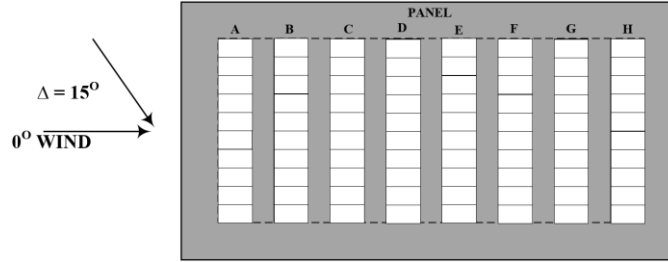
Figure 6.6 Maximum local positive and negative peak pressure coefficients of the panel upper

surface at each wind direction

97

the size of the clearance (G = 20 cm and G = 40 cm) has two countervailing effects on the surface negative peak pressure coefficients. On one hand, the negative peak pressure coefficients on the lower surface are increased with increasing the solar array clearance, and on the other hand, the negative peak pressure coefficients of the upper surface are decreased in magnitude with increasing the solar array clearance - as shown in Figures 6.5 and 6.6, respectively.

The impact of the underneath solar panel array clearance will be examined on the local negative and positive peak force coefficients obtained at wind directions 30° and 150° for modules located on the windward edge of the array.

Figure 6.7 shows clearly that at the most critical wind direction for positive peak net pressure, i.e. 30°, the values of the positive peak force coefficients (GC_F) have decreased, particularly at no clearance (G = 0). This is due to the increased lower surface wind pressure coefficients which played a significant role in more equalizing the upper surface pressure suction. In contrast, the negative peak force coefficients obtained at the most critical wind direction of 150° are reduced at higher clearance (G = 40 cm) at regions close to the lower edge of the panels. The higher values are mostly observed on the modules of lower array clearance (G = 20 cm) as the pressure on the upper surface becomes greater than the lower surface reduced pressure.

6.3 Design Force Coefficients

In this section, the experimental force coefficients that could be treated as design loading will be examined and compared in the condition of changing the underneath array clearance. Thus, the experimental force coefficients will be calculated in the same manner as the design force coefficients adopted by different national wind codes and standards for roof-mounted solar panels. As discussed before, the North American Wind Codes and Standards (SEAOC PV2, 2017; NBCC,

2020; and ASCE/SEI 7, 2022) adopt the "envelope procedure" (i.e., the envelope wind tunnel data from all wind directions) for the design force coefficients; while the Japanese Industrial Standard (JIS C 8955, 2017) considers the force coefficients for 0° and 180° wind directions.
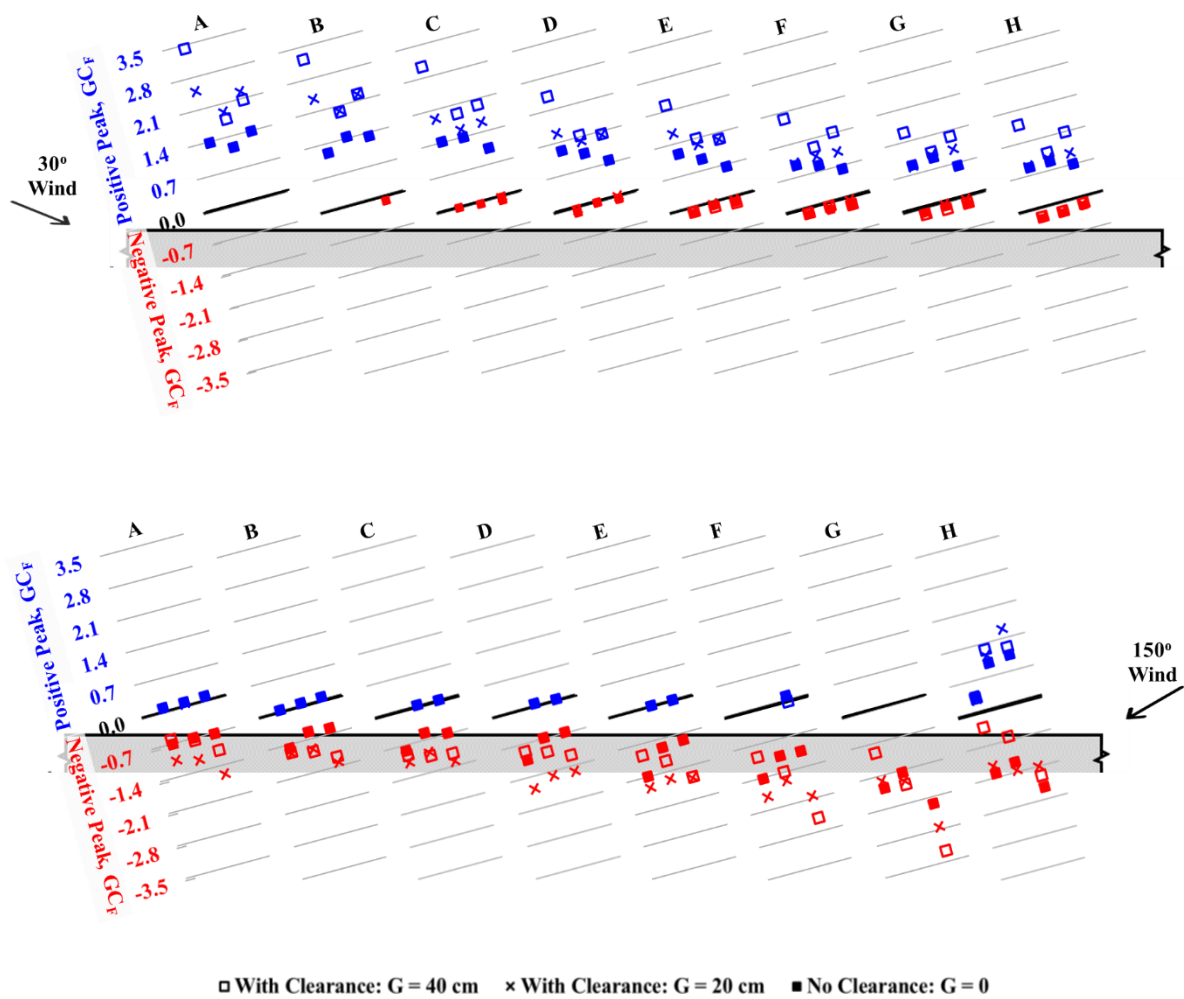
Figure 6.7 Local positive and negative peak force coefficients (GC_F) at the windward edge of the array (Module: M1) at 30° and 150° wind direction

Figures 6.8 and 6.9 present the maximum mean and maximum peak values of the module force coefficients (worst force coefficient within the panel at a particular wind direction that corresponds

to an effective wind area A = 2 m^2). Following the design value definition of JIS C 8955 (2017) of Japan, the module maximum positive mean and peak force coefficients are obtained at 0° wind direction (as presented in Figure 6.8), whereas the module maximum negative mean and peak force coefficients are obtained at 180° wind direction (as presented in Figure 6.9). It is evident that the clearance of the solar array above the roof has influenced the estimation of the force coefficients intended for design purposes.
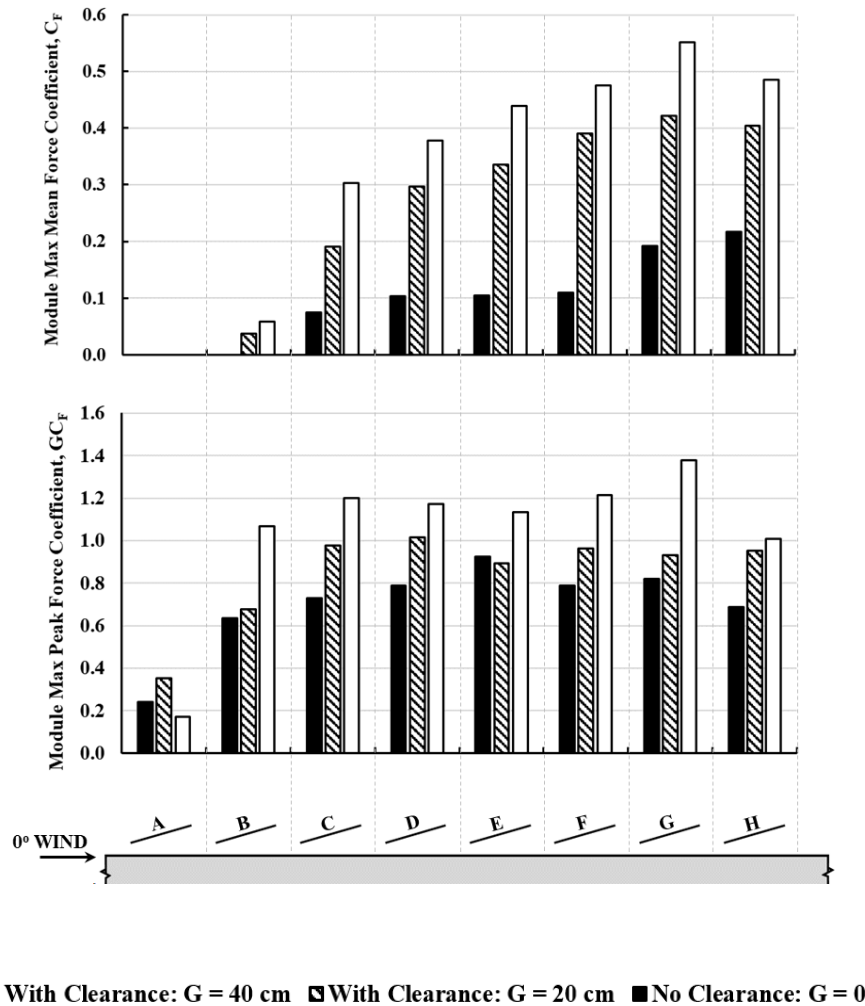
Figure 6.8 Effect of clearance on module maximum positive mean and peak force coefficients at 0° wind direction
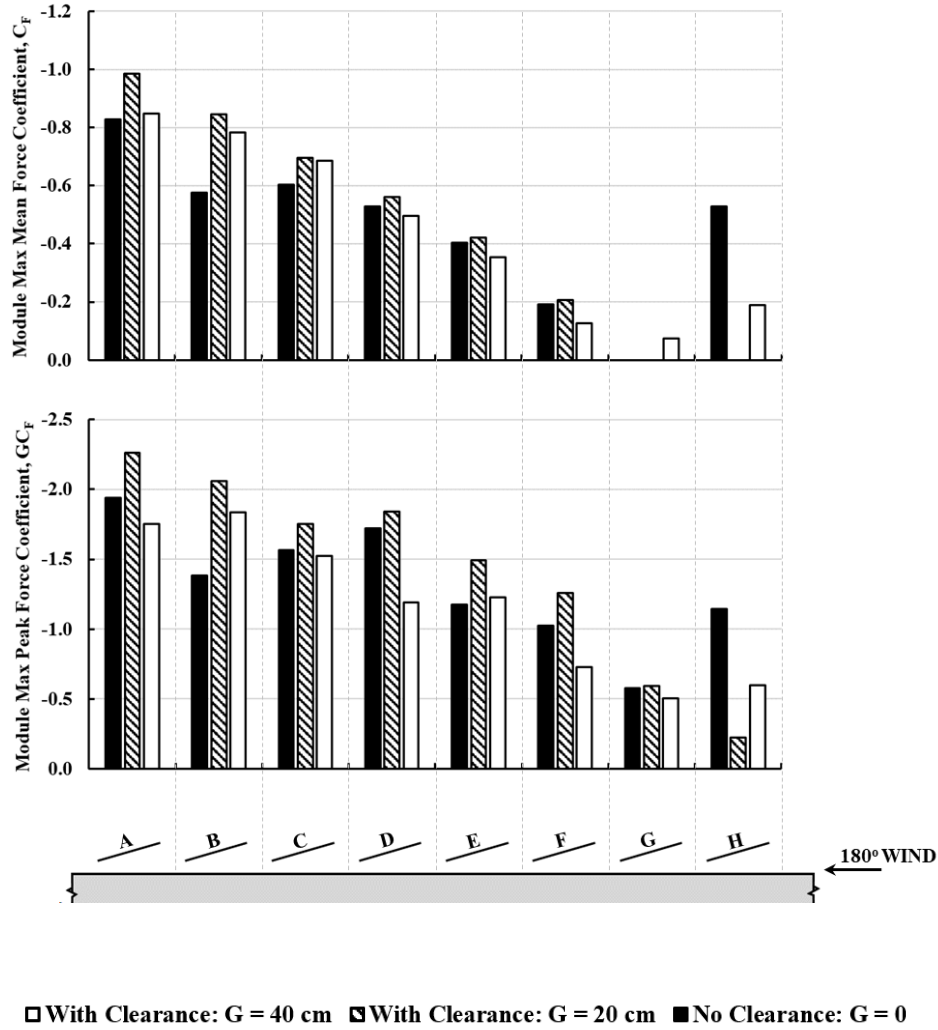
Figure 6.9 Effect of clearance on module maximum negative mean and peak force coefficients at 180° wind direction

The module maximum positive mean and peak force coefficients show a tendency to increase with increasing the clearance between the solar array and the roof. However, as in Figure 6.8, the module maximum positive peak force coefficients of the upstream panel (A) obtained at lower clearance ($G = 20$ cm) are the highest. Thus, the positive mean and peak module force coefficients are increasingly underestimated with the downstream panels at minimizing the clearance of the solar panels (i.e., $G = 0$ and 20 cm). Certainly, that tendency is attributable to the decrease in the

101

local net pressures at regions close to the lower and higher edges of the panel – as mostly dropped by half compared with the corresponding values of the array placed at higher clearance (i.e., $G = 40$ cm). It should be noted that the modules of the upstream panel (A) do not experience mean force coefficients except locally at the regions close to the lower edge of the array at $G = 40$ cm where the local mean force coefficient is found to be about 0.2.

As shown in Figure 6.9, the module negative force coefficients of the upstream panel (H) are greatly increased when $G = 0$. In the downstream direction, minimizing the clearance from $G = 40$ to $G = 20$ cm has generally resulted in overestimating the negative module force coefficients.

Figure 6.10 shows the extreme negative and positive peak force coefficients, which are assessed as loading force coefficients by SEAOC PV2 (2017), NBCC (2020), and ASCE/SEI 7 (2022), among the considered air clearances versus the effective wind area of the panel. It should be noted that the extreme force coefficient corresponding to a particular effective area is the envelope value from all wind directions and all possible loading areas within the panel. Overall, these results are in accordance with findings reported by Kopp (2014) wherein the worst extreme peak force coefficients (i.e., the envelope of the envelope panels' curves) would show little differences with the underneath array clearance. This fact is acknowledged, but there is a considerable discussion to take place in this regard. The study of Kopp (2014) lacked the potential to quantify the clearance effect due to some technical limitations of the experimental modeling. In the experimental modeling of that study, the pressure taps coverage on the lower surface of the panels is reduced compared with the upper surface, where three lines of pressure taps were considered as opposed to only one line along the center of the lower surface. Excluding the pressure taps on the lower surface at regions close to the edges has led to conclude that the array clearance has a minimum impact on the pressure envelope curves, although such regions are highly affected by the clearance
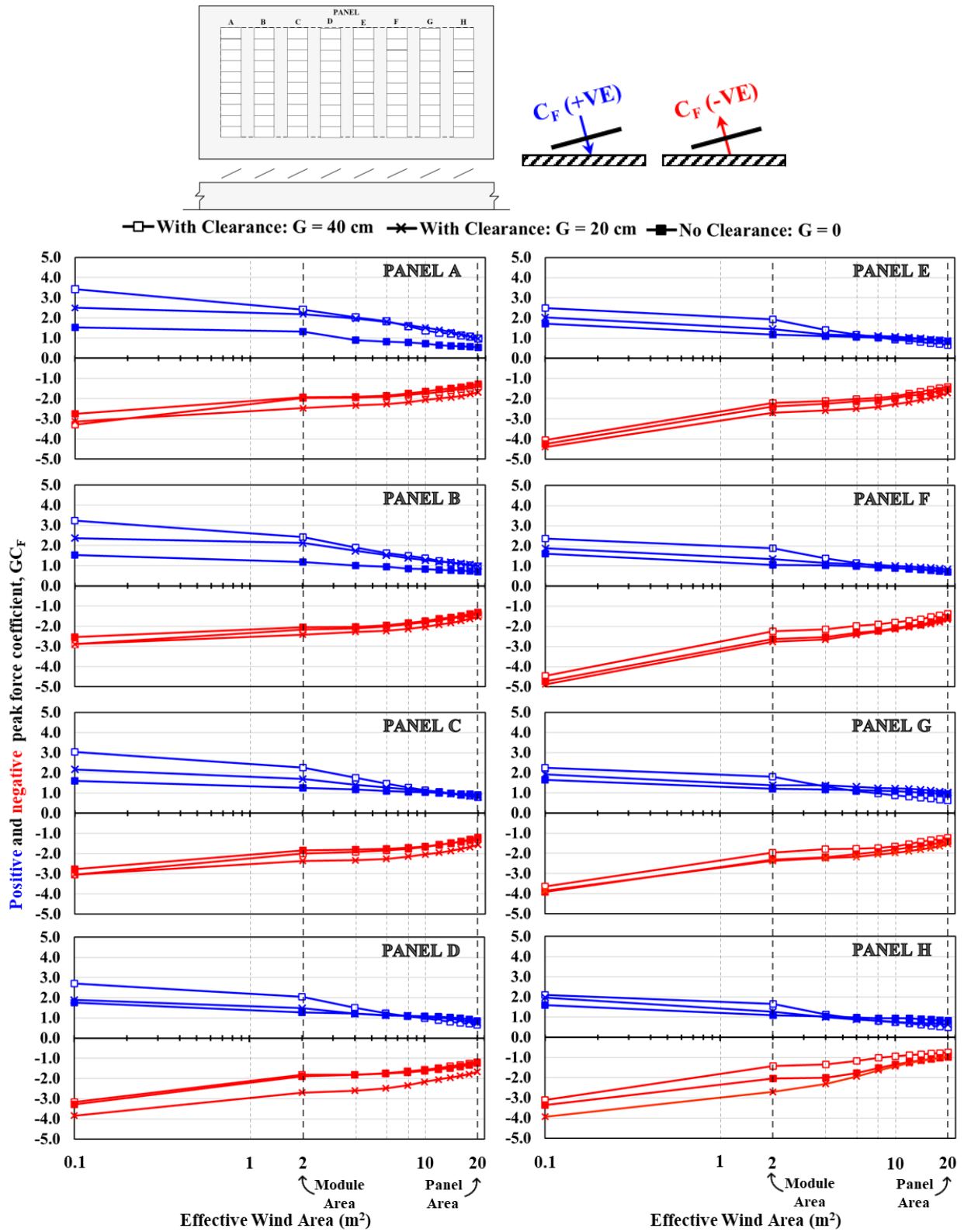
Figure 6.10 Effect of clearance on extreme positive and negative area-averaged peak force coefficients, envelope GC_F.

103

at critical wind directions – as demonstrated subsequently in the present study and that of Wang et al (2020b).

Referring to the extreme peak force coefficient of Figure 6.10, placing the solar array at different clearances above the roof has had uneven extreme peak force coefficients – the topology of the differences between the measurements among the considered clearances can be summarized as follows:

- Differences resulted on the extreme negative peak force coefficients by placing the array at half or zero of the typical clearance vary spatially depending on the panel location within the array.

- Differences resulted on the extreme positive peak force coefficients by placing the array at half of the typical clearance show a strong correlation with the effective wind area of the panel and less correlation with the panel location.

- Differences resulted on the extreme positive peak force coefficients by placing the array at zero of the typical clearance show a correlation with the effective wind area of the panel and the panel location within the array.

In detail, the results provided in Figure 6.10 demonstrate that placing the solar array at no clearance ($G = 0$) largely diminishes the extreme positive peak force coefficients of most of the array panels, particularly the values of the front panels (A and B) and those corresponding to the area of one module or less (GC_F of A $\leq$ 2.0 m^2) of the middle and the back panels. Clearly, the extreme positive peak force coefficients of the front panels at no clearance ($G = 0$) are reduced by one-third. Although the extreme negative peak force coefficients are found to be less affected with placing the array at no clearance ($G = 0$), an increasing tendency is observed on the extreme negative force coefficients of the back panels (G and H) with a factor up to 1.6. In general,

minimizing the underneath array clearance (i.e., from $G = 40$ cm to $G = 20$ cm) tends to decrease the extreme positive peak force coefficients and to largely increase the extreme negative peak force coefficients.

As stated previously, the current wind codes and standards do not incorporate the impact of the underneath clearance of the solar array above the roof. Specifically, the provisions adopted by SEAOC (2017), NBCC (2020), and ASCE/SEI 7 (2022) are applicable exclusively for solar panels installed at a clearance height of 60 cm or less ($G \leq 60$ cm) based on the premise that the air clearance has no bearing within that limit. However, the results of the present study confirm that the underneath air clearance of the solar array presents different tendencies for the extreme force coefficients according to the direction of the net pressure (upward or downward).

To give a clearer illustration of the potential distortions that could be introduced on the design loading coefficients, Figure 6.11 shows the experimental module and panel extreme (envelope) lift and drag force coefficients, which are practically used to design the supports of the solar panel racking systems. Thus, the upward lift forces and the drag forces are respectively used to evaluate the vertical and the horizontal resistance of the posts (in case of mechanically fastened racking systems on roofs) or weights (in case of roof ballasted racking systems).

As clearly illustrated in Figure 6.11, minimizing the underneath solar array clearance would require increasing the upward resistance of the racking system, as the upward lift forces of the modules and the panels broadly increased by 50% when the typical underneath clearance was reduced to half. It is true that the negative lift force coefficients show a reversed trend, but these forces act as a downward thrust on the roof. Thus, increasing the clearance is detrimental to the vertical wind loads transferred to the roof.

Changing the underneath clearance size also influences the drag coefficients. In this case, the
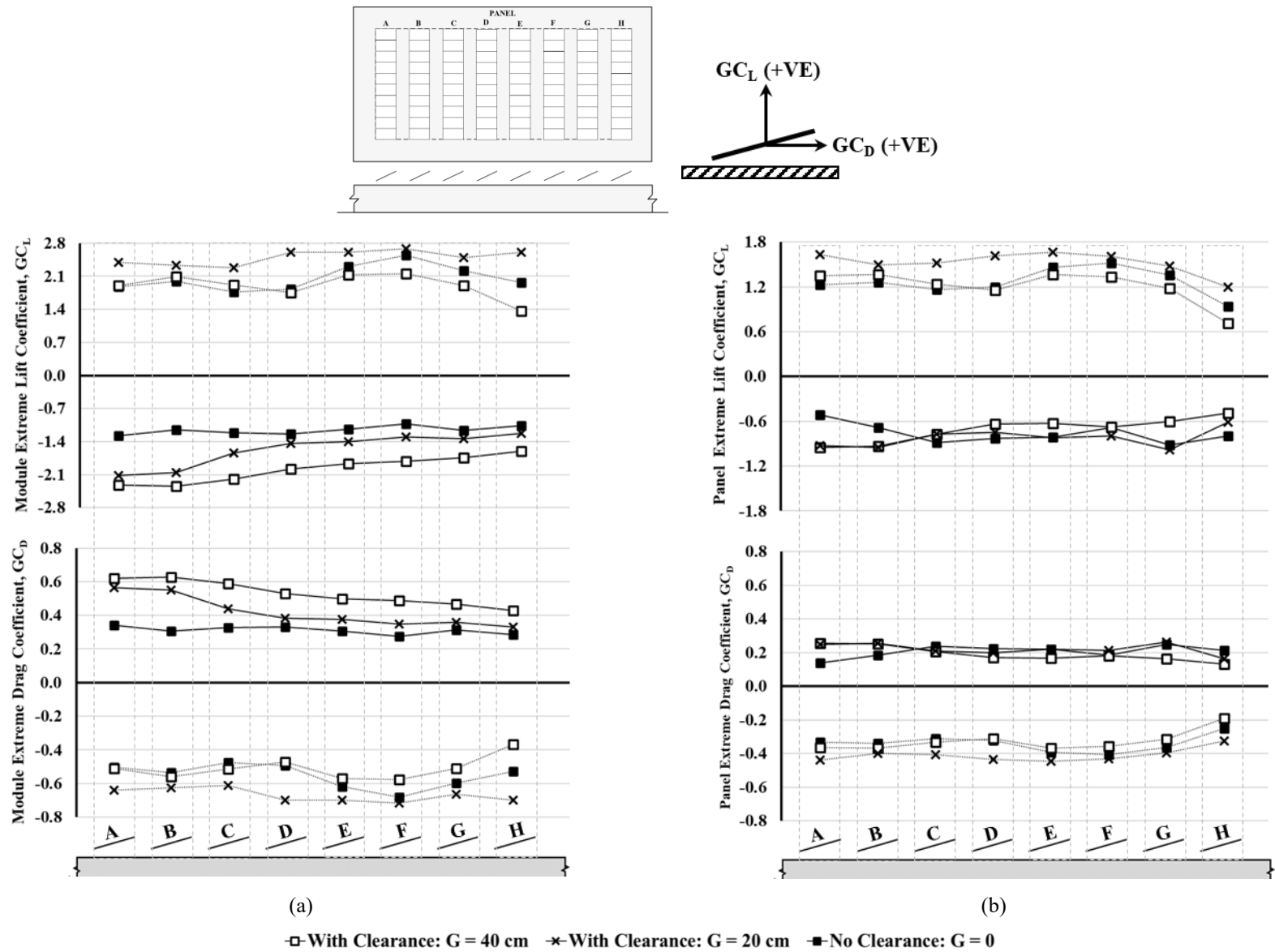
Figure 6.11 Extreme peak lift and drag force coefficients (GC_L and GC_D) for: (a) Solar module, and (b) Solar panel

comparison shall be made without considering the direction of the drag forces (left or right) since they are perceived as horizontal resistance required by the supports of the racking system. Accordingly, comparing the worst values of the positive and negative (right and left, respectively) extreme drag force coefficients shows that reducing the clearance to half has resulted in enlarging the drag coefficients of the middle panels by 30% and the back panel by 60%. To a lesser extent, placing the array at no clearance has reduced the drag resistance of the module and the entire panel by 20% of the upstream panels (A, B, C, and D) and on the other side enlarged the drag coefficients of the back panels by 30%.

The results provided in this section have revealed that the wind tunnel experimental results assigned as design force coefficients are particularly sensitive to air clearance underneath the solar array model; therefore, such coefficients based on violating such geometry layout may compromise the credibility of the design and the safety of the structures, particularly when the case is underestimating. The provided results may also assist solar panel practitioners and engineers in this concern which is not specifically dealt with in existing codes and standards provisions.

CHAPTER 7 EFFECT OF PRESSURE TAPS COVERAGE

This part of the study is primarily concerned with the degradation of the surface and the net pressures over the panels with the wind direction, determined by the distribution and number of pressure taps implemented on the surfaces of the solar panels to allow reliable evaluation of wind-induced pressure. In this regard, the degradation of the surface and the net pressures the of the panels of the solar array tilted at angle $\omega = 15°$ will be investigated.

A portion of the work provided in this chapter has been presented at several conferences (Alrawashdeh and Stathopoulos, 2022a, 2022c, 2022d).

7.1 Mean and Peak Pressure Coefficients

In this section, the basic aerodynamic characteristics of the solar panels mounted on a flat roof are highlighted to understand the extent and nature of changes that have occurred on the surface pressures, particularly the wind pressure degradation with the wind direction.

Figures 7.1 and 7.2 respectively provide contours of the local mean pressure coefficients on the upper and lower surfaces of the panels at the considered wind directions. As clearly shown, the panels' surfaces are greatly dominated by suction pressures (i.e., negative mean). For winds between 0° and 75°, the mean suction on the lower surface is found to be higher in magnitude than those of the upper surface. Similar values are observed at 90° wind directions. With further increasing the wind direction, mean pressure coefficients of the upper surface came to prevail over the corresponding pressures induced on the lower surface.

As shown in Figures 7.1 and 7.2, the surface wind suction at 0° wind direction collapsed on the downstream panels and rebounded again on the back panels of the array (G and H) due to the
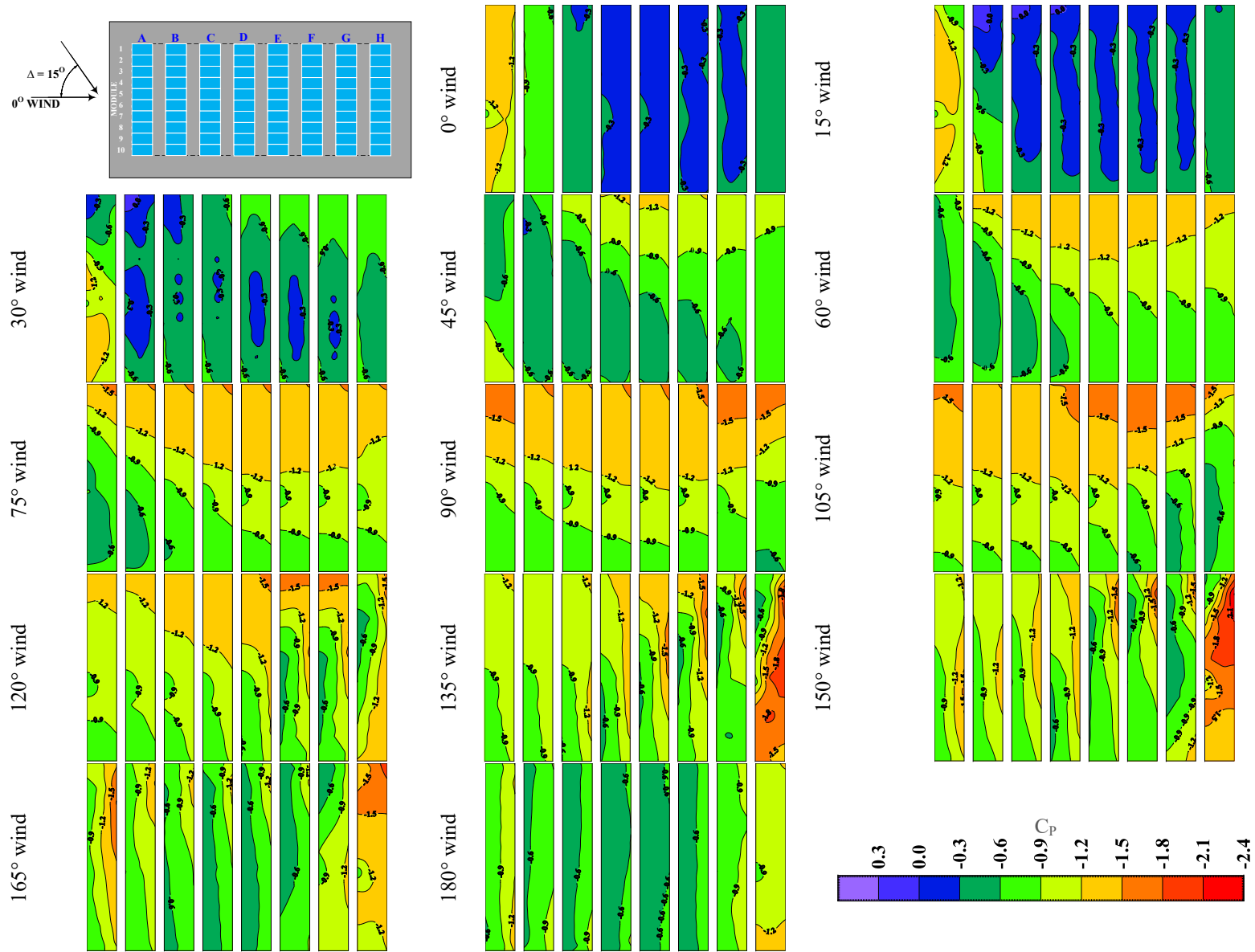
Figure 7.1 Contours of local mean pressure coefficients, C_P, on the upper surface at the considered wind directions
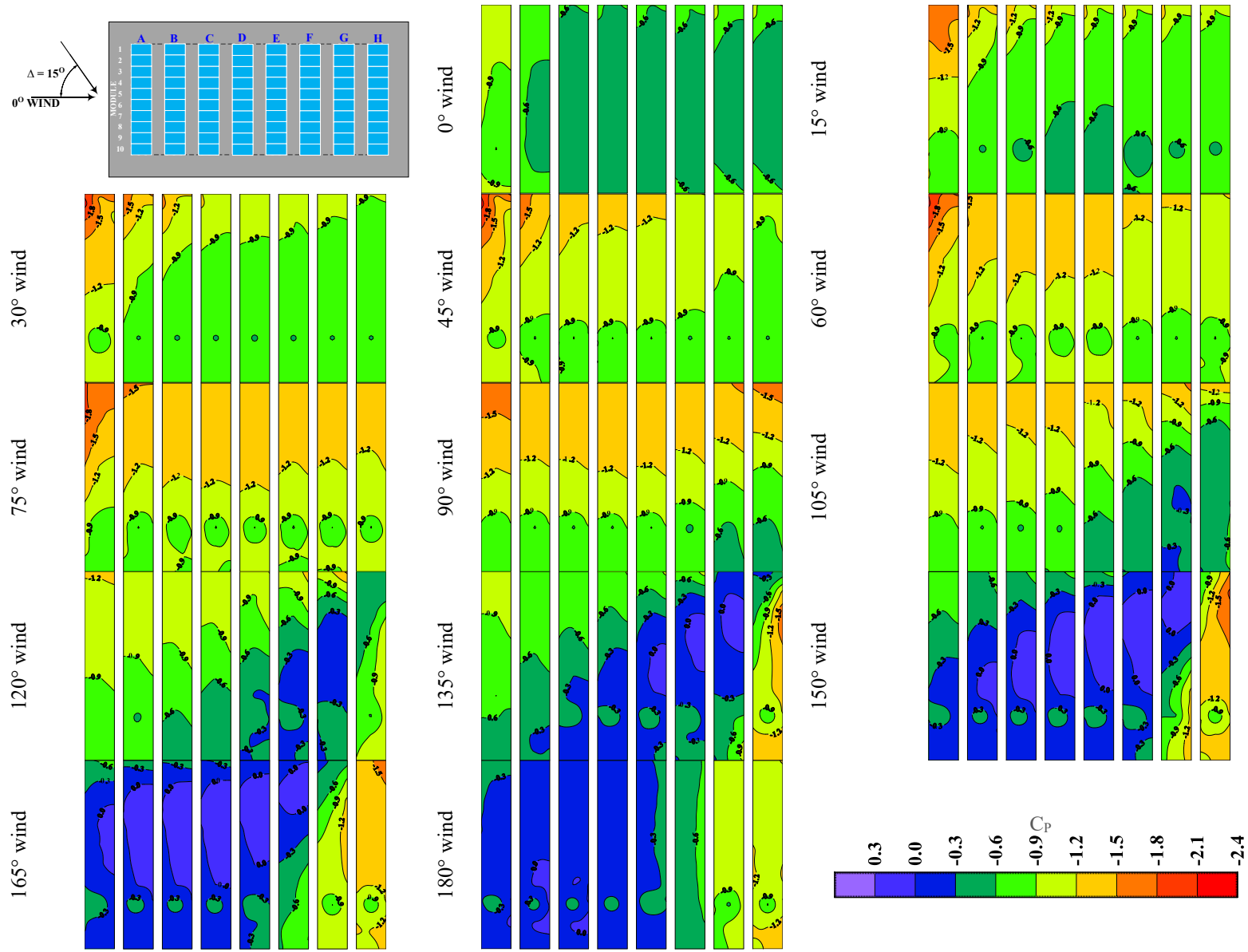
Figure 7.2 Contours of local mean pressure coefficients, C_P, on the lower surface at the considered wind directions

interaction of the reattached flow with the higher edges with a notable degradation observed on the upper surface where the highest values observed in regions close to the lower edge of the modules. At 180° wind, the mean surface pressure coefficients exhibit a similar distribution pattern as of the 0° wind but with higher values, thus higher values are observed on the upstream panels of the array and then the values declined at the middle panels and then recovered at the downstream panels (B and A). Contrary to 0° wind direction, higher values of mean pressure coefficients are induced in regions close to the higher edge of the panel and lowest values in regions close to the lower edge of the panels. This may be a result of the air clearance underneath the panels, at which high turbulence regions are generated due to flow separation. At 90° wind, higher mean pressure coefficients are observed on the surfaces of the upstream modules, i.e., half of the array on the windward side of the roof.

The presence of vortexes detached from the leading edges of the roof at oblique wind directions has surely played a significant role in influencing the distribution of the surface pressure. As shown in Figures 7.1 and 7.2 for oblique wind directions, the wind suctions induced on the surfaces of the panels have further escalated and spread to a larger region over the array's panels mainly due to the separation of the conical vortices, which has a downflow nature, at the higher edge of the panels. That is, disparities in the values of the upper and lower surface mean pressure coefficients culminated at wind directions of 15°-60° and 135°-165°, respectively. At 15°-60° winds, the greatest differences have been observed at the windward corner modules, while for wind directions between 135° and 165° the differences are more clearly observed at modules located in the field of the array. These wind directions are therefore considered unfavorable to the net pressure of these solar modules, as pressure equalization is less likely to occur.

The distribution of the mean pressure coefficients provided by Figure 7.1 demonstrates that

the wind-induced pressures on the upper surface of the PV panels exhibit a steep degradation in the chordwise direction, where the highest mean pressure coefficients are mostly observed in regions close to the higher edge of the panels and decreases in values towards the regions close to the lower edge. This is clearly reflected by the closed contour lines of the mean pressure coefficients of the upstream modules at unfavorable wind directions (i.e., 120°-150°). On the other hand, the local mean pressure coefficients on the lower surface of the array have also experienced degradation, but to a lesser extent than the pressure coefficients on the upper surface. As shown in Figure 7.2, the mean pressure coefficients of the lower surface of the edge modules of the upstream panels were subjected particularly to pressure degradation in the chordwise direction where higher suction is induced in regions close to the higher edge of the panels.

However, further clarification is required as to the surface negative peak pressure coefficients. Figure 7.3 provides the distribution of the negative peak pressure coefficients of the upper and lower surface obtained at wind directions of 150° and 30°, respectively. Recalling the fact that those wind directions are unfavorable for the wind-induced pressures on the panels' surfaces. Contours of the negative peak surface pressure coefficients tie well with the previous contours of the mean pressure coefficients wherein the local negative peak pressure coefficients of the upper surface have steeply degraded in the chordwise direction while the negative peak pressure coefficients of the lower surface have appeared nearly uniform except for the windward modules at the array edge which were exposed to degradation in the chordwise direction.

From practical perspectives, high local peak suctions on the upper surface may certainly lead to cracking the module upper surface cover plate, their higher degradation nevertheless constitutes a very high risk on the stability of the module cover plate as to be loose or peeled out from the circumference supporting frame of the PV module. The same is applied to the lower surface

backing sheet of the PV modules located on the solar array edges.
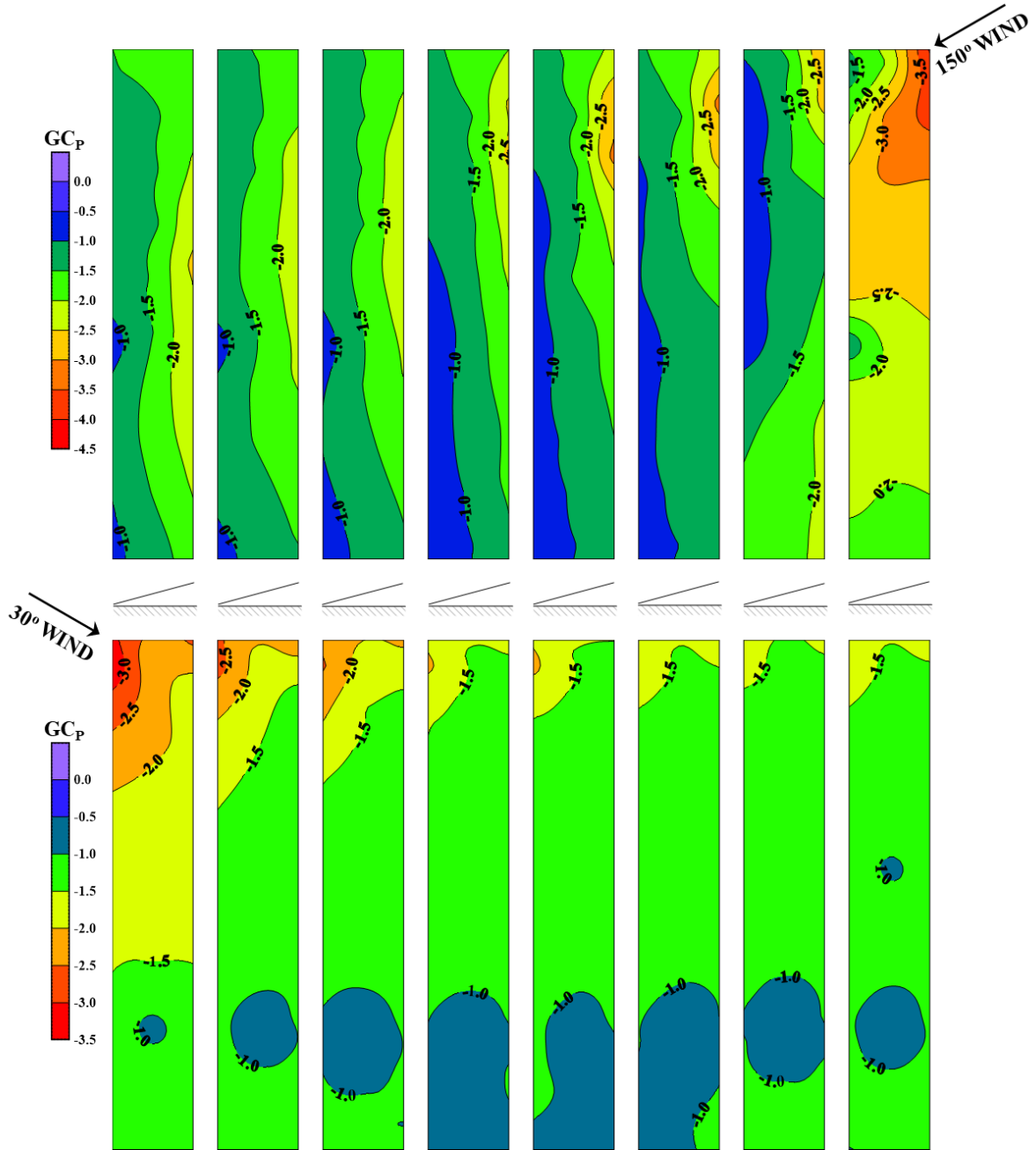
Figure 7.3 Contours of local negative peak pressure coefficients, GC_P, on the upper and lower

surfaces at respectively wind directions of 150° and 30°

7.2 Mean and Peak Force Coefficients

The present section mainly sets forth the mean and peak net pressures (force coefficients), taking into account the pressure taps configurations illustrated by Figure 4.8, for the purpose of discussing the net degradation over the module and the panel area. In this context, the module mean and peak force coefficients, namely C_F and GC_F corresponding to effective wind area $A = 2.0$ m^2, have been numerically calculated for each pressure taps configuration and wind direction.

Figures 7.4 and 7.5 show the module maximum mean and peak force coefficient over the panel for each particular wind direction. Thus, the values provided in these figures are the worst force coefficients at each particular pressure taps coverage and wind direction for an effective wind area of 2.0 m^2. As can be seen by these figures, the variations of the maximum module mean and peak force coefficients show a similar pattern with the wind direction, but different values among the considered pressure taps coverages. Generally, it is observed that the maximum module positive mean and positive peak force coefficients of Conf. 4 are the highest compared with other configurations. Also, the highest module maximum negative mean and negative peak force coefficients in absolute value are mostly obtained by Conf. 2.

Moreover, among the considered coverages of pressure taps, the maximum module positive mean and positive peak force coefficients are appeared to be the highest heterogeneity at wind directions ranging from 15°-45°; whereas, the maximum module negative mean and negative peak force coefficients show the highest heterogeneity at winds ranging from 120°-165°. This may indicate that the positive and negative net pressures are of higher degradation over the array panel at wind directions of 15°-45° and 120°-165°, respectively. Bearing in mind that, these ranges of wind directions are respectively unfavorable for wind-induced pressures on the upper and lower surface; and hence, extreme net pressures (upward and downward) are developed at these wind
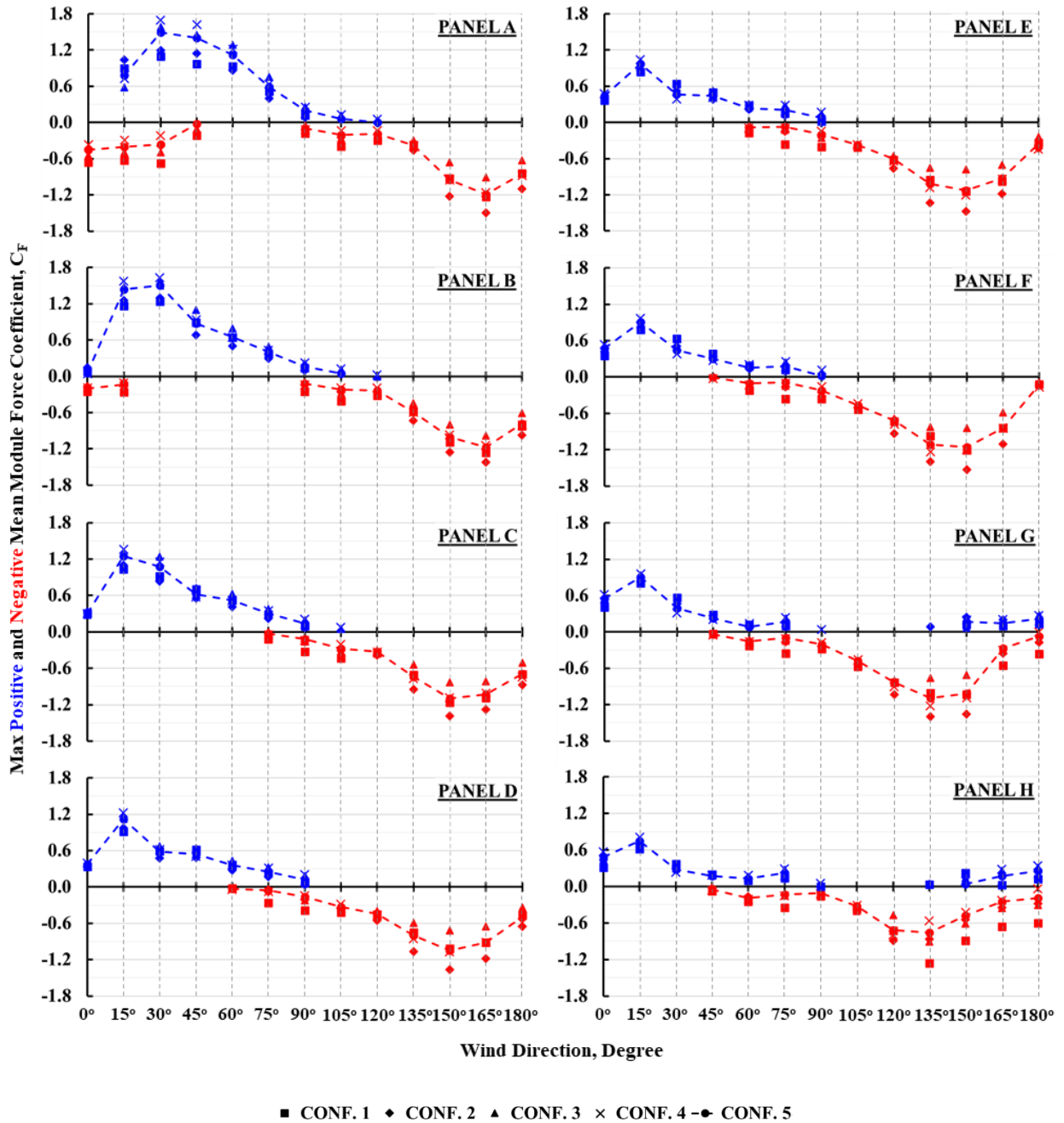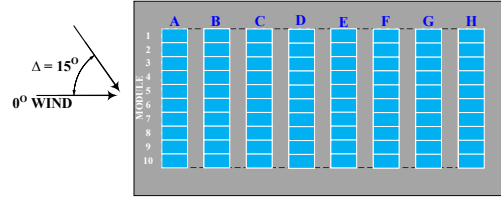
Figure 7.4 Variation of the module maximum mean force coefficients, C_F of 2.0 m^2 effective area, with the direction.
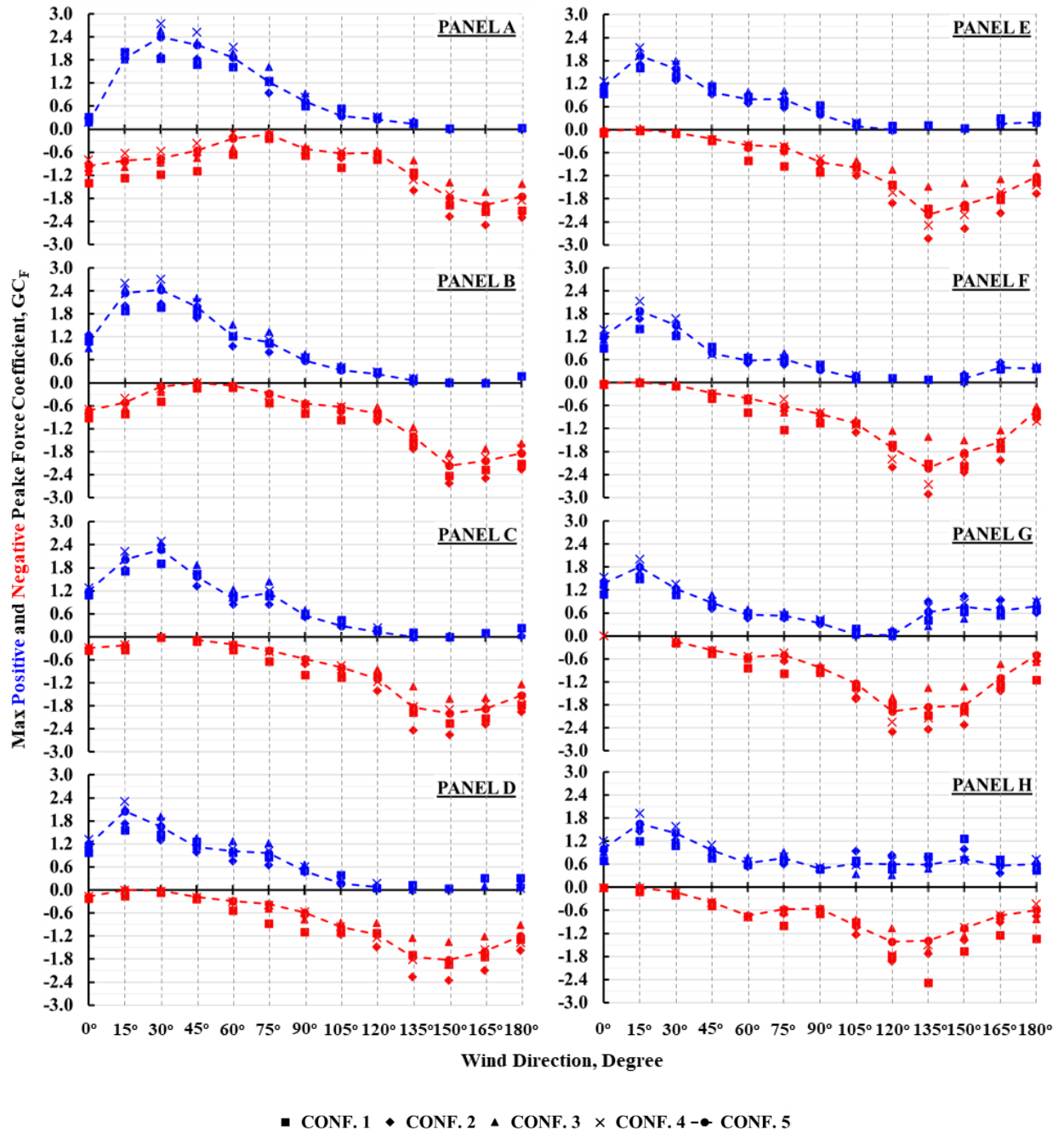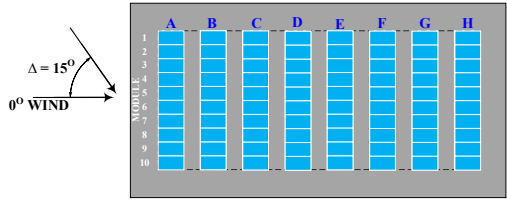
Figure 7.5 Variation of module maximum peak force coefficients, GC_F of 2.0 m^2 effective area, with the wind direction.

directions since the pressure equalization across the panel will be at the lowest level of development.

To obviously demonstrate the local force coefficients degradation at these critical wind directions, Figures 7.6 and 7.7 show contours of the local distribution of the mean and peak force coefficients of the array for wind directions 30° and 150°, respectively. As illustrated, the panels of the array have dominated by positive mean net pressure for the wind direction of 30° with higher values observed on regions close to the lower edge of the panels – See Figure 7.6.

The distribution of mean force pressure coefficients at 150° wind direction, provided in Figure 7.7, appears to be somehow different than that of 30° wind direction; thus the negative mean pressures dominate the areas of the panels with higher severity on regions close to the higher edge and sharply decrease in value towards the regions at the lower edge of the panels. Admittedly, the concern local peak force coefficients have seen a substantial degradation over the panels of the array, most likely about 3.0 in the chordwise direction (i.e., across the regions between the higher and lower edges of the panels).

In addition to the local measurements of the mean and peak force coefficients, the cross-correlations of the fluctuating pressures were computed for the pressure taps located in the chordwise direction. This is to additionally understand the influence of pressure taps coverage on the area-averaged force coefficients. In this context, the correlation coefficients of the fluctuating force coefficients of regions located at the middle and higher edge of the module have been evaluated with reference to the region located close to the lower edge of the module according to the following equation:

$$R_{C_F}(X_1, X_2) = \frac{\overline{C_{F,X_1}(t) \times C_{F,X_2}(t)}}{\sqrt{\overline{C_{F,X_1}^2(t)} \times \overline{C_{F,X_2}^2(t)}}} \qquad\qquad 7.1$$

in which the subscript X_1 refers to the region close to the lower edge of the module and X_2 refers to the region in the middle or close to the higher edge of the same module. The values of the correlation coefficients at wind directions of 30° and 150° are locally provided on the contours of mean force coefficients of Figures 7.6 and 7.7, respectively.

The cross-correlation of the force coefficients, at 30° wind direction provided in Figure 7.6 and at 150° wind direction provided in Figure 7.7, have quite similar distributions. The correlation coefficients were found to be positive in value at the considered wind directions, which signifies that the local regions of the solar module have simultaneously experienced the same wind action, i.e., upward or downward net pressure depending on the wind direction. On the other hand, it is apparent that the fluctuating force coefficients of regions close to the higher and lower edges of the panels do not appear to be sufficiently correlated, where R_{C_F} values were found to be in the range of 0.2-0.6. For fluctuating force coefficients of the region close to the middle of the solar module, comparatively higher cross-correlations have been observed.

The lack of cross-correlation between the force coefficients of regions close to the panels' edges can be attributable to the nature of the local separation that mainly occurred at the higher edge of the solar panels depending on the wind direction. Investigating of the chordwise cross-correlations of the fluctuating surface pressure $\left(R_{C_P}\right)$ at these winds of direction 30° and 150°, which are provided in Appendix C for sake of brevity here, pointed to the fact that the wind-induced pressures on the lower surfaces of the solar panels at these wind directions found in good correlation, at which R_{C_P} values found mostly in the range of 0.7-0.9. Contrarily, the wind-induced
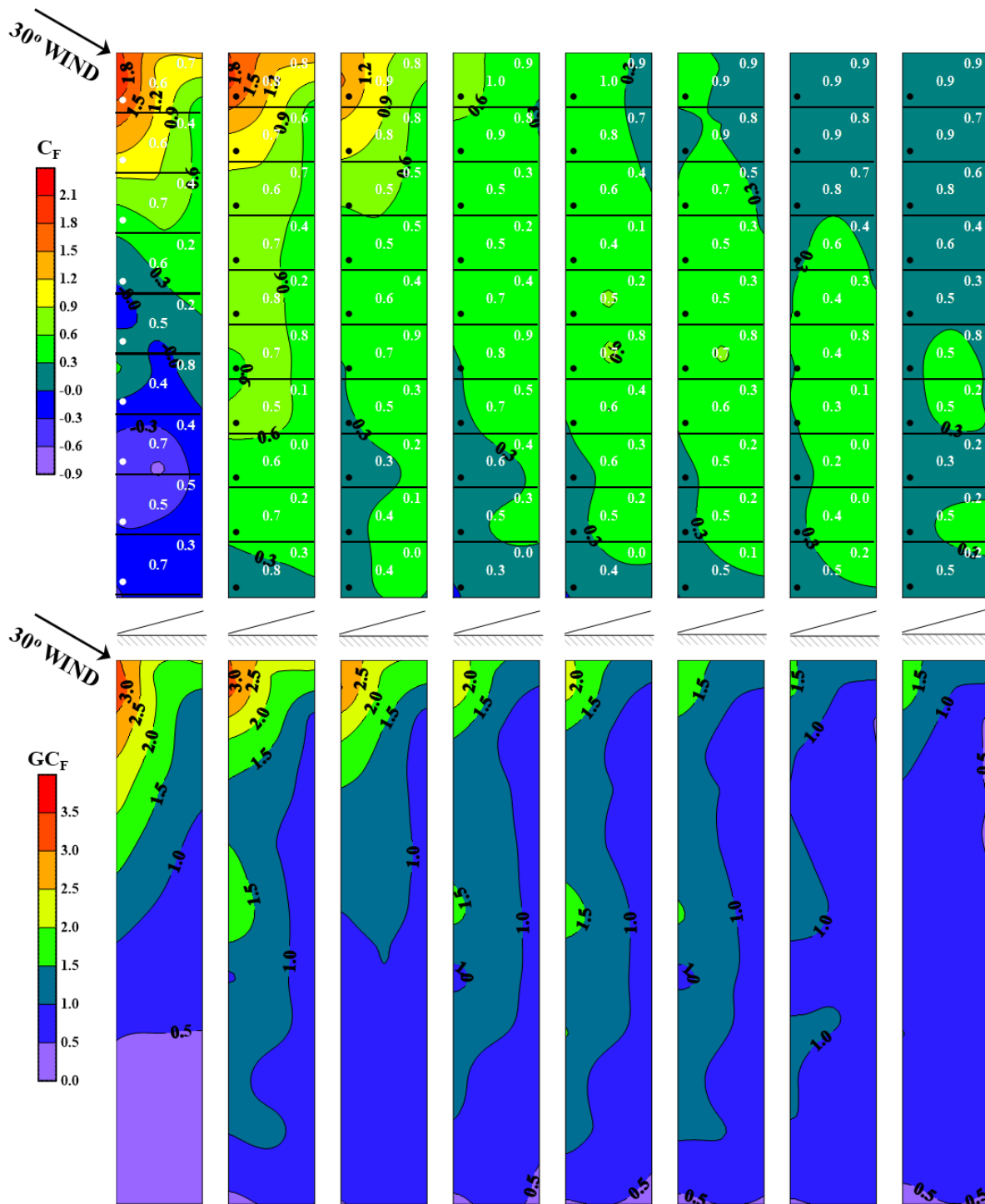
Figure 7.6 Contours of local mean (C_F) and positive peak force coefficient (GC_F), values shown in black, and the chordwise cross-correlation, values shown in white, for 30° wind direction
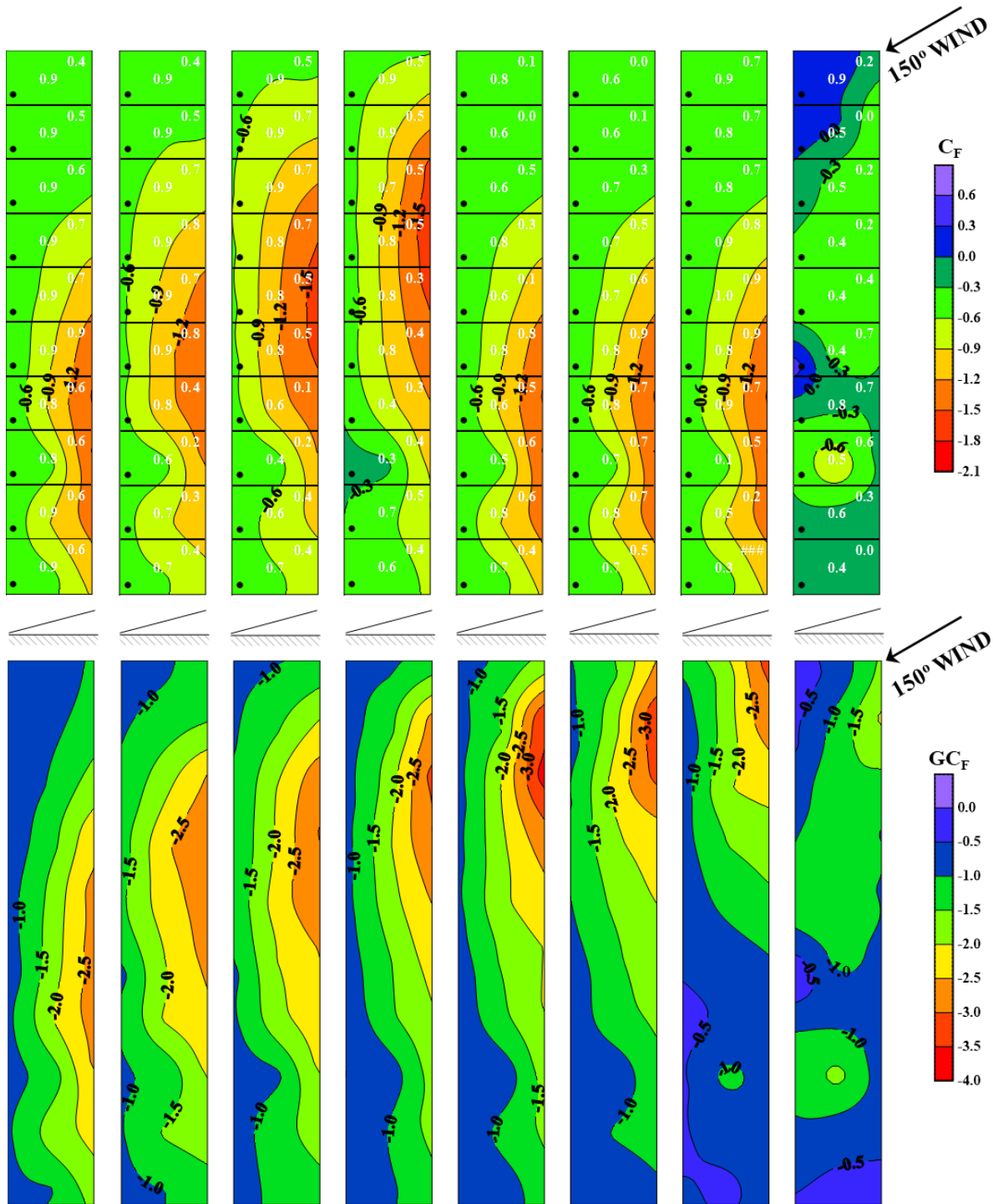
Figure 7.7 Contours of local mean (C_F) and negative peak force coefficient (GC_F), values shown in black, and the chordwise cross-correlation, values shown in white, for 150° wind direction

pressures on the upper surface were found to be poorly correlated in the chordwise direction. That is, except for the modules located on the windward edges of the array, R_{C_P} values were found ranging between 0.1 and 0.4. Furthermore, negative correlations have been observed on the upper surface pressures of regions close to the higher and lower edges for some modules located within the field of the array because different separation mechanisms occurred at the higher and lower edges of the panels resulting in vortex shedding of an antisymmetric pattern. As those modules are exposed to the horizontal flow (parallel to the roof) of the reattached streamlines of the large-scale conical vortices.

Therefore, the very poor cross-correlations of the fluctuating net pressures (e.g., positive and negative force coefficients) in the chordwise direction, particularly between regions near the higher and lower edges of the solar module, were stemmed by the subtraction of the very poor correlated upper surface pressures and the relatively well-correlated lower surface pressures.

7.3 Design Force Coefficients

As pointed out previously, there are striking disparities in the values of the positive and negative peak force coefficients by the pressure taps coverage due to high net pressure degradation within the module area, particularly at critical wind directions. Therefore, it is of great importance to assess the effects of pressure taps coverage on the experimental force coefficients that would be deemed as design loading for the credibility and integrity of the wind-tunnel setup established for codification-oriented studies. To this end, the mean and peak area-averaged force coefficients (force coefficients versus the effective wind area of the panel) obtained at 0°, 30°, 150°, and 180° will be examined.

121

Figure 7.8 shows the maximum module positive mean and peak force coefficients at 0° wind direction; and the maximum module negative mean and peak force coefficients at 180° wind direction among the considered pressure taps coverages. Noting that such results are regarded by JIS C 8955 (2017) as the design loadings. The module positive force coefficients evaluated in Figure 7.8 (a) reveal a general trend of lowering the positive peak force coefficients when disregarded the pressure taps at regions close to the module edges – as these regions experienced relatively high positive net pressure at 0° wind direction. For instance, considering only one pressure tap in the middle of the module (i.e., Conf. 1) or only two pressure taps arranged (as per Conf. 2) has resulted in positive mean and peak force coefficients of lower values in comparison with results of the other configurations. Certainly, the highest module forces are generated when considering pressure taps in regions close to the higher and lower edges of the module (i.e., Conf. 4) - see Figure 7.8 (a).

Moreover, the comparison of the module negative mean and negative peak force coefficients at 180° wind direction, provided in Figure 7.8 (b), shows that omitting the pressure taps from regions close to the module high edge results in undervaluing the positive net pressure (e.g., the negative mean and peak force coefficients obtained according to Conf. 3), where such regions experienced high upward net pressures.

Continuing past practice, Figures 7.9 and 7.10 present respectively the area-averaged maximum mean and peak force coefficients among the considered pressure taps coverages, including positive force coefficients at 30° wind direction and negative force coefficients at 150° wind direction. Certainly, the rationale behind the focus on the area-averaged force coefficients obtained at these wind directions is that the wind directions 15°-45° and 135°-165° are the most critical directions for the positive and negative values, respectively. Thus, the extreme area-
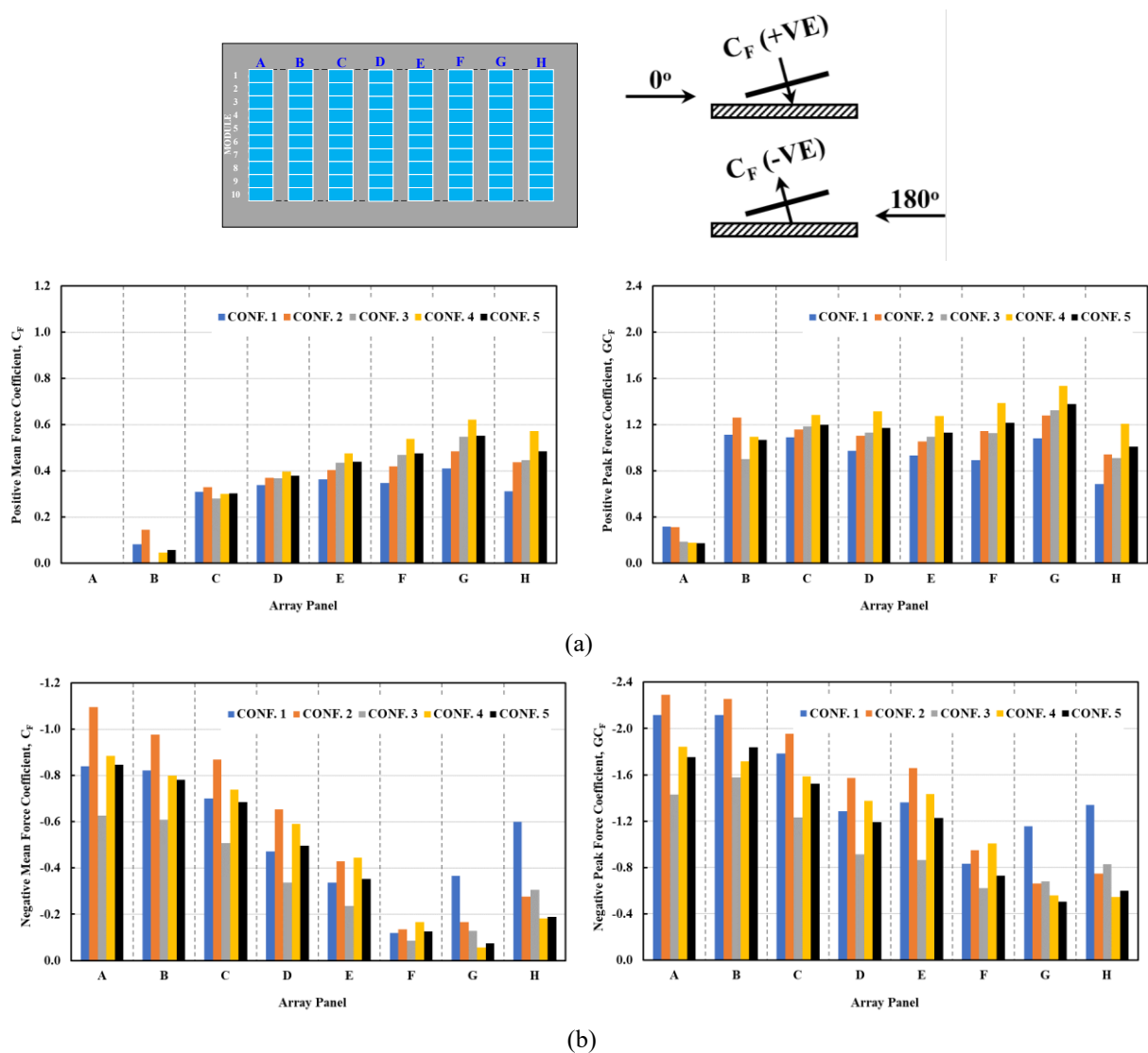
Figure 7.8 Module maximum positive and negative of mean and peak force coefficients, C_F and GC_F of 2.0 m^2 effective area, for wind direction of: (a) 0° and (b) 180°

averaged force coefficients were mostly produced at these wind directions; and hence, these values may be somewhat similar or may even overlap with the envelope curves.

As shown in Figures 7.9 and 7.10, considering one pressure tap at the module middle (Conf. 1) is not sufficient enough as taps coverage for the area-averaged peak force coefficients, in which
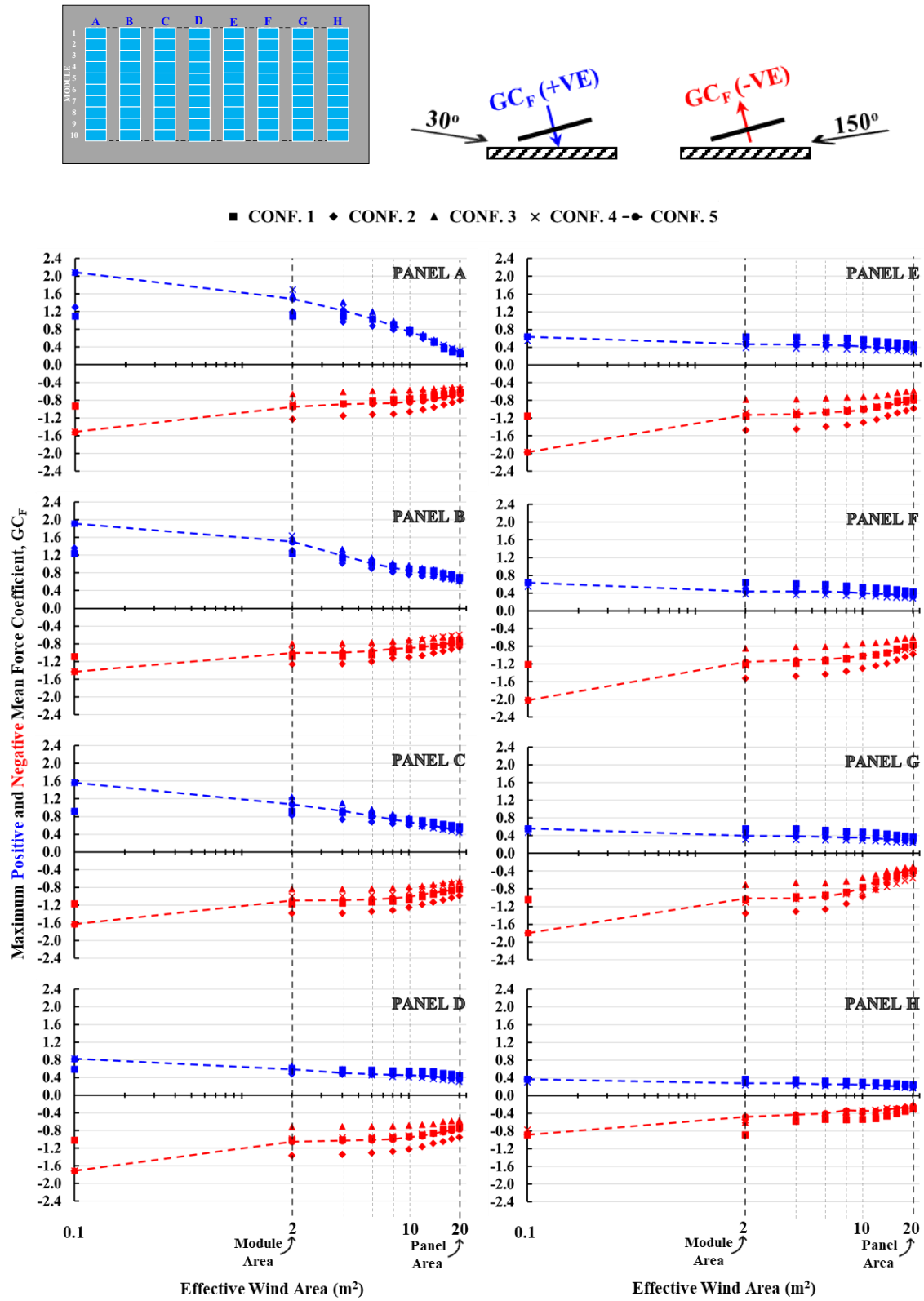
Figure 7.9 Variation of the maximum mean force coefficients, C_F, versus the effective wind area of the panels - positive at 30° wind and negative at 150° wind

124
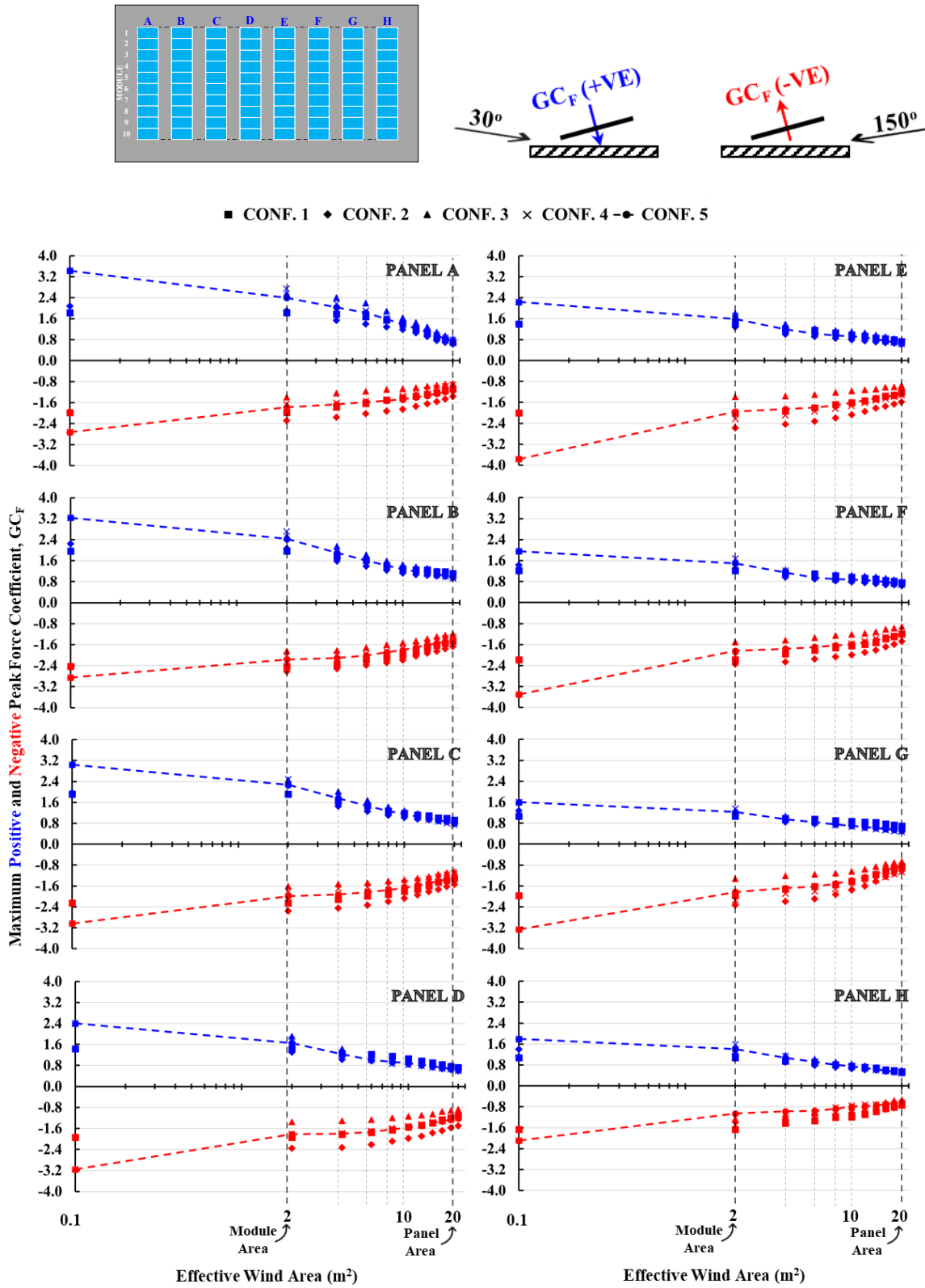
Figure 7.10 Variation of the maximum peak force coefficients, GC_F, versus the effective wind area of the panels - positive at 30° wind and negative at 150° wind

the negative mean and peak area-averaged force coefficients have been underestimated by a factor of about 2.0 on most panels for effective wind areas corresponding to area of one module ($2\ m^2$) or less.

Furthermore, considering two pressure taps (i.e., Confs. 2 and 3) may lead to poor evaluation for the negative and positive area-averaged force coefficients. The negative area-averaged mean and peak force coefficients obtained through Conf. 2 show higher values than the corresponding values of Conf. 5, mostly of a factor of 1.3 for effective wind area larger than $2\ m^2$; however, on the other hand, the positive area-averaged mean and peak force coefficients of Conf. 2 are found lower than those of Conf. 5 by a factor of 0.7 for all effective wind areas. In contrast to the trends of Conf. 2, the area-averaged mean and peak force coefficients obtained through Conf. 3 show overvaluing and undervaluing tendency for the positive and negative peak force coefficients of Conf. 5, respectively.

The negative and positive area-averaged peak force coefficients obtained by considering Confs. 4 and 5 were broadly similar, with a discrepancy within 5%. Obviously, this is due to the net pressure distribution where the negative peak net pressures are influential in the regions close to the higher edge of the panels, while the positive peak net pressures dominate the regions close to the lower edge of panels. This is largely reflected by the local mean and peak force coefficients, such that the local negative mean and peak force coefficients obtained through Conf. 1 and 3 were found to be lower than the corresponding values of Conf. 5 by a factor ranging from 0.5 to 0.8, whereas local force coefficients of the Conf. 2 and Conf. 4 show identical results with Configuration 5. On the other hand, the local positive mean and peak force coefficients of Conf. 5 were mostly 1.6 times the corresponding values of Conf. 1 and 2, and in great similarity with the local coefficients of Conf. 3 and 4.

A closer look at the technical conducts considered by literature studies towards overcoming the barriers associated with the pressure taps installation on the wind tunnel model found that these studies resorted to reducing the pressure taps coverage on the lower surface compared to the upper surface. As formerly discussed, Kopp et al. (2012) and Kopp (2014) have considered three lines of pressure taps on the upper surface compared to only one line of pressure taps along the center of the lower surface. Certainly, the last study would be of a case in a point for further discussing, and report on successes, problems, and shortcomings of such pressure taps coverage. As this particular study was comprehensively concerned with the design pressure coefficients of roof-mounted solar panels, namely the envelope curves of various geometric parameters. Therefore, it would be assumed that the pressure taps coverage at the lower surface are minimized and increased on the upper surface of the panels with attention given to the panel edges.

To verify this assumption and to identify the importance of the pressure taps alignment on the surfaces of the solar panels model, results at pressure taps coverage of Conf. 6 are determined for comparisons making with the results obtained according to pressure taps at Conf. 5 of identical and densest pressure taps coverage on the panel's surfaces – see Figure 4.8 for details of the pressure taps coverage. Figure 7.11 presents the variation of the extreme area-averaged negative and positive mean and peak force coefficients with the effective wind area of the panel obtained at pressure taps coverage at Conf. 5 and Conf. 6. Clearly, the extreme negative area-averaged mean and peak force coefficients show high agreement with the corresponding values of the identical distribution. On the other hand, utilizing only one line of pressure taps on the lower surface (i.e., conf. 6) has greatly undervalued the extreme positive mean and peak area-averaged force coefficients, in particular for loading areas less than 4.0 m^2 with a factor of about 1.6.

The recorded time histories of module force coefficient for modules located at the edge of the
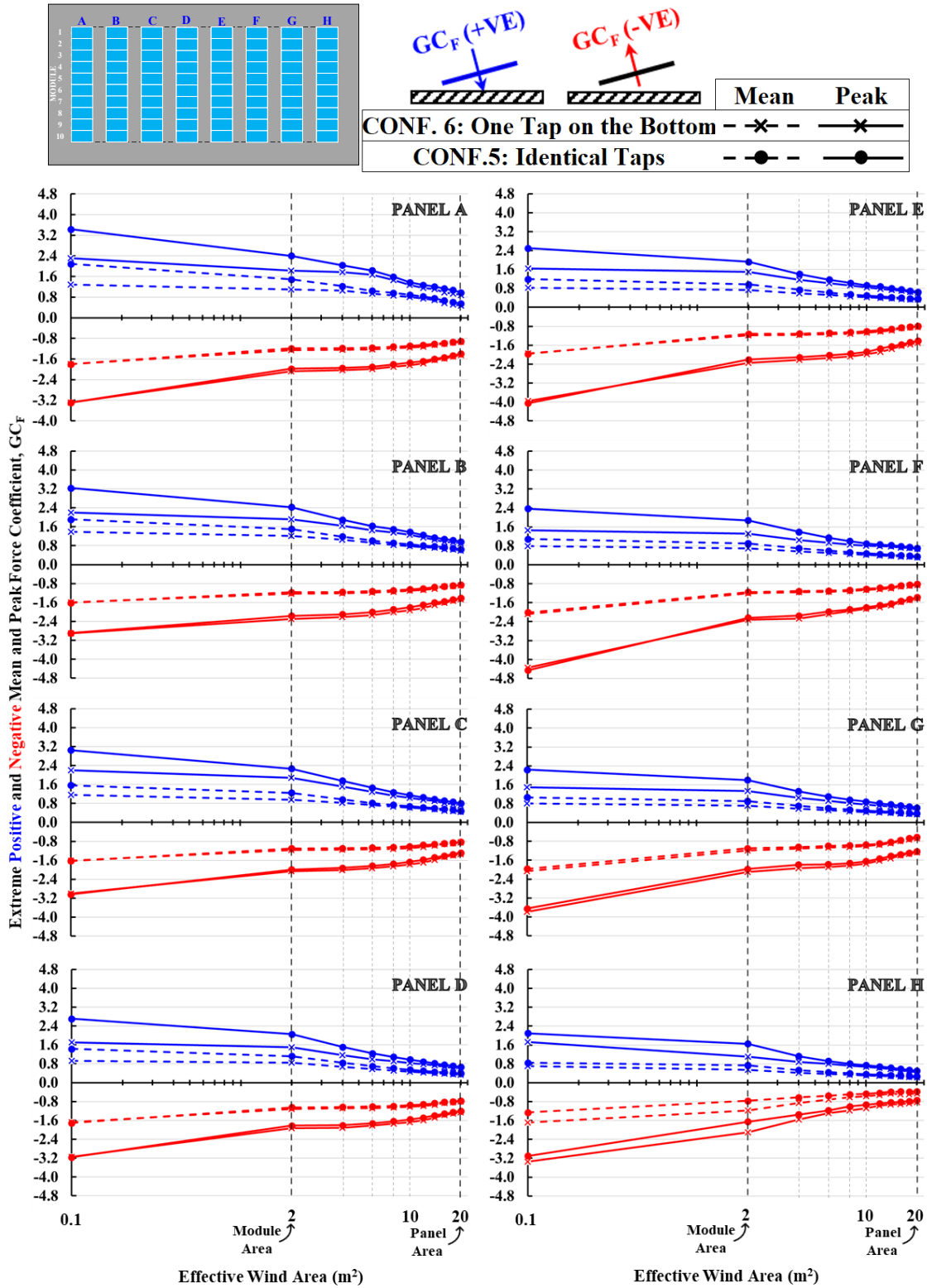
Figure 7.11 Variation of the extreme mean and peak force coefficients, C_F and GC_F, versus the effective wind area of the panels
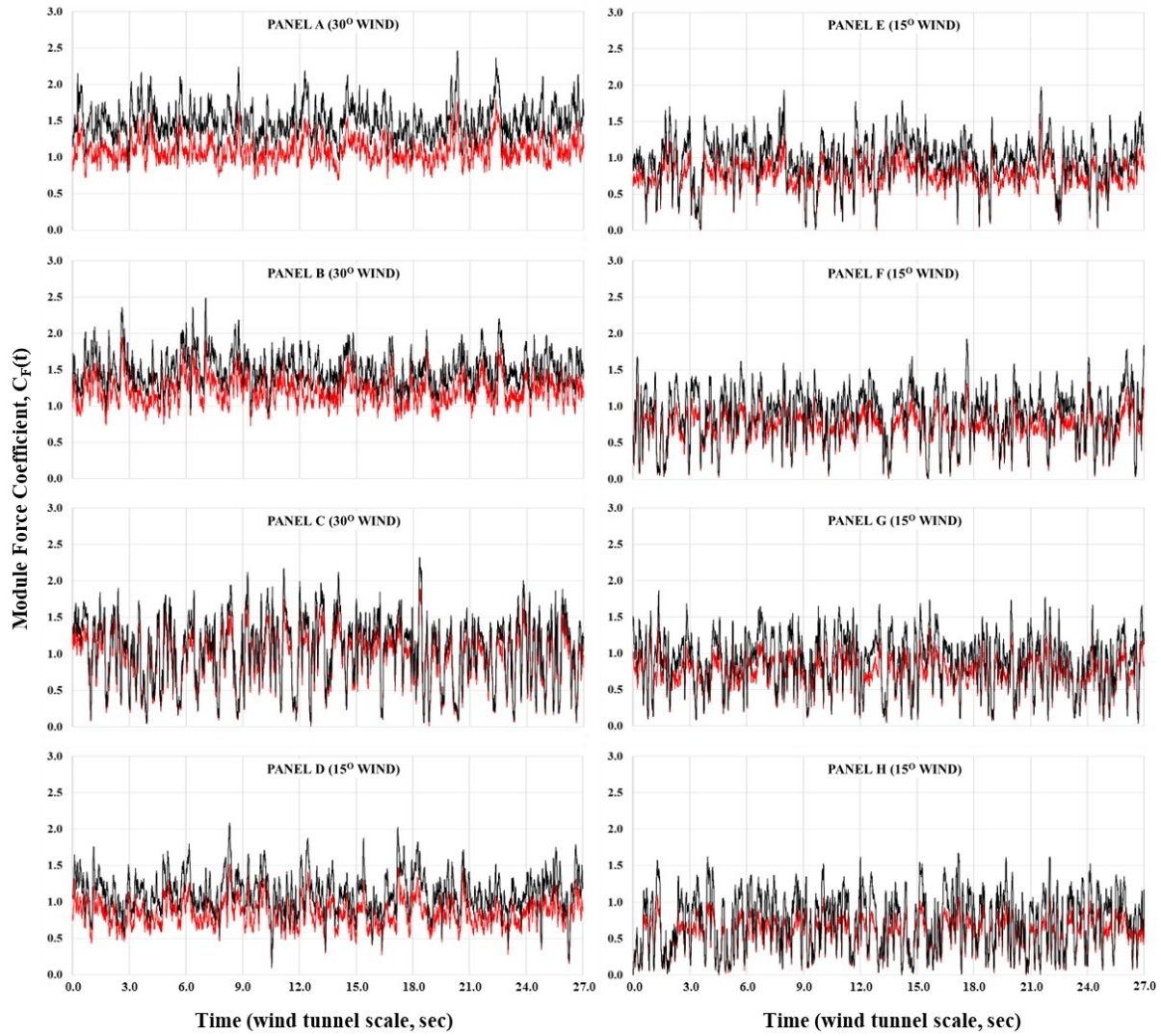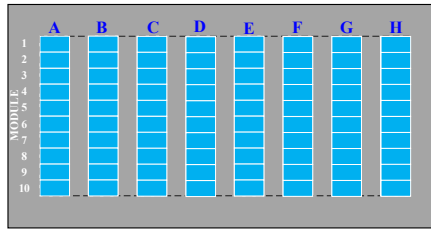
Figure 7.12 Time histories of module force coefficients for array-edge modules (M1)

array, presented in Figure 7.12, show that the module force coefficients obtained at pressure taps coverage at Conf. 5 and Conf. 6 are of a similar shape substantially; but demonstrably, the amplitudes of high positive "spikes" are lowered when considering one line of pressure taps on the lower surface, and hence, the resulted force coefficients are not as intensive as those obtained with identical taps distribution.

It should be noted that the records selected are of module maximum positive peak force coefficients provided in Figure 7.11 corresponding to the effective area of 2.0 m^2. Certainly, the downward translation of the amplitudes (i.e., shifts towards the negative y-axis) has been introduced into the records of the positive module force coefficients when considering on pressure tap at the center of the module as a result of excluding the regions of high positive net pressures (i.e., regions of high suction on the lower surface) and the high cross-correlation between the time history of the lower surface pressure at different regions in the chordwise direction.

As a result, the misalignment of the pressure taps on the panel surfaces by overlooking the lower surface regions close to the solar module edges significantly underestimated the worst mean and peak force coefficients of the downward net pressures, as these regions have experienced peak surface suction at the most critical wind direction found to be in the range of 1.3-1.6 larger than the corresponding suction of regions located in the middle of the solar module.

Finally, it is demonstrated that the pressure taps coverage on the upper and lower surface is critical for reliable, economic, and safe estimation of the net pressure across the solar panel; thus, their proper implementation and distribution shall be ensured during the experimental setup.

CHAPTER 8 TOWARD BETTER MODELING IN WIND TUNNELS FOR CODIFICATION STUDIES

In this chapter, the issues addressed in the current research have been dealt with separately, where sections 8.1, 8.2, and 8.3 are dedicated to discussing the results related to enlarging the geometric test scaling, air clearance underneath the solar array, and the pressure taps coverage, respectively. In each section, specific recommendations are established and provided for remedying the design provisions of the current wind codes and standards and for better simulation of solar panels in atmospheric wind tunnels for codification and design-oriented studies.

A portion of the work presented in this chapter has been published in the Journal of Wind Engineering and Industrial Aerodynamics (Alrawashdeh and Stathopoulos, 2020) and the Journal of Structural Engineering (Alrawashdeh and Stathopoulos, 2022b) and presented at several conferences (Alrawashdeh and Stathopoulos, 2019a, 2019b, 2022a, 2022c).

8.1 Geometric Scale

It is increasingly evident that enlarging the geometric scaling of the test model of rooftop solar panels would disturb the experimental results. Moreover, the fact that testing solar panels at the correct scale in standard open-country exposure is an end that could not be rightfully satisfied in the wind tunnel at the desired modeling flexibility. The accurate answer to the present issue will obviously call for models tested at various scales to perceive the variations which are recognized as a random trend spatially. Particularly, when it comes to underestimated trends in the magnitude of the wind-tunnel design force coefficients, i.e., the critical positive and negative peak force coefficients developed at oblique wind directions, the influence of enlarging the geometric test

scale shall not be understated. Therefore, a correction methodology is imperative to enhance the reliability and credibility of the wind tunnel results produced at relaxed geometric test scale.

For the considered geometric test scaling, Figures 8.1 and 8.2 present the distribution of local extreme positive and negative peak force coefficients along the center of the panels in the spanwise direction, respectively. The extreme positive and negative peak force coefficients are the envelope values of the data provided and discussed in Figures 5.8-5.10 and Figures 5.11-5.13, respectively.

A categorized rectification factors to account for the extreme force coefficients depending on the module location are proposed to address the impact of relaxing the geometric test scaling, as presented in Figure 8.3. The proposed rectification factors are recommended for multi-panels array inclined on flat or nearly flat roofs, where their design loads obtained by wind tunnel model size enlarged in the order of two and half to ten times the accurate size, provided that the wind-tunnel boundary flow fully duplicates the boundary field flow characteristics, namely flow roughness length (z_0), boundary layer depth (Z_g), and streamwise turbulence parameters (integral scale, intensity, and power spectra).

As illustrated in Figure 8.3, the modules of the array have been zoned into different groups associated with rectification factors, namely: modules in the front, the inner, and the edge and back of the array for positive loading; and modules in the front and inner, the edge, and the back of the array for negative loading. The groups of the array modules were created to reflect the topology of the extreme peak force coefficients, shown in Figures 8.1 and 8.2, along with their decreasing tendencies against the relative length scale of the simulated flow $(L_{u,x}/H)$.

As an illustrative example of the selection of the rectification factor, consider the extreme positive peak force coefficients of modules located in the front of the array (i.e., modules of panel A in Figure 8.1) which show decreasing tendencies with enlarging the geometric scale; this is indicative
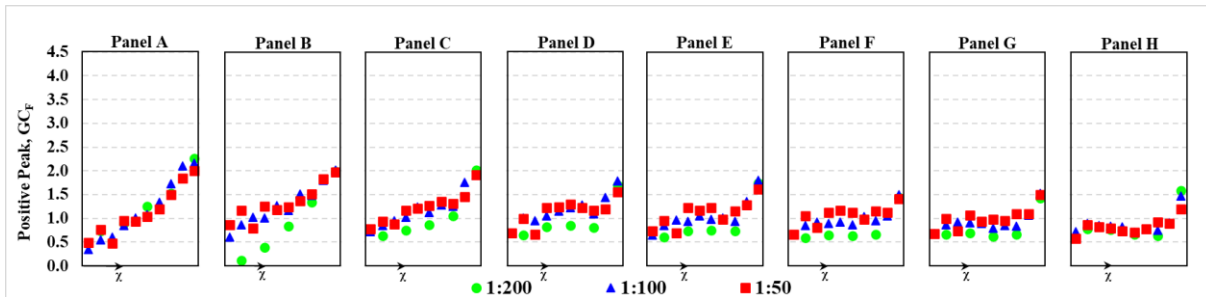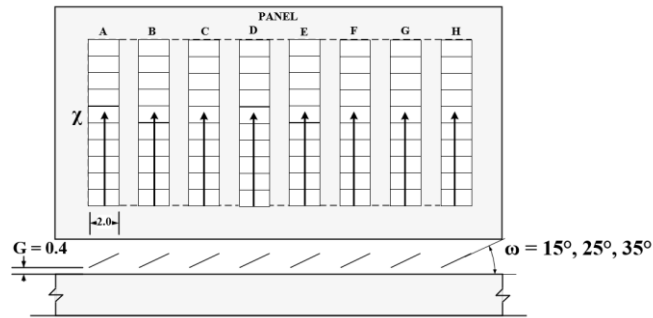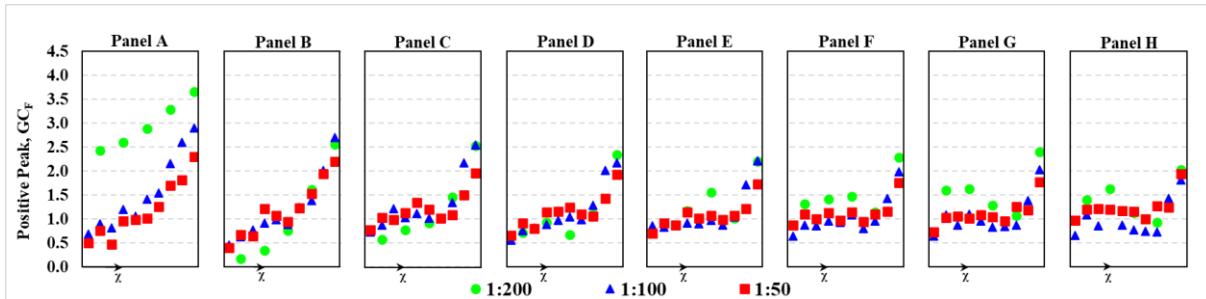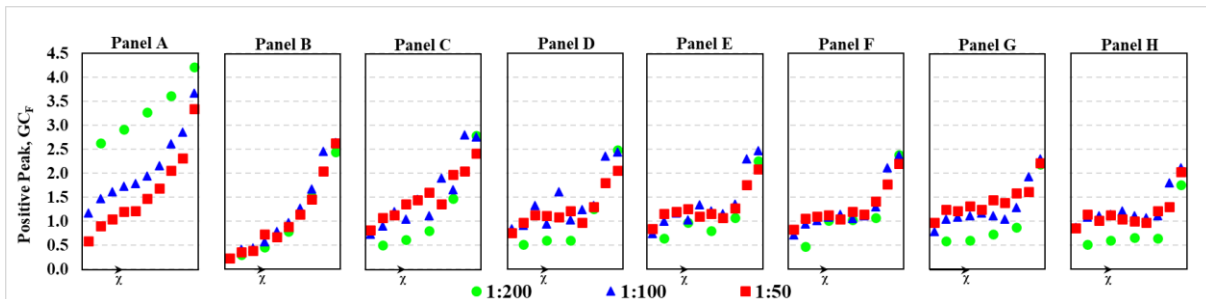
Figure 8.1 Effect of model scaling on extreme positive local peak force coefficients, envelope GC_F, of solar array at inclination, ω, of: (a) 15°, (b) 25°, and (c) 35°
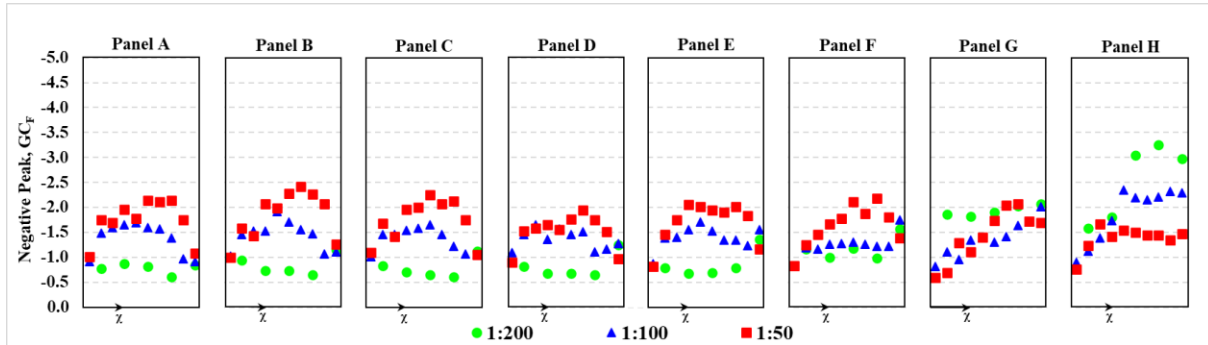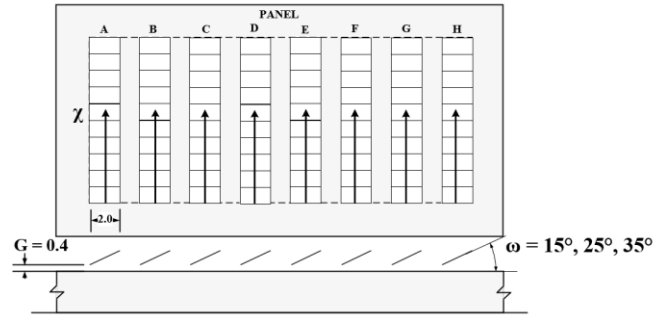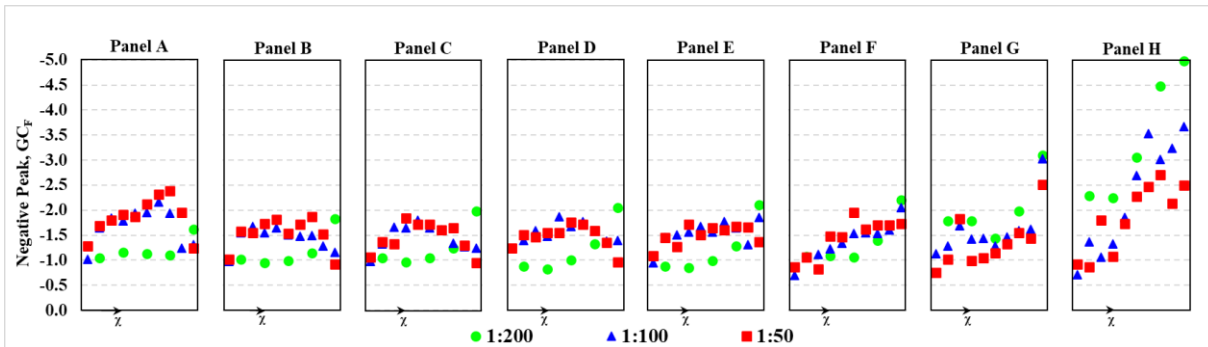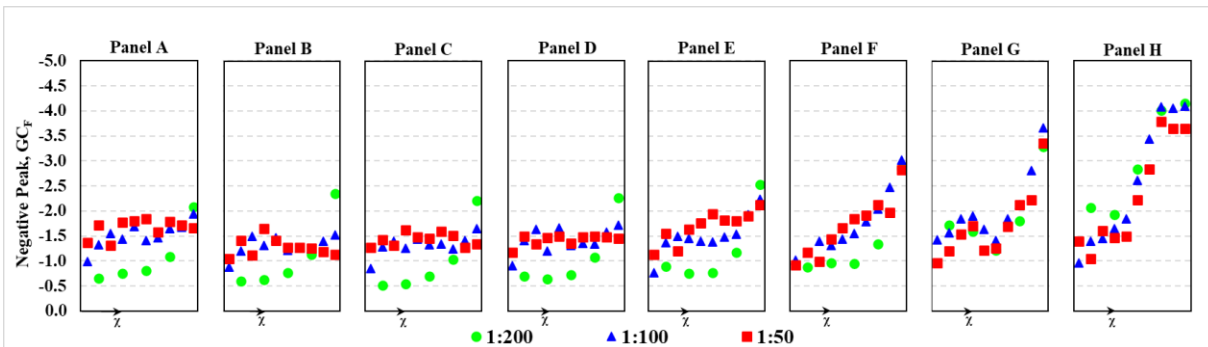
Figure 8.2 Effect of model scaling on extreme negative local peak force coefficients, envelope GC_F, of solar array at inclination, ω, of: (a) 15°, (b) 25°, and (c) 35°

For roof-mounted solar panels tested in an atmospheric boundary layer wind tunnel utilizing models of ten times the right size or less $(0.1 \leq L_{u,x}/H \leq 1.0)$:

Module location and Associated Rectification Factor:	
Front	3.5
Inner	1.6
Edge and back	1.4

Front and inner	1.8
Edge	2.2
Back	2.6
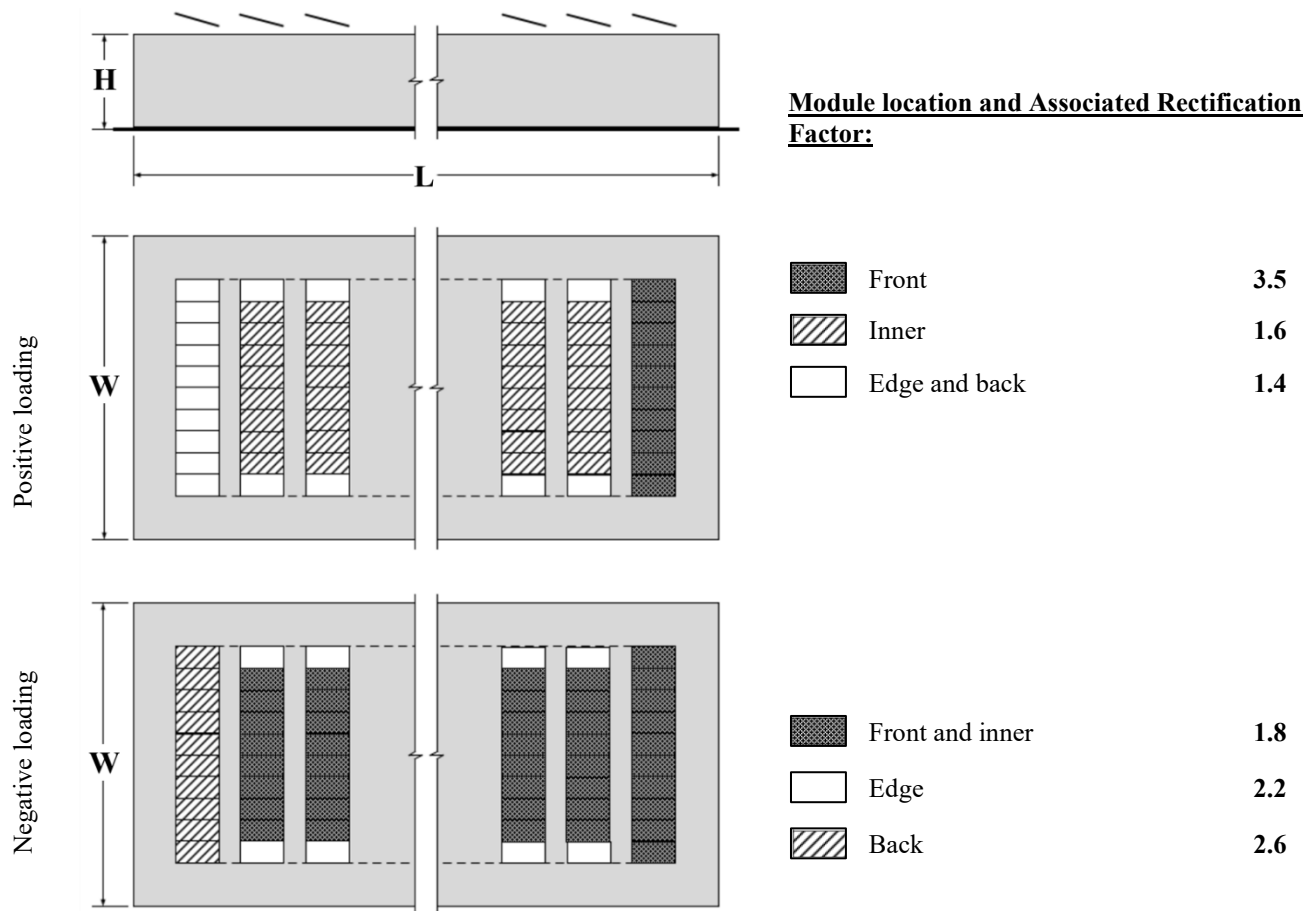
Figure 8.3 Rectification factors for extreme peak net pressure coefficients

that the results of the right scale would be higher, and an amplification factor must be applied to the results of these modules. A conservative approach is followed by examining the values of the ratios of the extreme positive peak module force coefficients of 1:50 to 1:200, 1:50 to 1:100, and 1:100 to 1:200 and selecting whichever is greater as a rectification factor. In all cases, the rectified results will be similar to those of 1:200 or greater, which are of course still higher than the actual

values (results at the correct scale).

The devised rectification procedure of the present research, illustrated in Figure 8.3, provides a post-experiments results rectification procedure that would lend itself well for use in atmospheric wind tunnel tests intended for generating design force coefficients and codification purposes. This approach not only serves to simplify the task of modeling structures that may often be impossible to scale down at the correct geometric ratio in the atmospheric flow of the standard open-country exposure. But also, it offers a reliable experimental technique, when applied no need to recourse to other simulation techniques such as partial atmospheric boundary layer simulations that may lead to underestimating the turbulence parameters.

It should be noted that the recommended factors may not be applicable to the previous studies for the following reasons: (1) the results of the previous studies are not provided locally (i.e, location of the solar module within the array), and (2) most of the experiments of the previous studies were carried out in partial-depth flow simulation which does not meet the conditions of the application of the rectification factors. In addition, one of the main challenging issues in the research field under consideration is the lack of full-scale data. However, the proposed rectification factors may provide a suitable base for future studies in these directions.

8.2 Air Clearance Beneath the Solar Array

As stated previously, current national wind codes and standards commonly used in professional practice do not address the impact of array clearance on wind loading. The provisions adopted by SEAOC (2017), NBCC (2020), and ASCE/SEI 7 (2022) are applicable exclusively for solar panels installed at a clearance height of 60 cm or less ($G \leq 60$ cm) based on the premise that the air

clearance has no bearing within that limit. However, the formerly discussed results confirm that the underneath air clearance of the solar array presents different tendencies for the extreme force coefficients according to the direction of the net pressure (upward or downward).

As shown in Figures 8.40 and 8.50, the experimental results of the extreme negative and positive peak force coefficients are compared against the corresponding design force coefficients prescribed by NBCC (2020) and ASCE/SEI 7 (2022). It should be noted that the experimental results of these figures were not modified by the post-experiments rectification procedure introduced in the previous section of the thesis. It is considered that the selection of the model geometric test scaling would not of considerable importance when the interest is to observe the variation of the results with the clearance height.

Although the experimental extreme positive area-averaged peak force coefficients differed with air clearance size, they were less than the design values prescribed by NBCC (2020) and ASCE/SEI 7 (2022). On the other hand, it is observed that the experimental extreme negative area-averaged peak force coefficients are underestimated, significantly at reduced clearance (G = 0.20 m) and at no clearance (G = 0). As clearly shown in Figure 8.5, the extreme negative area-averaged peak force coefficients of all solar panels at reduced air clearance (i.e., G = 0.20 m) were significantly greater than the recommended design values with a factor up to 1.5. In this regard, it is recommended to review the scope of application of the current provisions to the rooftop solar array clearance off the roofs to ensure their compliance with the solar panels installed at a height of 40 cm or less above the roof.

The scope of application of the current guidelines identified in NBCC (2020) and ASCE/SEI 7 (2022) has been reviewed to make the necessary adjustments to incorporate the effects of the air clearance between the solar array and the roof. It is found from the discussion of the impact of the
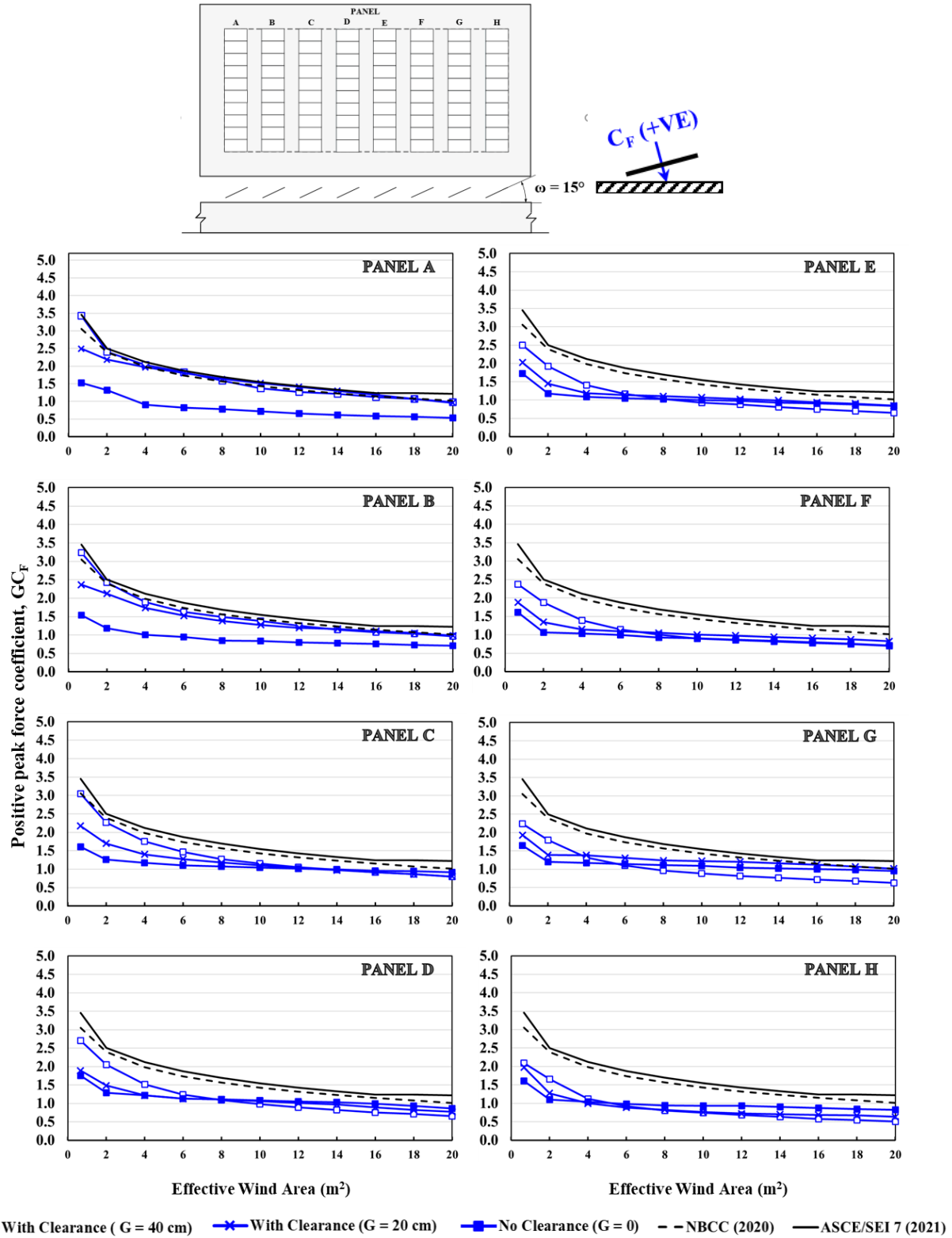
Figure 8.4 Effect of clearance on extreme positive area-averaged peak force coefficients,

envelope GC_F: Comparison with NBCC (2020) and ASCE/SEI 7 (2022)
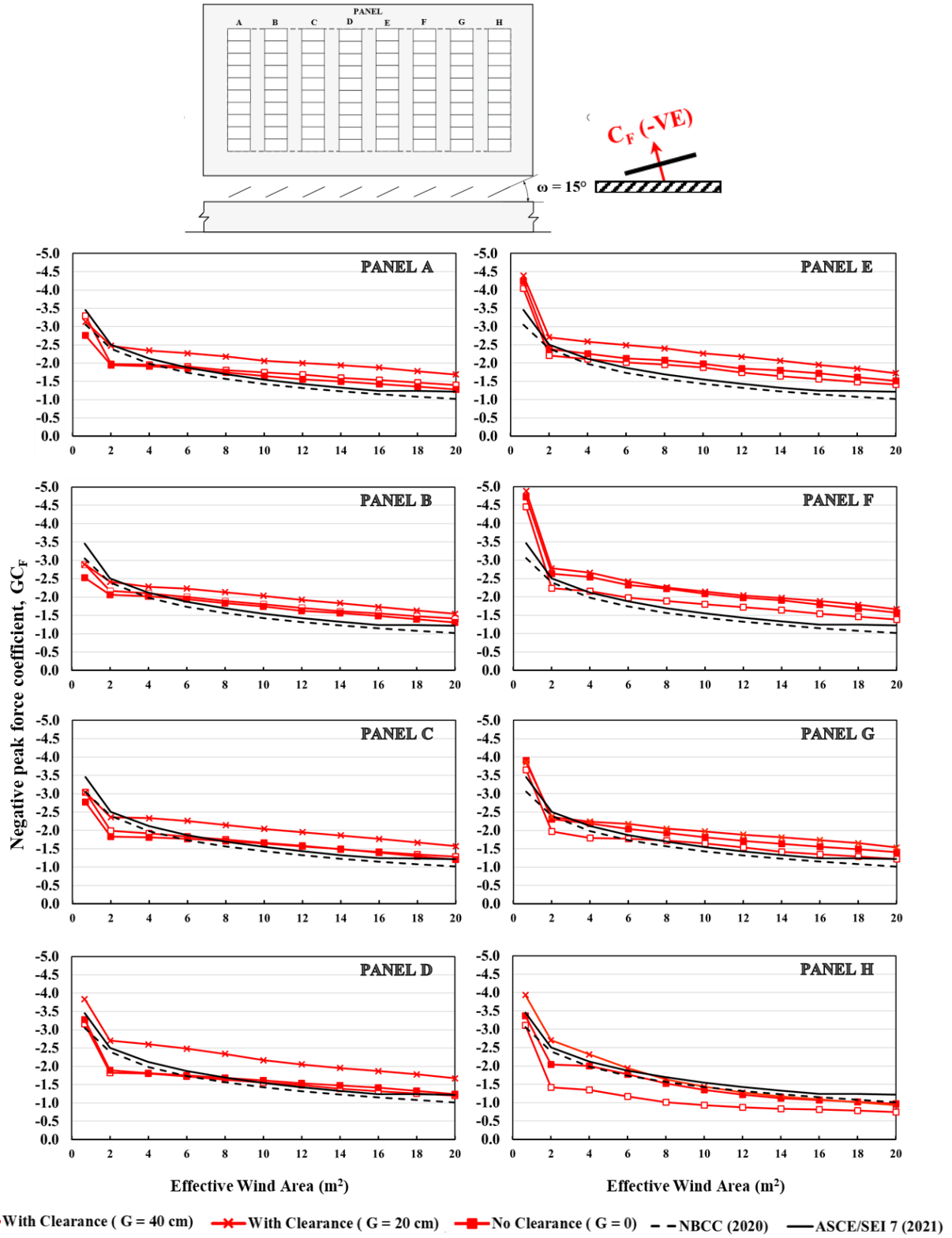
Figure 8.5 Effect of clearance on extreme negative area-averaged peak force coefficients, envelope GC$_F$: Comparison with NBCC (2020) and ASCE/SEI 7 (2022)

beneath air clearance on the extreme peak force coefficients that the rooftop solar panels at reduced clearance above the roof behaved like exposed panels (i.e., experienced higher upward net pressures). It would not be from a safety perspective to deal with solar panels under such aerodynamic conditions in the design as shielded (non-exposed); hence, an adjustment has been formulated and recommended for basically eliminating the application of the edge factor (γ_E) of value 1.0 for shielded (non-exposed) panels and considering it 1.5. Figure 8.6 presents the current scope of application of the current wind codes and standards with the proposed adjustments.

Clearly, the proposed adjustment can successfully enhance the safety of the current design guidelines for upward net pressure coefficients to accommodate the effects of the clearance on the upward net pressure coefficients. In applying the proposed adjustment, the extreme negative area-averaged peak force coefficients of ASCE/SEI 7 (2022) presented in Figure 8.5 will shift upward by 50% to envelope the experimental results.

To demonstrate the efficiency of the proposed exception to the current provisions, the experimental extreme area-averaged peak force pressure coefficients are compared with the modified provisions by applying the proposed exception. The comparison of the results (experimental, current, and rectified) is presented in Figure 8.7. It should be noted that the experimental GC_F values are the envelope from all wind directions, panels, and clearance heights. Furthermore, the application of the exception to the current provisions would enhance the harmonization between the different wind codes and standards of North America and Japan.

Current Provisions: NBCC (2020) and ASCE/SEI (2022)
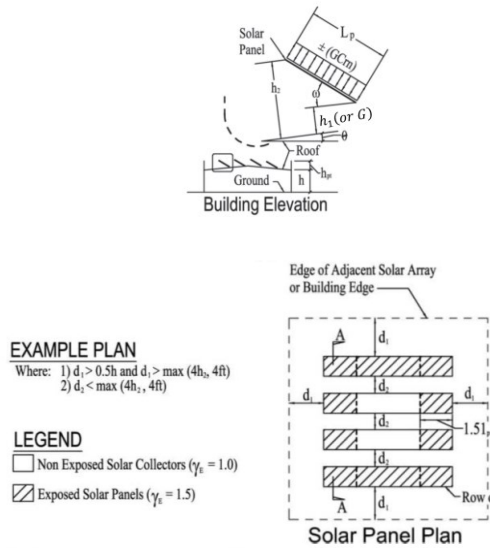
"the design wind pressure for rooftop solar panels apply to those located on enclosed or partially enclosed buildings of all heights with flat roofs, or with gable or hip roof slopes with θ ≤ 7°, with panels conforming to:

$$L_p \leq 2.04\ m$$
$$\omega \leq 35^o$$
$$G \leq 0.61\ m$$
$$h_2 \leq 1.22\ m$$"

"$\gamma_E = 1.5$ for uplift loads on panels that are exposed and within a distance $1.5L_p$ from the end of a row at an exposed edge of the array; $\gamma_E = 1.0$ elsewhere for uplift loads and for all downward loads. A panel is defined as exposed if d_1 to the roof edge > 0.5h and one of the following applies:

1. d_1 to the adjacent array > max($4h_2$, 1.2m)

or

2. d_2 to the next adjacent panel > max($4h_2$, 1.2m)."

Adjustment and Recommendations

- Solar panels installed at a height of 0.60 m or less ($G \leq 0.60\ m$) shall be considered exposed for the upward net pressures regardless of their location relative to other panels within the array, other neighboring arrays, and the building edge.

- For wind tunnel experiments utilized to generate the design net pressure coefficients, the correct handling of the solar array geometries shall include the size of the air clearance above the roof at a minimum possible blockage.

- For regions exposed to snow frequently, it is recommended to consider the excess of the wind-induced upward net pressure at the back panel of the array.

Figure 8.6 Adjustments and recommendations proposed to be added to current NBCC (2020)

and ASCE 7 (2022) for the effect of air clearance
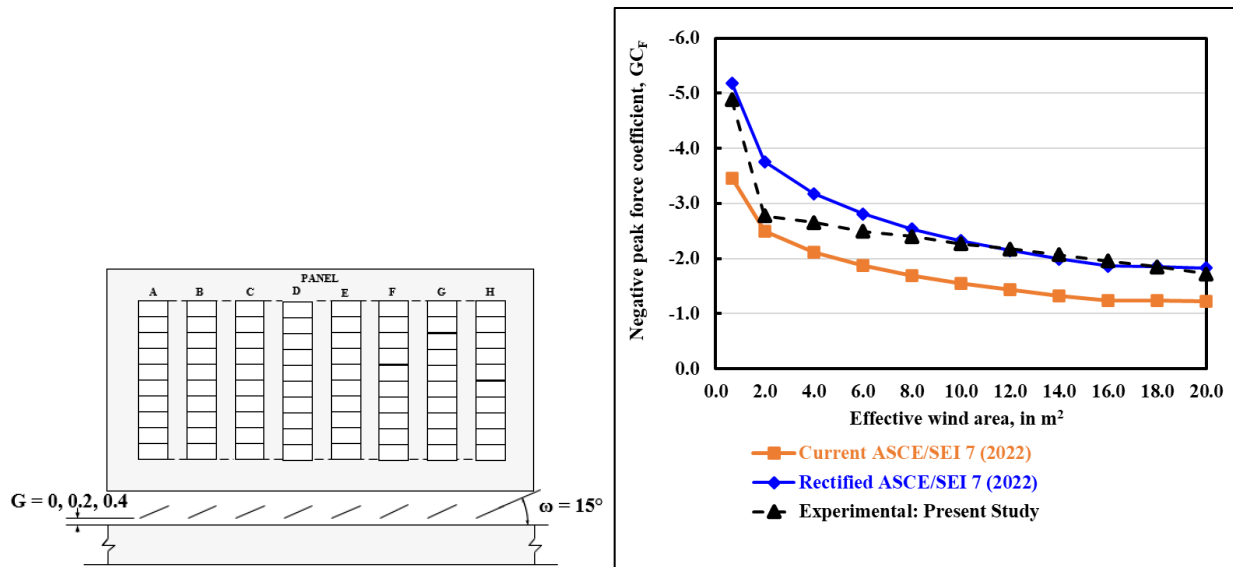
Figure 8.7 Extreme negative area-averaged peak force coefficients, envelope GC_F: Comparison with current ASCE/SEI (2022) and the proposed exception

8.3 Pressure Taps Coverage

Previously, it has been found that the wind-induced pressures on the surfaces of the solar panels asynchronously degrade in the chordwise direction depending on the wind direction. Thus, at critical wind directions for wind-induced suction on the upper surface, the wind suction degradation on the upper surface is subtle, and the same is true for the wind directions critical for wind suction on the lower surface. Furthermore, the distribution of the surface and net pressures at critical wind directions reveals, upon examination, crucial character of the pressure taps coverage with respect to their effects on experimental data, especially for the design-oriented results. Therefore, pressure taps coverage on the upper and lower surface is critical for reliable, economic, and safe estimation of the net pressure across the panel. In that spirit, a statement of guidance on proper handling of the pressure taps coverage is established.

142

Guidance Statement for Pressure Taps Coverage:

For atmospheric wind tunnel studies oriented toward generating the design net pressure coefficients and wind loading codification, the coverage of the pressure taps shall be properly handled, including taps locations, density, and alignment on the panel surfaces, as follows:

• At least three pressure taps per PV module surface shall be implemented in the chordwise direction, as close as possible to the middle and the edges of the solar panel.

• If the above coverage is not feasible, then two pressure taps per solar module would be equipped on each surface in regions close to the panel edges in the chordwise directions.

The first point of the Guidance Statement indicates the least coverage of pressure taps required to capture the severe net pressure at critical regions and the net pressure degradation over the module for the interest of the local and area-averaged net pressure coefficients. The pressure tap coverage proposed by the second point would be the minimum since it may account only for the critical regions of severe upward and downward net pressures (i.e., the edges of the PV module). It should be emphasized that the alignment of the pressure taps on the PV module surfaces shall be maintained, otherwise the pressure tap coverage may lead to underestimating the extreme upward and downward peak area-averaged net pressure coefficients.

CHAPTER 9 CONCLUSIONS AND RECOMMENDATION

8.1 Conclusions

This study concisely discussed the knowledge available on wind loads on solar panels mounted on flat roofs and pointed out the disagreement over the results of past studies in this area. Several tests were carried out on models of solar panels mounted on flat roofs at geometric scales of 1:200, 1:100, and 1:50 in a fully developed atmospheric flow of open-country exposure to investigate the impact of enlarging the geometric scale of the test model, air clearance underneath the array, and pressure taps coverage.

1. The present study corroborates that the broad spectrum of experimental practices in modeling solar panels in atmospheric wind tunnels may in part reflect the lack of procedural regularity that may contribute to the discrepancy of experimental findings in the research field under consideration. Unquestionably, such acts had implications for the codification of wind loads on rooftop solar panels.

2. At enlarging the wind tunnel model size:

    2.1 The flow pattern developed around the array and the local flow interaction with the panels was disturbed. Clear evidence of these disturbing interferences can be seen through the mean and peak surface pressures induced on the panels' surfaces.

    2.2 Surface pressures dominated by local flow generated at the panels' tips (i.e., modules are not within the large-scale separation bubble or large-scale conical vortices at the roof edges) show a decreasing tendency. Surface pressures of modules within the large separation bubble or conical vortices show dependence on the characteristics of the freestream flow,

particularly increasing tendency with enlarging the test model.

2.3 Minimal influence on the most critical wind direction.

2.4 Overvaluing and undervaluing tendencies of the force coefficients deemed as design values, depending on panel location, including negative and positive peak force coefficients induced at critical wind directions with variations by a factor up to 3.5.

3. Air clearance beneath the solar array

3.1 Varying the air clearance size may twist the flow-array interaction out of shape and may affect the local phenomena responsible for producing high suctions on the bottom surface, particularly like the wind interference of the solar panels. The wake region formulation is disturbed depending on the panel location and wind direction.

3.2 Varying the air clearance has implications on the mean and peak values of the surface and net pressures. Wind-induced pressure on the lower surface has been found to be the most sensitive to varying the air clearance for winds from 0° and 30°. Generally, the nearer the array is to the roof, the greater the upward net pressures and the lower the downward net pressures.

3.3 Condoning the air clearance during the experimental modeling setup is not appropriate practice, and hence, the correct handling of the solar array geometries shall include size of the air clearance above the roof at a minimum possible blockage.

3.4 There is a risk that in the event of snow accumulation around the solar panels the wind may become more severe on the back and middle panels. For regions exposed to snow frequently, it is recommended to consider the excess of the wind-induced pressure at these panels of the array.

4. Pressure taps coverage

   4.1 The wind pressures of the panels' upper surfaces exhibit high degradation markedly in the chordwise direction with relatively low cross-correlation, in particular at unfavorable wind directions (i.e., 120°-150°). On the contrary, the wind pressures of the panels' lower surfaces have a little degradation over most panels in both directions spanwise and chordwise – except for critical modules (i.e., windward modules at the array edge) at unfavorable wind directions, high degradation is observed.

   4.2 At wind directions unfavorable for upward and downward net pressures (i.e., 15°-45° and 120°-165°), the net pressures are of higher degradation in the chordwise direction, where degradation of the net pressure across the panel edges resulted in pressure regions characterized by the vast disparity in magnitude of a factor about 3.0.

   4.3 The comparison exercises made in this study through considering various pressure taps configurations show possible misleading results could be achieved when utilizing models of rooftop solar panels equipped with poorly conceived coverage of pressure taps. The proper coverage of pressure taps shall entail adequate density, arrangement, and alignment on the surfaces of the solar panel model.

5. Rules of procedure have been formulated and proposed to address the methodological challenges, limitations, as well as reliability and validity of the experimental results – concerning:

   5.1 Enlarged geometric scale: A post-experiments results rectification procedure along with indication for simulation requirements that shall be adopted for testing solar panels in

atmospheric wind tunnels.

5.2 Air clearance beneath the solar array: An adjustment for the application of the edge factor of NBCC (2020) and ASCE/SEI (2022) for shielded solar panels installed at a height of 0.60 m or less above the roof.

5.3 Pressure taps coverage: A statement of guidance for the proper implementation of the pressure taps on the surfaces of the solar panels.

Finally, it is important to sensitize the code and standards committees to research issues that may be critical to be addressed in the codification process, considering of course the inherent error associated with such modeling practices. It is highly recommended that the above rules be applied to the wind tunnel modeling setup intended particularly for codification studies for accurately conducting wind tunnel testing of roof-mounted solar panels

8.2 Recommendations for Further Work

The findings of the present thesis are promising and would provide a base for future studies. The author recommends further research in the field of rooftop solar panels should be carried out in the following directions:

- **Atmospheric Wind Tunnel Studies:** More wind tunnel studies oriented for codification purpose to generate the design wind pressure coefficients are needed. Geometric parameters, including inter-panels spacing, building height, roof dimensions, panels number, shall be accounted.

- **Computational studies:** CFD simulations are very useful for better understanding and visualizing the development and interaction of the flow with the rooftop solar panels.

- **Field (full-scale) studies:** This is a crucial area of emphasis for the evaluation of design wind loading for rooftop solar panel systems. Full-scale measurements always have a considerable interest for their importance in validating the experimental (wind tunnel) and computational (CFD) results. In the case of rooftop solar panels, the full-scale measurements assume paramount importance since they are extremely limited unless not explicitly available in the literature.

REFERENCES

Alberta Infrastructure, 2017. Solar photovoltaic guidelines: Planning and installation for Alberta infrastructure projects. https://www.alberta.ca/assets/documents/tr/tr-solarpvguide.pdf

Alrawashdeh, H., 2015. Wind pressures on flat roof edges and corners of large low buildings. Master's Thesis, Concordia University, Montreal, Canada.

Alrawashdeh, H., Stathopoulos, T., 2015. Wind pressures on large roofs of low buildings and wind codes and standards. Journal of Wind Engineering and Industrial Aerodynamics 147, 212–225. https://doi.org/10.1016/j.jweia.2015.09.014

Alrawashdeh H., Stathopoulos T., 2017. Wind effects on roof-mounted solar panels. Proceedings of the 2nd Coordinating Engineering for Sustainability and Resilience (CESARE'17), May 3-8, Amman, Jordan.

Alrawashdeh H., Stathopoulos T., 2018. A critical review of wind load provisions for solar panel design. Presented in Structures Congress Conference, ASCE, April 19-21, Fort Worth, Texas, USA.

Alrawashdeh H., Stathopoulos T., 2019a. Wind loads on solar panels mounted on flat roofs: Effect of geometric scale. Proceedings of the 15th International Conference on Wind Engineering, September 1-6, Beijing, China.

Alrawashdeh H., Stathopoulos T., 2019b. Reliable evaluation of wind loads on roof-mounted solar panels using wind-tunnel models. Proceedings of the 27th Canadian Congress of Applied Mechanics (27th CANCAM), May 27-30, Sherbrooke, Quebec, Canada.

Alrawashdeh, H., Stathopoulos, T., 2020. Wind loads on solar panels mounted on flat roofs: Effect of geometric scale. Journal of Wind Engineering and Industrial Aerodynamics 206,

104339. https://doi.org/10.1016/j.jweia.2020.104339

Alrawashdeh H., Stathopoulos T., 2022a. Critical considerations for modeling roof-mounted solar panels in atmospheric wind tunnels. Proceedings of the 3rd Coordinating Engineering for Sustainability and Resilience (CESARE'22), pp. 22-32, 6-9 May, Irbid, Jordan.

Alrawashdeh H., Stathopoulos T., 2022b. Experimental investigation of the wind loading on solar panels: effects of clearance off flat roofs. Journal of Structural Engineering (ASCE), 148 (12), 04022202 (1-18). https://doi.org/10.1061/JSENDH/STENG-10957

Alrawashdeh H., Stathopoulos T., 2022c. Testing rooftop solar panels in atmospheric wind tunnels: state-of-the-practice. Presented in the 14th Americas Conference on Wind Engineering, 17-19 May, Lubbock, Texas, USA.

Alrawashdeh H., Stathopoulos T., 2022d. Wind loading of rooftop PV panels cover plate: A codification-oriented study. Proceedings of the 8th European-African Conference on Wind Engineering, September 20-23, Bucharest, Romania.

Aly, A.M., 2016. On the evaluation of wind loads on solar panels: The scale issue. Solar Energy 135, 423–434. https://doi.org/10.1016/j.solener.2016.06.018

Aly, A.M., Bitsuamlak, G., 2014. Wind-induced pressures on solar panels mounted on residential homes. Journal of Architectural Engineering 20, 04013003. https://doi.org/10.1061/(ASCE)AE.1943-5568.0000132

Aly, A.M., Bitsuamlak, G., 2013. Aerodynamics of ground-mounted solar panels: Test model scale effects. Journal of Wind Engineering and Industrial Aerodynamics 123, 250–260. https://doi.org/10.1016/j.jweia.2013.07.007

ASCE/SEI 7, 2022. Minimum design loads and associated criteria for buildings and other structures. American Society of Civil Engineers, Reston, VA, USA.

https://doi.org/10.1061/9780784415788

ASCE/SEI 49, 2021. Wind tunnel testing for buildings and other structures. American Society of Civil Engineers, Reston, VA, USA. https://doi.org/10.1061/9780784415740

Banks, D., 2013. The role of corner vortices in dictating peak wind loads on tilted flat solar panels mounted on large, flat roofs. Journal of Wind Engineering and Industrial Aerodynamics 123, 192–201. https://doi.org/10.1016/j.jweia.2013.08.015

Browne, M.T.L., Gibbons, M.P.M., Gamble, S., Galsworthy, J., 2013. Wind loading on tilted roof-top solar arrays: The parapet effect. Journal of Wind Engineering and Industrial Aerodynamics 123, 202–213. https://doi.org/10.1016/j.jweia.2013.08.013

Candelario, J.D., Stathopoulos, T., Zisis, I., 2014. Wind loading on attached canopies: Codification study. Journal of Structural Engineering 140, 4014007. https://doi.org/10.1061/(ASCE)ST.1943-541X.0001007

Cao, J., Yoshida, A., Saha, P.K., Tamura, Y., 2013. Wind loading characteristics of solar arrays mounted on flat roofs. Journal of Wind Engineering and Industrial Aerodynamics 123, 214–225. https://doi.org/10.1016/j.jweia.2013.08.014

Chevalier, H., Norton, D., 1979. Wind loads on solar collector panels and support structure. Technical Report, Texas A and M University, Texas, USA. https://doi.org/10.2172/5350425

Durst, C.S., 1960. The statistical variation of wind with distance. Quarterly Journal of the Royal Meteorological Society 86, 543–549. https://doi.org/10.1002/qj.49708637012

Ginger, J., Payne, M., Stark, G., Sumant, B., Leitch, C., 2011. Investigations on wind loads applied to solar panels mounted on roofs. Cyclone Testing Station (Report No. TS821), School of Engineering and Physical Sciences, James Cook University, Townsville, Australia.

Hunt, A., 1982. Wind-tunnel measurements of surface pressures on cubic building models at several scales. Journal of Wind Engineering and Industrial Aerodynamics 10, 137–163. https://doi.org/10.1016/0167-6105(82)90061-7

JIS C 8955, 2017. Load design guide on structures for photovoltaic array. Japanese Standards Association, Tokyo, Japan.

Kopp, G.A., 2014. Wind loads on low-profile, tilted, solar arrays placed on large, flat, low-rise building roofs. Journal of Structural Engineering 140, 04013057. https://doi.org/10.1061/(ASCE)ST.1943-541X.0000825

Kopp, G.A., Farquhar, S., Morrison, M.J., 2012. Aerodynamic mechanisms for wind loads on tilted, roof-mounted, solar arrays. Journal of Wind Engineering and Industrial Aerodynamics 111, 40–52. https://doi.org/10.1016/j.jweia.2012.08.004

Mooneghi, M., Irwin, P., Gan Chowdhury, A., 2016. Partial turbulence simulation method for predicting peak wind loads on small structures and building appurtenances. Journal of Wind Engineering and Industrial Aerodynamics 157, 47–62. https://doi.org/10.1016/J.JWEIA.2016.08.003

Naeiji, A., Raji, F., Zisis, I., 2017. Wind loads on residential scale rooftop photovoltaic panels. Journal of Wind Engineering and Industrial Aerodynamics 168, 228–246. https://doi.org/10.1016/j.jweia.2017.06.006

NBCC, 2020. National Building Code of Canada 2020. Canadian Commission on Building and Fire Codes, National Research Council of Canada, Ottawa, Canada.

PV Magazine, 2018. In case of hurricane, apply Enphase, tighten bolts and mind your wind codes! https://pv-magazine-usa.com/2018/11/29/in-case-of-hurricane-apply-enphase-and-mind-your-wind-codes/

Rabinovitch, J., 2019. Design guide for rooftop solar. RJC Engineers Firm. https://www.rjc.ca/rjc-media/research/design-guide-for-rooftop-solar.html

Radu, A., Axinte, E., 1989. Wind forces on structures supporting solar collectors. Journal of Wind Engineering and Industrial Aerodynamics 32, 93–100. https://doi.org/10.1016/0167-6105(89)90020-2

Radu, A., Axinte, E., Theohari, C., 1986. Steady wind pressures on solar collectors on flat-roofed buildings. Journal of Wind Engineering and Industrial Aerodynamics 23, 249–258. https://doi.org/10.1016/0167-6105(86)90046-2

Saathoff, P.J., Stathopoulos, T., 1992. Wind loads on buildings with sawtooth roofs. Journal of Structural Engineering 118, 429–446. https://doi.org/10.1061/(ASCE)0733-9445(1992)118:2(429)

SEAOC, 2012. Report SEAOC PV2-2012: Wind design for solar photovoltaic arrays on flat roofs. SEAOC Solar Photovoltaic Systems Committee, Structural Engineers Association of California, Sacramento, CA, USA.

SEAOC, 2017. Report SEAOC PV2-2017: Wind design for solar arrays. SEAOC Solar Photovoltaic Systems Committee, Structural Engineers Association of California, Sacramento, CA, USA.

Stathopoulos, T., 1984. Design and fabrication of a wind tunnel for building aerodynamics. Journal of Wind Engineering and Industrial Aerodynamics 16, 361–376. https://doi.org/10.1016/0167-6105(84)90018-7

Stathopoulos, T., Dumitrescu-Brulotte, M., 1989. Design recommendations for wind loading on buildings of intermediate height. Canadian Journal of Civil Engineering 16, 910–916. https://doi.org/10.1139/L89-134

Stathopoulos, T., Elsharawy, M., Galal, K., 2013. Wind load combinations including torsion for rectangular medium-rise building. International Journal of High-Rise Buildings 2(3), 245–255. https://doi.org/10.21022/IJHRB.2013.2.3.245

Stathopoulos, T., Mohammadian, A.R., 1991. Modelling of wind pressures on monoslope roofs. Engineering Structures 13, 281–292. https://doi.org/10.1016/0141-0296(91)90039-F

Stathopoulos, T., Surry, D., 1983. Scale effects in wind tunnel testing of low buildings. Journal of Wind Engineering and Industrial Aerodynamics 13, 313–326. https://doi.org/10.1016/0167-6105(83)90152-6

Stathopoulos, T., Wang, K., Wu, H., 2000. Proposed new Canadian wind provisions for the design of gable roofs. Canadian Journal of Civil Engineering 27, 1059–1072. https://doi.org/10.1139/l00-023

Stathopoulos, T., Zisis, I., Xypnitou, E., 2014. Local and overall wind pressure and force coefficients for solar panels. Journal of Wind Engineering and Industrial Aerodynamics 125, 195–206. https://doi.org/10.1016/j.jweia.2013.12.007

Stenabaugh, S.E., Karava, P., Kopp, G.A., 2010. Design Wind Loads for Photovoltaic Systems on Sloped Roofs of Residential Buildings. Boundary Layer Wind Tunnel (Report BLWT 4–2010), London, ON, Canada.

Stenabaugh, S.E., Iida, Y., Kopp, G.A., Karava, P., 2015. Wind loads on photovoltaic arrays mounted parallel to sloped roofs on low-rise buildings. Journal of Wind Engineering and Industrial Aerodynamics 139, 16-26. https://doi.org/10.1016/j.jweia.2015.01.007.

Tieleman, H.W., Reinhold, T.A., Hajj, M.R., 1997. Importance of turbulence for the prediction of surface pressures on low-rise structures. Journal of Wind Engineering and Industrial Aerodynamics 69–71, 519–528. https://doi.org/10.1016/S0167-6105(97)00182-7

Wang, J., van Phuc, P., Yang, Q., Tamura, Y., 2020a. LES study of wind pressure and flow characteristics of flat-roof-mounted solar arrays. Journal of Wind Engineering and Industrial Aerodynamics 198, 104096. https://doi.org/10.1016/j.jweia.2020.104096

Wang, J., Yang, Q., Tamura, Y., 2018. Effects of building parameters on wind loads on flat-roof-mounted solar arrays. Journal of Wind Engineering and Industrial Aerodynamics 174, 210–224. https://doi.org/10.1016/j.jweia.2017.12.023

Wang, J., Yang, Q., van Phuc, P., Tamura, Y., 2020b. Characteristics of conical vortices and their effects on wind pressures on flat-roof-mounted solar arrays by LES. Journal of Wind Engineering and Industrial Aerodynamics 200, 104146. https://doi.org/10.1016/j.jweia.2020.104146

Wood, G.S., Denoon, R.O., Kwok, K.C.S., 2001. Wind loads on industrial solar panel arrays and supporting roof structure. Wind and Structures, An International Journal 4, 481–494. https://doi.org/10.12989/was.2001.4.6.481

Appendix A

Figures from wind codes and standards

Appendix A-1: Design wind loads for rooftop solar panels for enclosed and partially enclosed buildings in ASCE/SEI 7 (2022)

Appendix A-2: Illustration of exposed (end) and shielded (central) modules in a rooftop array in JIS C 8955 (2017)

Appendix A-1: Design wind loads for rooftop solar panels for enclosed and partially enclosed

buildings in ASCE/SEI 7 (2022)

W_L

2h   2h

2h   ③   ②   ③

W_S ②   ①   ②

2h   ③   ②   ③

Building Roof Plan

Solar Panel L_p

$\pm (GC_m)$

h_2 ω

h_1

θ

Roof

Ground h h_{pt}

Building Elevation

Nominal Net Pressure Coefficients $(GC_{rn})_{nom}$

Nominal Net Pressure Coefficient (GC rm) nom

③   ②   ①

0.5
0.45
0.35

0.15
0.10

Normalized Wind Area, A
$0° \le \omega \le 5°$

Nominal Net Pressure Coefficient (GC rm) nom

③   ②   ①

0.8
0.65
0.56

0.5
0.4
0.3

Normalized Wind Area, A
$15° \le \omega \le 35°$
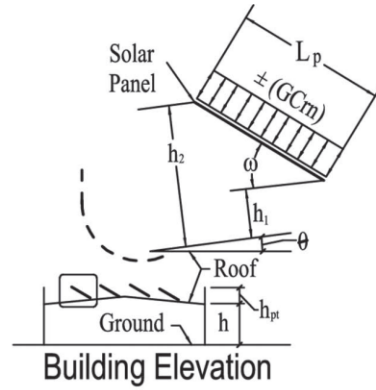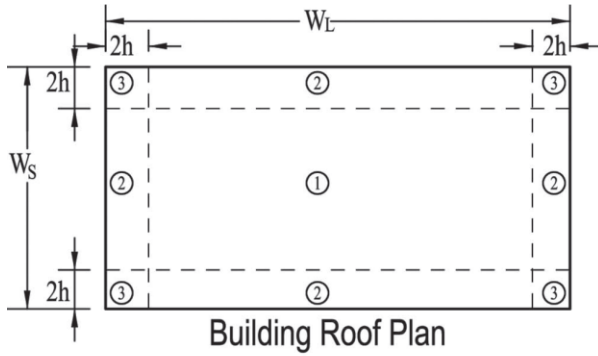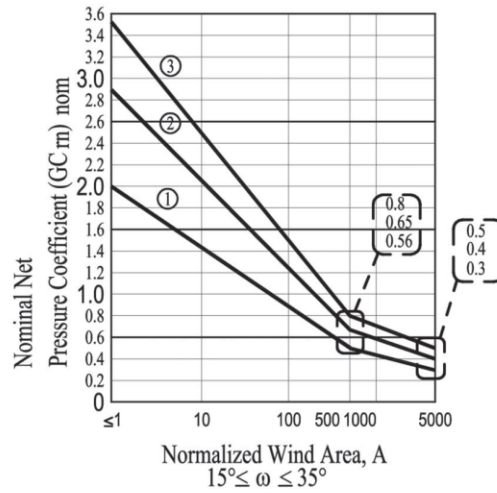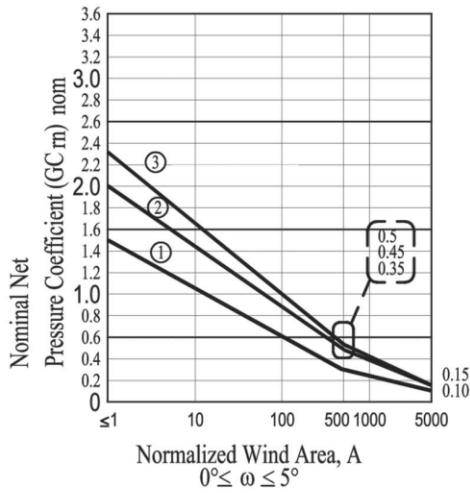
Array Edge Factors, γ_E

EXAMPLE PLAN

Where: 1) $d_1 > 0.5h$ and $d_1 > \max (4h_2, 4ft)$
        2) $d_2 < \max (4h_2, 4ft)$

LEGEND

☐ Non Exposed Solar Collectors ($\gamma_E = 1.0$)

▨ Exposed Solar Panels ($\gamma_E = 1.5$)

Solar Panel   Roof

Section A-A

Edge of Adjacent Solar Array
or Building Edge

NORTH

A d_1

d_2

d_1 d_1

d_2

$1.5 l_p$ typ

d_2

d_2

A d_1 Row of Solar Panels

Solar Panel Plan
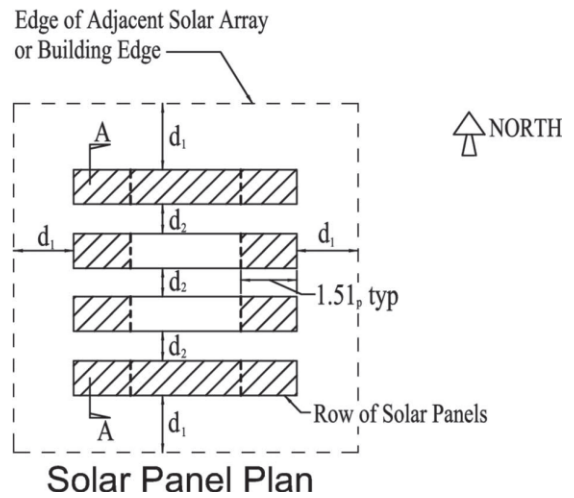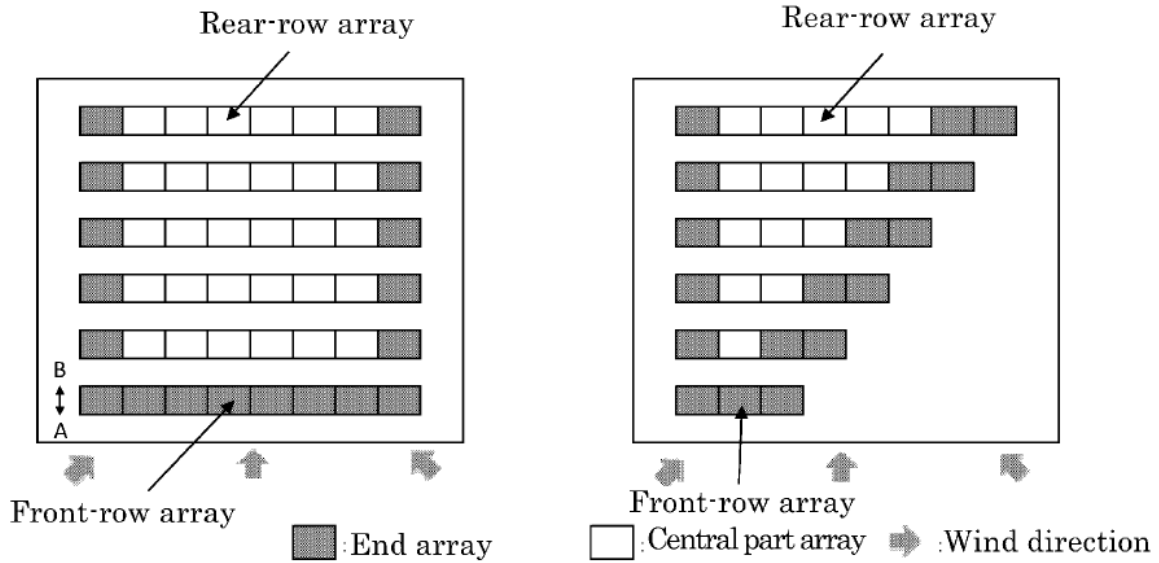
a) In the case of fair wind (positive pressure)
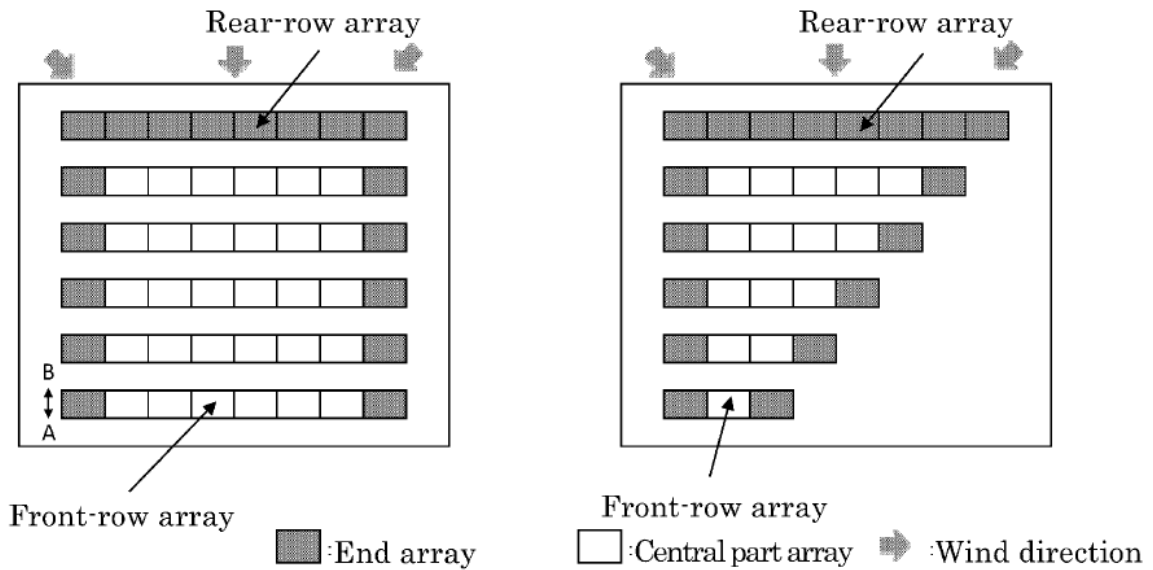
b) In the case of adverse wind (negative pressure)

Appendix B

Local extreme positive mean and peak force coefficients and the corresponding most critical wind direction for the solar array with a tilt angle ω = 15° at model scales of 1:200, 1:100, and 1:50

Appendix B-1: Local positive mean

Appendix B-2: Local negative mean

Appendix B-3: Local positive peak

Appendix B-4: Local negative peak

Appendix B-1: Extreme local positive mean force coefficient and the corresponding most critical

wind direction

C_F -0.2   ...   -1.2

Force coefficients

1:200

Row			
A	-0.3	-0.2	-0.3
B	-0.3	-0.2	-0.4
C	-0.2	-0.2	-0.5
D	-0.2	-0.3	-0.6
E	-0.2	-0.3	-0.6
F	-0.4	-0.4	-0.7
G	-0.8	-0.8	-1.0
H	-1.0	-1.2	-1.1

1:100

Row					
A	-0.7	-0.6	-0.5	-0.4	-0.5
B	-0.7	-0.7	-0.6	-0.5	-0.5
C	-0.6	-0.6	-0.5	-0.5	-0.6
D	-0.7	-0.5	-0.5	-0.5	-0.6
E	-0.7	-0.6	-0.5	-0.6	-0.8
F	-0.6	-0.5	-0.5	-0.5	-0.7
G	-0.3	-0.4	-0.4	-0.5	-0.7
H	-0.9	-0.7	-1.0	-0.8	-0.8

1:50

Row					
A	-1.2	-1.2	-1.1	-0.8	-0.6
B	-1.1	-1.3	-1.2	-0.9	-0.7
C	-1.1	-1.1	-1.1	-0.8	-0.6
D	-1.0	-1.0	-0.9	-0.8	-0.6
E	-1.1	-1.1	-1.0	-0.9	-0.7
F	-1.0	-1.2	-1.2	-0.9	-0.8
G	-1.0	-1.0	-1.0	-0.9	-0.9
H	-0.6	-0.5	-0.4	-0.4	-0.6

Critical wind directions

1:200

165	150	150
165	165	150
165	150	150
165	150	150
120	135	150
165	135	135
165	165	135
135	150	165

1:100

165	165	165	150	165
165	165	165	150	150
150	165	165	150	150
150	150	135	135	150
150	150	150	135	135
135	150	150	150	135
120	135	135	135	135
120	150	135	150	135

1:50

165	165	165	165	165
165	165	165	165	165
150	165	165	165	165
150	150	165	150	150
150	150	165	165	150
150	150	150	135	150
135	135	150	150	135
150	150	150	120	120

Wind direction reference: 0°, 15°, 30°, 45°, 60°, 75°, 90°, 105°, 120°, 135°, 150°, 165°, 180° (rows A–H)

Appendix B-3: Extreme local positive peak force coefficient and the corresponding most critical

wind direction

The figure shows GC$_F$ color scale from 0.6 to 2.3.

Top section — Extreme local positive peak force coefficients

1:200

A	1.2	1.5	2.3
B	0.9	1.3	2.0
C	0.9	1.1	2.0
D	0.8	0.8	1.7
E	0.7	0.7	1.7
F	0.7	0.7	1.4
G	0.6	0.7	1.4
H	0.7	0.6	1.6

1:100

A	1.1	1.3	1.7	2.1	2.2
B	1.2	1.5	1.6	1.8	2.0
C	1.1	1.3	1.3	1.8	1.9
D	1.2	1.3	1.1	1.4	1.8
E	1.0	1.0	0.9	1.4	1.8
F	0.9	1.0	1.0	1.1	1.5
G	0.8	0.9	0.8	1.1	1.5
H	0.7	0.8	0.8	0.9	1.5

1:50

A	1.1	1.3	1.5	1.8	2.0
B	1.3	1.4	1.5	1.8	2.0
C	1.3	1.4	1.3	1.5	1.9
D	1.3	1.2	1.1	1.2	1.6
E	1.2	1.0	1.2	1.3	1.6
F	1.1	1.0	1.2	1.1	1.4
G	1.0	1.0	1.1	1.1	1.5
H	0.7	0.8	0.9	0.9	1.2

Bottom section — Corresponding most critical wind direction

1:200

45	30	30
60	45	30
45	15	15
15	30	15
15	15	15
15	15	15
15	15	15
15	15	15

1:100

45	45	30	30	30
30	45	15	30	30
15	15	15	15	15
30	30	30	15	15
30	15	15	15	15
30	30	30	15	15
15	30	15	15	15
30	15	15	15	15

1:50

60	60	30	30	30
30	45	45	15	30
45	30	30	30	30
30	30	30	15	15
30	30	15	15	15
30	30	15	15	15
15	15	15	15	15
15	15	15	15	15

Wind direction diagram: 0°, 15°, 30°, 45°, 60°, 75°, 90°, 105°, 120°, 135°, 150°, 165°, 180° (with rows A B C D E F G H)

162

Appendix B-4: Extreme local negative peak force coefficient and the corresponding most critical

wind direction

GC$_F$ (scale: -0.6 to -3.3)

Extreme local negative peak force coefficient

	1:200			1:100					1:50				
A	-0.8	-0.8	-0.8	-1.6	-1.6	-1.4	-1.1	-1.2	-2.1	-2.1	-2.1	-1.8	-1.1
B	-0.7	-0.7	-1.2	-1.7	-1.6	-1.5	-1.1	-1.1	-2.3	-2.4	-2.3	-2.1	-1.3
C	-0.7	-0.6	-1.1	-1.7	-1.5	-1.2	-1.1	-1.0	-2.3	-2.1	-2.1	-1.7	-1.0
D	-0.7	-0.6	-1.2	-1.7	-1.5	-1.1	-1.2	-1.3	-1.8	-1.9	-1.7	-1.5	-1.0
E	-0.7	-0.8	-1.4	-1.5	-1.3	-1.3	-1.2	-1.6	-1.9	-1.9	-2.0	-1.8	-1.2
F	-1.2	-0.9	-1.6	-1.3	-1.3	-1.3	-1.2	-1.8	-1.4	-1.9	-1.8	-2.1	-2.2
G	-1.9	-2.0	-2.1	-1.8	-1.4	-1.6	-1.7	-2.3	-1.7	-2.0	-1.6	-1.8	-2.1
H	-3.1	-3.3	-3.0	-2.4	-2.2	-2.3	-2.3	-2.3	-1.5	-1.4	-1.4	-1.5	

Corresponding most critical wind direction

	1:200			1:100					1:50				
	165	180	135	165	165	165	150	135	165	165	165	165	165
	165	180	150	150	165	165	165	150	150	150	165	165	165
	150	180	135	150	165	165	135	135	150	150	165	165	150
	165	135	135	150	150	135	135	135	150	150	165	165	150
	150	135	135	135	150	150	135	135	135	135	150	165	150
	165	165	150	135	135	165	135	135	135	150	150	150	135
	150	165	135	150	150	150	150	120	135	135	135	120	150
	135	135	135	135	135	135	150	135	150	150	150	150	120

Wind direction key: 0°, 15°, 30°, 45°, 60°, 75°, 90°, 105°, 120°, 135°, 150°, 165°, 180°

Appendix C

Cross-correlation of the surface pressure coefficients in the chordwise direction for panels with
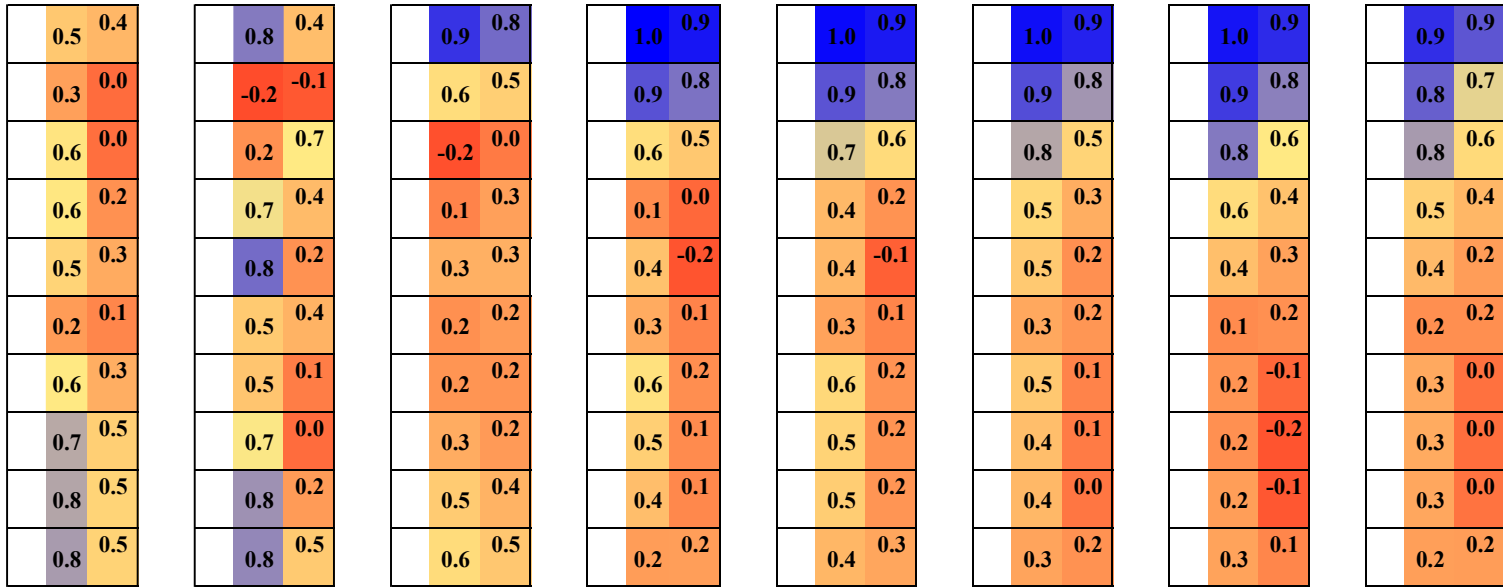
a tilt angle ω = 15°

Appendix C-1: Cross-correlation of the upper surface pressure coefficients at 30° wind direction

0.5	0.4	0.8	0.4	0.9	0.8	1.0	0.9	1.0	0.9	1.0	0.9	1.0	0.9	0.9	0.9
0.3	0.0	-0.2	-0.1	0.6	0.5	0.9	0.8	0.9	0.8	0.9	0.8	0.9	0.8	0.8	0.7
0.6	0.0	0.2	0.7	-0.2	0.0	0.6	0.5	0.7	0.6	0.8	0.5	0.8	0.6	0.8	0.6
0.6	0.2	0.7	0.4	0.1	0.3	0.1	0.0	0.4	0.2	0.5	0.3	0.6	0.4	0.5	0.4
0.5	0.3	0.8	0.2	0.3	0.3	0.4	-0.2	0.4	-0.1	0.5	0.2	0.4	0.3	0.4	0.2
0.2	0.1	0.5	0.4	0.2	0.2	0.3	0.1	0.3	0.1	0.3	0.2	0.1	0.2	0.2	0.2
0.6	0.3	0.5	0.1	0.2	0.2	0.6	0.2	0.6	0.2	0.5	0.1	0.2	-0.1	0.3	0.0
0.7	0.5	0.7	0.0	0.3	0.2	0.5	0.1	0.5	0.2	0.4	0.1	0.2	-0.2	0.3	0.0
0.8	0.5	0.8	0.2	0.5	0.4	0.4	0.1	0.5	0.2	0.4	0.0	0.2	-0.1	0.3	0.0
0.8	0.5	0.8	0.5	0.6	0.5	0.2	0.2	0.4	0.3	0.3	0.2	0.3	0.1	0.2	0.2
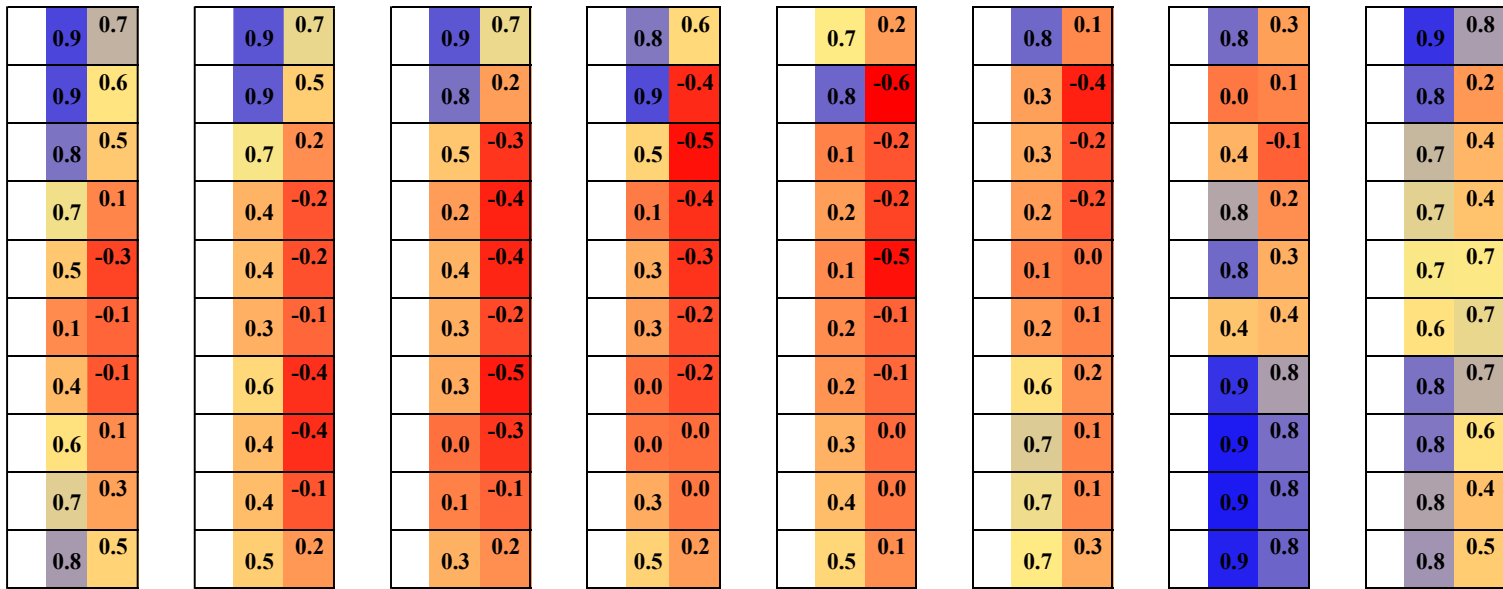
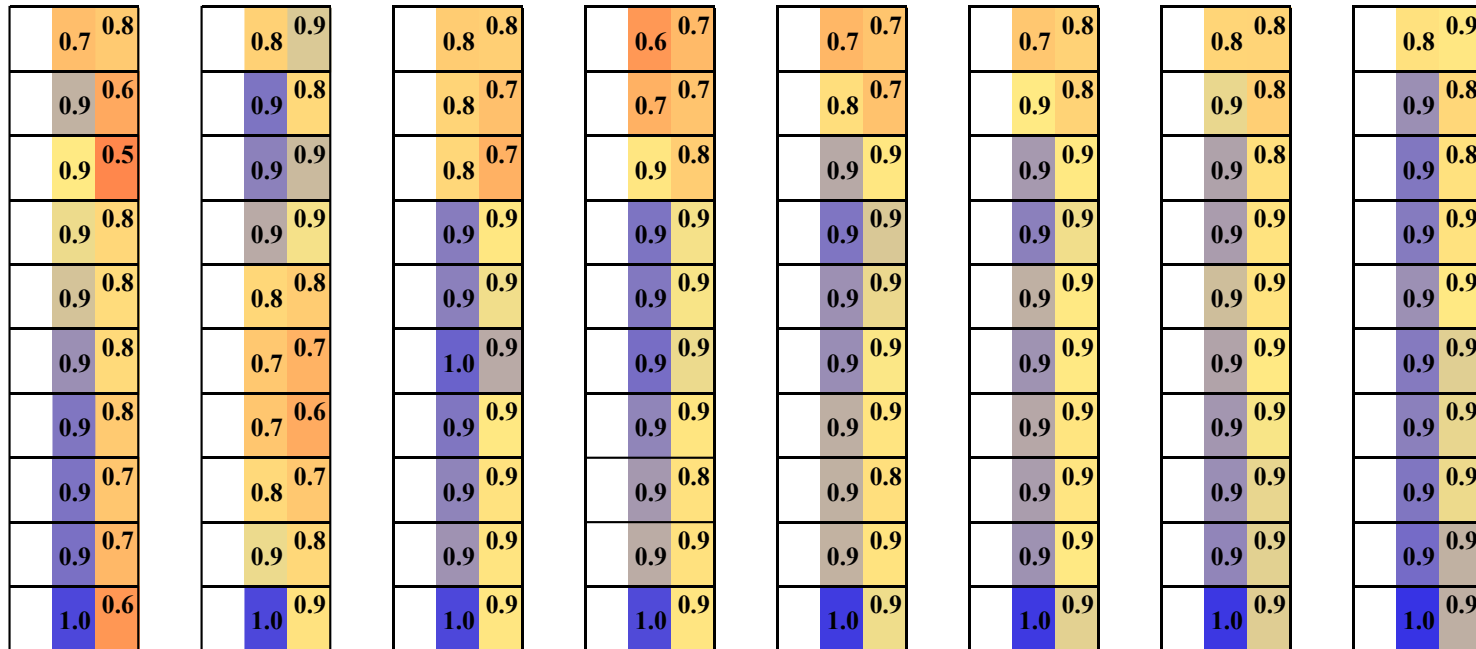*Appendix C-3: Cross-correlation of the lower surface pressure coefficients at 30° wind direction*

Appendix C-4: Cross-correlation of the lower surface pressure coefficients at 150° wind direction